

# DarkSide-20k Intermediate Design Report

## The Global Argon Dark Matter Collaboration

September 19, 2019



## DarkSide-20k Intermediate Design Report

C. E. Aalseth,<sup>1</sup> S. Abdelhakim,<sup>2</sup> F. Acerbi,<sup>3,4</sup> P. Agnes,<sup>5</sup> I. F. M. Albuquerque,<sup>6</sup> T. Alexander,<sup>1</sup> A. Alici,<sup>7,8</sup> A. K. Alton,<sup>9</sup> P. Amaudruz,<sup>10</sup> F. Ameli,<sup>11</sup> P. Antonioli,<sup>8</sup> S. Arcelli,<sup>7,8</sup> R. Ardito,<sup>12,13</sup> I. J. Arnquist,<sup>1</sup> P. Arpaia,<sup>14,15</sup> D. M. Asner,<sup>16</sup> A. Asunskis,<sup>17</sup> M. Ave,<sup>6</sup> H. O. Back,<sup>1</sup> A. Barrado Olmedo,<sup>18</sup> G. Batignani,<sup>19,20</sup> M. G. Bisogni,<sup>19,20</sup> V. Bocci,<sup>11</sup> A. Bondar,<sup>21,22</sup> G. Bonfini,<sup>23</sup> W. Bonivento,<sup>24</sup> B. Bottino,<sup>25,26</sup> M. G. Boulay,<sup>27</sup> R. Bunker,<sup>1</sup> S. Bussino,<sup>28,29</sup> A. Buzulutskov,<sup>21,22</sup> M. Cadeddu,<sup>30,24</sup> M. Cadoni,<sup>30,24</sup> A. Caminata,<sup>26</sup> N. Canci,<sup>5,23</sup> A. Candela,<sup>23</sup> C. Cantini,<sup>31</sup> M. Caravati,<sup>24</sup> M. Cariello,<sup>26</sup> M. Carpinelli,<sup>32,33</sup> A. Castellani,<sup>12,13</sup> P. Castello,<sup>34,24</sup> S. Catalanotti,<sup>35,15</sup> V. Cataudella,<sup>35,15</sup> P. Cavalcante,<sup>36,23</sup> S. Cavuoti,<sup>35,15</sup> S. Cebrian,<sup>37</sup> B. Celano,<sup>15</sup> R. Cereseto,<sup>26</sup> W. Cheng,<sup>38,39</sup> A. Chepurnov,<sup>40</sup> C. Ciccalò,<sup>24</sup> L. Cifarelli,<sup>7,8</sup> M. Citterio,<sup>13</sup> A. G. Cocco,<sup>15</sup> M. Colocci,<sup>7,8</sup> L. Consiglio,<sup>41</sup> F. Cossio,<sup>38,39</sup> G. Covone,<sup>35,15</sup> P. Crivelli,<sup>31</sup> I. D'Antone,<sup>8</sup> M. D'Incecco,<sup>23</sup> D. D'Urso,<sup>32,33</sup> M. D. Da Rocha Rolo,<sup>38</sup> M. Daniel,<sup>18</sup> S. Davini,<sup>26</sup> A. De Candia,<sup>35,15</sup> S. De Cecco,<sup>11,42</sup> M. De Deo,<sup>23</sup> A. De Falco,<sup>24,30</sup> G. De Filippis,<sup>35,15</sup> D. De Gruttola,<sup>43</sup> G. De Guido,<sup>44,13</sup> G. De Rosa,<sup>35,15</sup> G. Dellacasa,<sup>38</sup> P. Demontis,<sup>32,33,45</sup> S. DePaquale,<sup>43</sup> A. V. Derbin,<sup>46</sup> A. Devoto,<sup>30,24</sup> F. Di Eusanio,<sup>47,23</sup> G. Di Pietro,<sup>23,13</sup> P. Di Stefano,<sup>48</sup> C. Dionisi,<sup>11,42</sup> F. Dordei,<sup>24</sup> M. Downing,<sup>49</sup> F. Edalatfar,<sup>10</sup> A. Empl,<sup>5</sup> M. Fernandez Diaz,<sup>18</sup> A. Ferri,<sup>3,4</sup> C. Filip,<sup>50</sup> G. Fiorillo,<sup>35,15</sup> K. Fomenko,<sup>51</sup> A. Franceschi,<sup>52</sup> D. Franco,<sup>53</sup> G. E. Froudakis,<sup>54</sup> F. Gabriele,<sup>23</sup> A. Gabrieli,<sup>32,33</sup> C. Galbiati,<sup>47,41</sup> P. Garcia Abia,<sup>18</sup> D. Gascón Fora,<sup>55</sup> A. Gendotti,<sup>31</sup> C. Ghiano,<sup>23</sup> A. Ghisi,<sup>12,13</sup> S. Giagu,<sup>11,42</sup> P. Giampa,<sup>10</sup> R. A. Giampaolo,<sup>38</sup> C. Giganti,<sup>56</sup> M. A. Giorgi,<sup>20,19</sup> G. K. Giovanetti,<sup>47</sup> M. L. Gligan,<sup>50</sup> A. Gola,<sup>3,4</sup> O. Gorchakov,<sup>51</sup> M. Grab,<sup>57</sup> R. Graciani Diaz,<sup>55</sup> F. Granato,<sup>58</sup> M. Grassi,<sup>19</sup> J. W. Grate,<sup>1</sup> G. Y. Grigoriev,<sup>59</sup> A. Grobov,<sup>59</sup> M. Gromov,<sup>40</sup> M. Guan,<sup>60</sup> M. B. B. Guerra,<sup>17</sup> M. Guerzoni,<sup>8</sup> M. Gulino,<sup>61,33</sup> R. K. Haaland,<sup>62</sup> B. R. Hackett,<sup>63</sup> A. Hallin,<sup>64</sup> B. Harrop,<sup>47</sup> E. W. Hoppe,<sup>1</sup> S. Horikawa,<sup>41,23</sup> B. Hosseini,<sup>24</sup> F. Hubaut,<sup>65</sup> P. Humble,<sup>1</sup> E. V. Hungerford,<sup>5</sup> An. Ianni,<sup>47,23</sup> V. Ippolito,<sup>11</sup> C. Jillings,<sup>66,67</sup> S. Jimenez Cabre,<sup>18</sup> K. Keeter,<sup>17</sup> C. L. Kendziora,<sup>68</sup> S. Kim,<sup>58</sup> I. Kochanek,<sup>23</sup> K. Kondo,<sup>41</sup> G. Kopp,<sup>47</sup> D. Korablev,<sup>51</sup> G. Korga,<sup>5,23</sup> A. Kubankin,<sup>69</sup> R. Kugathasan,<sup>38,39</sup> M. Kuss,<sup>19</sup> M. Kuzniak,<sup>27</sup> M. La Commara,<sup>70,15</sup> M. Lai,<sup>30,24</sup> S. Langrock,<sup>66,67</sup> M. Lebois,<sup>2</sup> B. Lehnert,<sup>64</sup> X. Li,<sup>47</sup> Q. Liqiang,<sup>2</sup> M. Lissia,<sup>24</sup> G. U. Lodi,<sup>44,13</sup> G. Longo,<sup>35,15</sup> R. Lussana,<sup>71,13</sup> L. Luzzi,<sup>72,13</sup> A. A. Machado,<sup>73</sup> I. N. Machulin,<sup>59,74</sup> A. Mandarano,<sup>41,23</sup> L. Mapelli,<sup>47</sup> M. Marcante,<sup>75,4,3</sup> A. Margotti,<sup>8</sup> S. M. Mari,<sup>28,29</sup> M. Mariani,<sup>72,13</sup> J. Maricic,<sup>63</sup> M. Marinelli,<sup>25,26</sup> D. Marras,<sup>24</sup> A. D. Martinez Rojas,<sup>38,39</sup> C. J. Martoff,<sup>58</sup> M. Mascia,<sup>76,24</sup> A. Masoni,<sup>24</sup> A. Mazzi,<sup>3,4</sup> A. B. McDonald,<sup>48</sup> A. Messina,<sup>11,42</sup> P. D. Meyers,<sup>47</sup> T. Miletic,<sup>63</sup> R. Milincic,<sup>63</sup> A. Moggi,<sup>19</sup> S. Moioli,<sup>44,13</sup> J. Monroe,<sup>77</sup> M. Morrocchi,<sup>19</sup> T. Mroz,<sup>57</sup> W. Mu,<sup>31</sup> V. N. Muratova,<sup>46</sup> S. Murphy,<sup>31</sup> C. Muscas,<sup>34,24</sup> P. Musico,<sup>26</sup> R. Nania,<sup>8</sup> T. Napolitano,<sup>52</sup> A. Navrer Agasson,<sup>56</sup> M. Nessi,<sup>78</sup> I. Nikulin,<sup>69</sup> A. O. Nozdrina,<sup>59,74</sup> N. N. Nurakhov,<sup>59</sup> A. Oleinik,<sup>69</sup> V. Oleynikov,<sup>21,22</sup> M. Orsini,<sup>23</sup> F. Ortica,<sup>79,80</sup> L. Pagani,<sup>81</sup> M. Pallavicini,<sup>25,26</sup> S. Palmas,<sup>76,24</sup> L. Pandola,<sup>33</sup> E. Pantic,<sup>81</sup> E. Paoloni,<sup>19,20</sup> G. Paternoster,<sup>3,4</sup> V. Pavletcov,<sup>40</sup> F. Pazzona,<sup>32,33</sup> S. Peeters,<sup>82</sup> P. A. Pegoraro,<sup>34,24</sup> K. Pelczar,<sup>23</sup> L. A. Pellegrini,<sup>44,13</sup> N. Pelliccia,<sup>79,80</sup> F. Perotti,<sup>12,13</sup> V. Pesudo,<sup>18</sup> E. Picciau,<sup>30,24</sup> C. Piemonte,<sup>3,4</sup> F. Pietropaolo,<sup>78</sup> A. Pocar,<sup>49</sup> T. Pollman,<sup>83</sup> D. Portaluppi,<sup>71,13</sup> S. S. Poudel,<sup>5</sup> P. Pralavorio,<sup>65</sup> D. Price,<sup>84</sup> D. A. Pugachev,<sup>59</sup> B. Radics,<sup>31</sup> F. Raffaelli,<sup>19</sup> F. Ragusa,<sup>85,13</sup> M. Razeti,<sup>24</sup> A. Razeto,<sup>23</sup> V. Regazzoni,<sup>75,4,3</sup> C. Regenfus,<sup>31</sup> A. L. Renshaw,<sup>5</sup> S. Rescia,<sup>16</sup> M. Rescigno,<sup>11</sup> F. Retiere,<sup>10</sup> Q. Riffard,<sup>53</sup> A. Rivetti,<sup>38</sup> A. Romani,<sup>79,80</sup> L. Romero,<sup>18</sup> N. Rossi,<sup>11,23</sup> A. Rubbia,<sup>31</sup> D. Sablone,<sup>58,23</sup> P. Sala,<sup>78</sup> P. Salatino,<sup>86,15</sup> O. Samoylov,<sup>51</sup> E. Sánchez García,<sup>18</sup> S. Sanfilippo,<sup>29,28</sup> M. Sant,<sup>32,33</sup> D. Santone,<sup>77</sup> R. Santorelli,<sup>18</sup> C. Savarese,<sup>47</sup> E. Scapparone,<sup>8</sup> B. Schlitzer,<sup>81</sup> G. Scioli,<sup>7,8</sup> E. Segreto,<sup>73</sup> A. Seifert,<sup>1</sup> D. A. Semenov,<sup>46</sup> A. Shchagin,<sup>69</sup> E. Shemyakina,<sup>21,22</sup> A. Sheshukov,<sup>51</sup> S. Siddhanta,<sup>24</sup> M. Simeone,<sup>86,15</sup> P. N. Singh,<sup>5</sup> P. Skensved,<sup>48</sup> M. D. Skorokhvatov,<sup>59,74</sup>

- O. Smirnov,<sup>51</sup> G. Sobrero,<sup>26</sup> A. Sokolov,<sup>21,22</sup> A. Sotnikov,<sup>51</sup> R. Stainforth,<sup>27</sup> S. Stracka,<sup>19</sup>  
 G. B. Suffritti,<sup>32,33,45</sup> S. Sulis,<sup>34,24</sup> Y. Suvorov,<sup>35,15,59</sup> A.M. Szlc,<sup>84</sup> R. Tartaglia,<sup>23</sup>  
 G. Testera,<sup>26</sup> T. Thorpe,<sup>41,23</sup> A. Tonazzo,<sup>53</sup> A. Tosi,<sup>71,13</sup> E. V. Unzhakov,<sup>46</sup> G. Usai,<sup>24,30</sup>  
 A. Vacca,<sup>76,24</sup> E. Vázquez-Jáuregui,<sup>87</sup> M. Verducci,<sup>11,42</sup> T. Viant,<sup>31</sup> S. Viel,<sup>27</sup>  
 F. Villa,<sup>71,13</sup> A. Vishneva,<sup>51</sup> R. B. Vogelaar,<sup>36</sup> M. Wada,<sup>24</sup> J. Wahl,<sup>1</sup> J. J. Walding,<sup>77</sup>  
 H. Wang,<sup>88</sup> Y. Wang,<sup>88</sup> S. Westerdale,<sup>27</sup> R. J. Wheadon,<sup>38</sup> R. Williams,<sup>1</sup> J. Wilson,<sup>2</sup>  
 Marcin Wojcik,<sup>57</sup> Mariusz Wojcik,<sup>89</sup> S. Wu,<sup>31</sup> X. Xiao,<sup>88</sup> C. Yang,<sup>60</sup> Z. Ye,<sup>5</sup> and G. Zuzel<sup>57</sup>
- <sup>1</sup>Pacific Northwest National Laboratory, Richland, WA 99352, USA  
<sup>2</sup>Institut de Physique Nucléaire d'Orsay, 91406, Orsay, France  
<sup>3</sup>Fondazione Bruno Kessler, Povo 38123, Italy  
<sup>4</sup>Trento Institute for Fundamental Physics and Applications, Povo 38123, Italy  
<sup>5</sup>Department of Physics, University of Houston, Houston, TX 77204, USA  
<sup>6</sup>Instituto de Física, Universidade de São Paulo, São Paulo 05508-090, Brazil  
<sup>7</sup>Physics Department, Università degli Studi di Bologna, Bologna 40126, Italy  
<sup>8</sup>INFN Bologna, Bologna 40126, Italy  
<sup>9</sup>Physics Department, Augustana University, Sioux Falls, SD 57197, USA  
<sup>10</sup>TRIUMF, 4004 Wesbrook Mall, Vancouver, BC V6T 2A3, Canada  
<sup>11</sup>INFN Sezione di Roma, Roma 00185, Italy  
<sup>12</sup>Civil and Environmental Engineering Department, Politecnico di Milano, Milano 20133, Italy  
<sup>13</sup>INFN Milano, Milano 20133, Italy  
<sup>14</sup>Department of Electrical Engineering and Information Technology, Università degli Studi "Federico II" di Napoli, Napoli 80125, Italy  
<sup>15</sup>INFN Napoli, Napoli 80126, Italy  
<sup>16</sup>Brookhaven National Laboratory, Upton, NY 11973, USA  
<sup>17</sup>School of Natural Sciences, Black Hills State University, Spearfish, SD 57799, USA  
<sup>18</sup>CIEMAT, Centro de Investigaciones Energéticas, Medioambientales y Tecnológicas, Madrid 28040, Spain  
<sup>19</sup>INFN Pisa, Pisa 56127, Italy  
<sup>20</sup>Physics Department, Università degli Studi di Pisa, Pisa 56127, Italy  
<sup>21</sup>Budker Institute of Nuclear Physics, Novosibirsk 630090, Russia  
<sup>22</sup>Novosibirsk State University, Novosibirsk 630090, Russia  
<sup>23</sup>INFN Laboratori Nazionali del Gran Sasso, Assergi (AQ) 67100, Italy  
<sup>24</sup>INFN Cagliari, Cagliari 09042, Italy  
<sup>25</sup>Physics Department, Università degli Studi di Genova, Genova 16146, Italy  
<sup>26</sup>INFN Genova, Genova 16146, Italy  
<sup>27</sup>Department of Physics, Carleton University, Ottawa, ON K1S 5B6, Canada  
<sup>28</sup>INFN Roma Tre, Roma 00146, Italy  
<sup>29</sup>Mathematics and Physics Department, Università degli Studi Roma Tre, Roma 00146, Italy  
<sup>30</sup>Physics Department, Università degli Studi di Cagliari, Cagliari 09042, Italy  
<sup>31</sup>Institute for Particle Physics, ETH Zürich, Zürich 8093, Switzerland  
<sup>32</sup>Chemistry and Pharmacy Department, Università degli Studi di Sassari, Sassari 07100, Italy  
<sup>33</sup>INFN Laboratori Nazionali del Sud, Catania 95123, Italy  
<sup>34</sup>Department of Electrical and Electronic Engineering  
 Engineering, Università degli Studi, Cagliari 09042, Italy  
<sup>35</sup>Physics Department, Università degli Studi "Federico II" di Napoli, Napoli 80126, Italy  
<sup>36</sup>Virginia Tech, Blacksburg, VA 24061, USA  
<sup>37</sup>Laboratorio de Física Nuclear y Astropartículas, Universidad de Zaragoza, Zaragoza 50009, Spain  
<sup>38</sup>INFN Torino, Torino 10125, Italy  
<sup>39</sup>Department of Electronics and Communications, Politecnico di Torino, Torino 10129, Italy  
<sup>40</sup>Skobeltsyn Institute of Nuclear Physics, Lomonosov Moscow State University, Moscow 119234, Russia  
<sup>41</sup>Gran Sasso Science Institute, L'Aquila 67100, Italy  
<sup>42</sup>Physics Department, Sapienza Università di Roma, Roma 00185, Italy  
<sup>43</sup>INFN Salerno, Salerno 84084, Italy  
<sup>44</sup>Chemistry, Materials and Chemical Engineering Department  
 "G. Natta", Politecnico di Milano, Milano 20133, Italy  
<sup>45</sup>Interuniversity Consortium for Science and Technology of Materials, Firenze 50121, Italy  
<sup>46</sup>Saint Petersburg Nuclear Physics Institute, Gatchina 188350, Russia  
<sup>47</sup>Physics Department, Princeton University, Princeton, NJ 08544, USA

- <sup>48</sup>*Department of Physics, Engineering Physics and Astronomy,  
Queen's University, Kingston, ON K7L 3N6, Canada*
- <sup>49</sup>*Amherst Center for Fundamental Interactions and Physics  
Department, University of Massachusetts, Amherst, MA 01003, USA*
- <sup>50</sup>*National Institute for R&D of Isotopic and Molecular Technologies, Cluj-Napoca, 400293, Romania*
- <sup>51</sup>*Joint Institute for Nuclear Research, Dubna 141980, Russia*
- <sup>52</sup>*INFN Laboratori Nazionali di Frascati, Frascati 00044, Italy*
- <sup>53</sup>*APC, Université Paris Diderot, CNRS/IN2P3, CEA/Irfu, Obs de Paris, USPC, Paris 75205, France*
- <sup>54</sup>*Department of Chemistry, University of Crete, P.O. Box 2208, 71003 Heraklion, Crete, Greece*
- <sup>55</sup>*Universitat de Barcelona, Barcelona E-08028, Catalonia, Spain*
- <sup>56</sup>*LPNHE, CNRS/IN2P3, Sorbonne Université, Université Paris Diderot, Paris 75252, France*
- <sup>57</sup>*M. Smoluchowski Institute of Physics, Jagiellonian University, 30-348 Krakow, Poland*
- <sup>58</sup>*Physics Department, Temple University, Philadelphia, PA 19122, USA*
- <sup>59</sup>*National Research Centre Kurchatov Institute, Moscow 123182, Russia*
- <sup>60</sup>*Institute of High Energy Physics, Beijing 100049, China*
- <sup>61</sup>*Engineering and Architecture Faculty, Università di Enna Kore, Enna 94100, Italy*
- <sup>62</sup>*Department of Physics and Engineering, Fort Lewis College, Durango, CO 81301, USA*
- <sup>63</sup>*Department of Physics and Astronomy, University of Hawai'i, Honolulu, HI 96822, USA*
- <sup>64</sup>*Department of Physics, University of Alberta, Edmonton, AB T6G 2R3, Canada*
- <sup>65</sup>*Centre de Physique des Particules de Marseille, Aix  
Marseille Univ, CNRS/IN2P3, CPPM, Marseille, France*
- <sup>66</sup>*Department of Physics and Astronomy, Laurentian University, Sudbury, ON P3E 2C6, Canada*
- <sup>67</sup>*SNOLAB, Lively, ON P3Y 1N2, Canada*
- <sup>68</sup>*Fermi National Accelerator Laboratory, Batavia, IL 60510, USA*
- <sup>69</sup>*Radiation Physics Laboratory, Belgorod National Research University, Belgorod 308007, Russia*
- <sup>70</sup>*Pharmacy Department, Università degli Studi "Federico II" di Napoli, Napoli 80131, Italy*
- <sup>71</sup>*Electronics, Information, and Bioengineering Department, Politecnico di Milano, Milano 20133, Italy*
- <sup>72</sup>*Energy Department, Politecnico di Milano, Milano 20133, Italy*
- <sup>73</sup>*Physics Institute, Universidade Estadual de Campinas, Campinas 13083, Brazil*
- <sup>74</sup>*National Research Nuclear University MEPhI, Moscow 115409, Russia*
- <sup>75</sup>*Physics Department, Università degli Studi di Trento, Povo 38123, Italy*
- <sup>76</sup>*Department of Mechanical, Chemical, and Materials  
Engineering, Università degli Studi, Cagliari 09042, Italy*
- <sup>77</sup>*Department of Physics, Royal Holloway University of London, Egham TW20 0EX, UK*
- <sup>78</sup>*CERN, European Organization for Nuclear Research 1211 Geneve 23, Switzerland, CERN*
- <sup>79</sup>*Chemistry, Biology and Biotechnology Department, Università degli Studi di Perugia, Perugia 06123, Italy*
- <sup>80</sup>*INFN Perugia, Perugia 06123, Italy*
- <sup>81</sup>*Department of Physics, University of California, Davis, CA 95616, USA*
- <sup>82</sup>*Physics and Astronomy, University of Sussex, Brighton BN1 9QH, UK*
- <sup>83</sup>*Physik Department, Technische Universität München, Munich 80333, Germany*
- <sup>84</sup>*The University of Manchester, Manchester M13 9PL, United Kingdom*
- <sup>85</sup>*Physics Department, Università degli Studi di Milano, Milano 20133, Italy*
- <sup>86</sup>*Chemical, Materials, and Industrial Production Engineering Department,  
Università degli Studi "Federico II" di Napoli, Napoli 80126, Italy*
- <sup>87</sup>*Instituto de Física, Universidad Nacional Autónoma de México (UNAM), México 01000, Mexico*
- <sup>88</sup>*Physics and Astronomy Department, University of California, Los Angeles, CA 90095, USA*
- <sup>89</sup>*Institute of Applied Radiation Chemistry, Lodz University of Technology, 93-590 Lodz, Poland*

## CONTENTS

List of Figures	vi
List of Tables	vii
1. Project Overview	1
2. Photoelectronics	4
2.1. PhotoDetector Modules (PDM)	5
2.2. Signal Transmission	6
2.3. PDM Fabrication and Characterization	6
2.4. Motherboard Assembly	8
2.5. Mass Production	9
3. Inner Detector and Cryogenics System	9
3.1. DS-20k LAr TPC	9
3.2. Cryogenics	15
4. Material Assays	21
4.1. Radio-purity database	22
4.2. Managing Assay Capabilities	23
4.3. Radioactive budget	23
5. Calibration	24
5.1. Distributed Gas Sources	24
5.2. Gamma Sources	25
5.3. Neutron Sources	25
5.4. Guide Tube System	27
6. Veto Detector	28
6.1. Overall Design	28
6.2. Assembly	29
6.3. Background Rejection	30
7. Data Acquisition	32
7.1. General DAQ scheme	32
7.2. Digitizers	33
7.3. DAQ software	33
8. Computing	34
8.1. Computing systems and data workflow	34
8.2. Software Environment	35
8.3. Simulation	36
9. The ReD Experiment	36
10. DarkSide-Proto	40
10.1. Prototype Overview and Status	40
10.2. The DS-Proto TPC	41
10.3. Materials for DarkSide-Proto	43
10.4. Validation tests and operation	43
11. AAr Cryostat	43

12. Argon Procurement and Purification	47
12.1. Urania	47
12.2. Aria	52
12.3. DArT	54
References	56

## LIST OF FIGURES

1	Artist rendering of the DS-20k experiment in Hall C of LNGS .....	1
2	Artist rendering of the DS-20k detectors .....	2
3	The first PDM and first motherboard resulting from the assembly of PDMs .....	5
4	Schematic of the transimpedance amplified and summing circuits .....	6
5	Variance of impedance of SiPMs quenching resistors .....	7
6	SiPM <i>I-V</i> curves and SNR .....	8
7	SNR of the SiPMs tiles of the first motherboard .....	9
8	Artist rendering of the PMMA vessel and the TPC .....	11
9	PDM patterning scheme .....	12
10	DS-20k PDM motherboard designs .....	13
11	3D model of the full DS-20k LAr TPC reflector panels system .....	14
12	DS-20k LAr TPC anode and cathode regions .....	15
13	Simulated electric field mapping of the DS-20k LAr TPC .....	17
14	DS-20k cryogenics system P&ID .....	18
15	DS-20k condenser box .....	19
16	DS-20k materials database structure .....	22
17	Web interface of DS-20k materials database .....	23
18	Schematic of the sources insertion system .....	26
19	Pictures of the miniature $^{241}\text{AmBe}$ neutron source .....	27
20	Schematic and 3D cut-away view of the DS-20k veto detector .....	28
21	3D drawings of the DS-20k Veto detector .....	30
22	Picture of the LNS beamline in use for ReD .....	38
23	Preliminary data from the ReD experiment .....	39
24	The DS-Proto cryostat and components delivered at CERN .....	41
25	Conceptual design of the DS-Proto detector .....	42
26	Schematics of the setup for the optimization of the S2 signals .....	44
27	Details of the AAr cryostat .....	45
28	3D view of the large AAr cryostat .....	45
29	Cross-sectional view of the large AAr cryostat .....	46
30	Process Flow Diagram for the Urania UAr extraction plant .....	49
31	Screening test plant for the Urania PSA sorbent .....	50
32	Schematic view of UAr cryogenic shipping vessel .....	51
33	Block diagram of Aria .....	53
34	The Seruci-0 cryogenic distillation column .....	55

## LIST OF TABLES

I	DS-20k LAr TPC detector parameters .....	10
II	DarkSide-20k cryogenics system parameters.....	16
III	Summary of DS-20k assays performed.....	24
IV	Summary of the assay capabilities available for DS-20k .....	24
V	Radiogenic neutrons from detector materials and background before and after cuts..	31
VI	Inlet argon purity required for operation of the DarkSide-20k getter .....	47

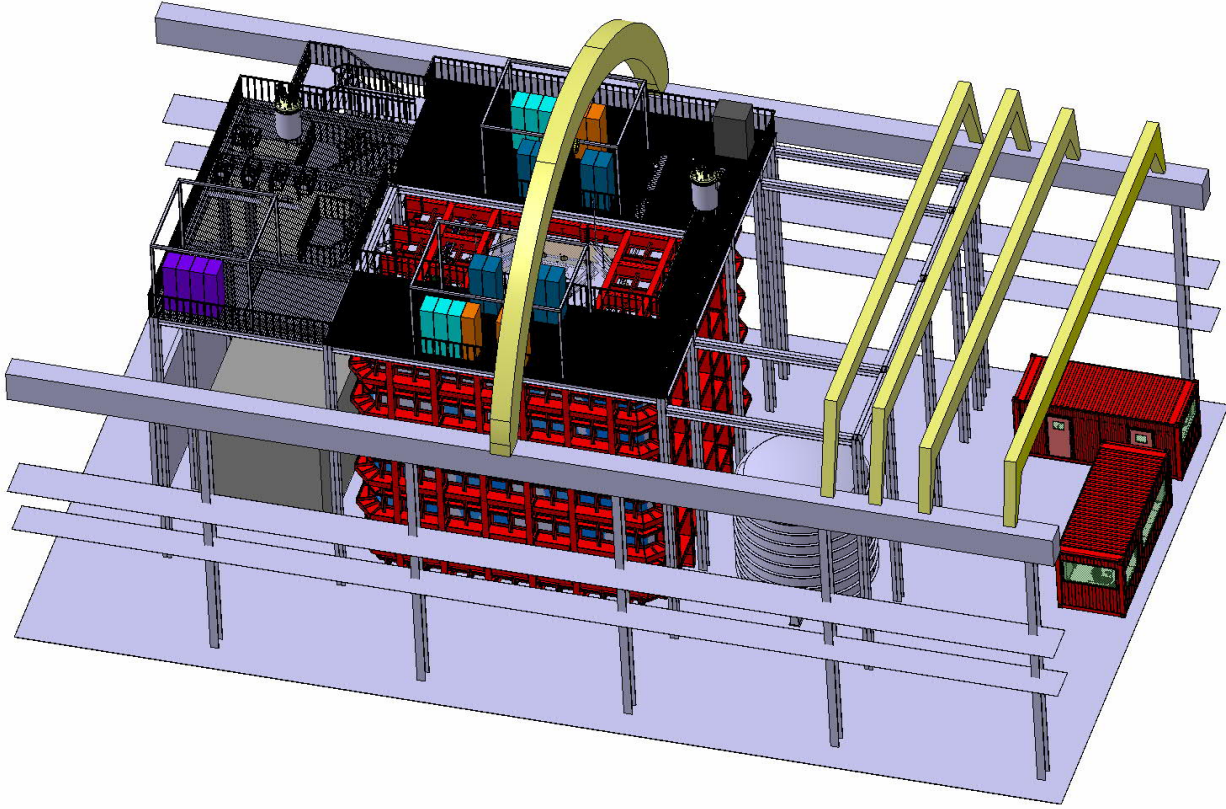


FIG. 1. Artist rendering of the DS-20k experiment in Hall C of LNGS.

## 1. PROJECT OVERVIEW

Many fundamental design parameters for the DarkSide-20k (DS-20k) experiment are based on the successful experience of the DarkSide Collaboration in constructing, commissioning, and operating the DarkSide-50 (DS-50) detector in a background-free mode. The many technical details of DarkSide-50 can be found in [1–14]. The DS-20k liquid argon time projection chamber (LAr TPC) will, too, be deployed at LNGS in the underground Hall C, at the center of a newly constructed active veto system. Fig. 1 shows the rendering of the future installation of DS-20k in the underground Hall C of LNGS and Fig. 2 shows an overview of the detailed arrangement of the LAr TPC and its anti-coincidence veto detector. The DS-20k experiment is designed to operate for a minimum of 10 yr while maintaining an irreducible background level in the WIMP search region of less than  $<0.1$  events for the total exposure. To achieve this goal, the design parameters of the DS-20k experiment have been taken directly from DS-50, where possible. Design changes have been made where needed in order to accommodate for the much larger size of DS-20k and to allow the experimental design to be scalable to a detector at the multi-hundred tonne scale. In building this preliminary design, issues that have arisen because of design choices or materials selections have been dealt with by limited design modifications, and further optimization will continue as the final development work is completed and a full technical design is made.

DS-20k will be built by the Global Argon Dark Matter Collaboration (GADMC) and will consist of two detectors: the inner detector and the veto detector, both hosted in a ProtoDUNE-like cryostat [15, 16]. The inner detector is a LAr TPC filled with underground argon (UAr). The veto detector is made of a plastic shell, loaded with Gd, surrounding the inner detector, sandwiched between two active atmospheric argon (AAr) layers.

The decision to abandon an organic liquid scintillator veto and to host DS-20k within a ProtoDUNE-like cryostat was originally motivated by the need of minimizing the environmen-

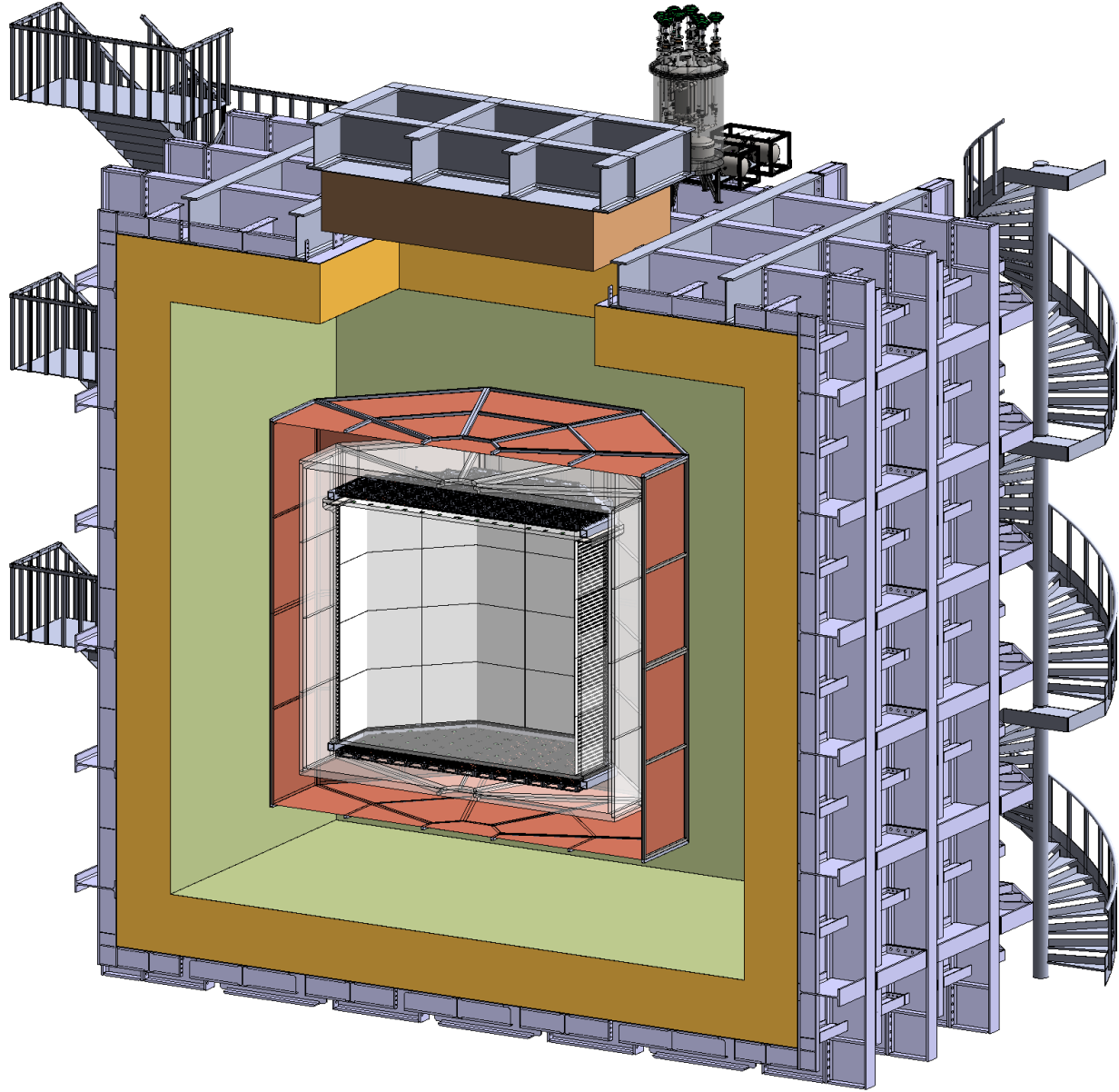


FIG. 2. Artist rendering of the DS-20k detectors, with many components omitted for clarity of presentation. The drawing shows the acrylic (PMMA) sealed TPC filled with UAr, surrounded by the veto detector consisting of a Gd-loaded acrylic Shell (GdAS) sandwiched between two atmospheric argon (AAr) active layers (the Inner Active Buffer, IAB and the Outer Active Buffer, OAB), all contained in the ProtoDUNE-like cryostat. The OAB is optically separated from the rest of the AAr by a copper vessel. Technical designs of the support structure of the TPC are already available, and intentionally omitted for clarity of presentation of the main elements.

tal impact on underground LNGS operations, but carries significant performance advantages. Indeed, operating the TPC directly in the ProtoDUNE-like cryostat eliminates the need of a cryostat in the immediate proximity of the UAr target, which would significantly contribute to the residual background. We therefore adopted a new design, with the UAr-filled TPC immersed in a bath of liquefied AAr held at the same temperature and pressure. This then allows for the use of a TPC vessel fabricated from the same ultra-pure poly(methyl methacrylate) (acrylic or PMMA) developed for the DEAP-3600 experiment, and thus eliminating the need for a dedicated cryostat or UAr containment vessel. The outer walls of the TPC will sit approximately 2 m away from inner

wall of the cryostat. The ProtoDUNE-like cryostat may be surrounded by layers of plastic for moderation of cosmogenic and radiogenic neutrons from the rocks surrounding the LNGS Hall C, this option is being investigated.

While this overview section gives a general outline of the project and introduces the major features of the experiment as they stand in the current preliminary design, the real details are given in the subsequent sections. The development of the SiPM photosensors, the LAr TPC and its cryogenics and gas handling system, and the materials screening plan that will ensure the radio purity of the experiment, are detailed in Sec. 2, Sec. 3 and Sec. 4, respectively. The plan for the calibration of the experiment is given in Sec. 5, the design of the veto detector is presented in Sec. 6, and the details about the data acquisition system and the plan for offline computing are given in Sec. 7 and Sec. 8, respectively. The two ancillary detectors, ReD and DarkSide-Proto, are described in Sec. 9 and Sec. 10. Finally, the design and use of the atmospheric argon cryostat, modeled after the ones deployed for ProtoDUNE, are given in Sec. 11, while the procurement of the underground argon (UAr) target is detailed in the final section, Sec. 12. Note that the following forms a preliminary design for an experiment capable of the stated physics goals, but may change as the technical details evolve in the final engineering stages. DS-20k will be built to operate for a minimum of 10 yr, providing the best sensitivity to high-mass WIMP dark matter.

Energy deposits in the LAr target result in the production of excited and ionized argon atoms, according to the underlying process for recoiling electrons or nuclei. Excited argon atoms, which can also be produced by recombining ionization charge, lead to an efficient formation of argon excimers decaying via the emission of scintillation light characterized by two decay time constants. Both of the components are combine to yield an instant light signal, called S1. Due to the deep UV nature (around 128 nm) of this scintillation light, which is absorbed by most materials, a thin layer of wavelength shifter, tetraphenyl butadiene (TPB), must cover all exposed surfaces to convert the photons to those of optical wavelengths for detection by photosensors. Ionization electrons escaping recombination are drifted to the top of the LAr by an applied electric field, where an electric field stronger than the field applied to drift the electrons, extracts the electrons into the gas pocket above the liquid. Here the strong field accelerates the electrons, enough for them to excite (but not ionize) the argon gas, producing a secondary scintillation signal S2, proportional to the ionization charge. Photosensors placed behind the wavelength shifter-coated windows at the top and bottom of the TPC, read out both scintillation signals (S1 and S2) of each event. S1 is used for energy determination, as well as for pulse shape discrimination (PSD). The latter is derived from the ratio of the prompt and delayed light fractions. S2 is used for energy and 3D position measurements of the event, the vertical coordinate is measured from the drift time between S1 and S2, and the horizontal coordinates from the light pattern resulting in the top photosensors from S2.

The octagonal LAr TPC will have a height of 350 cm and a distance between parallel walls of 355 cm. It will be instrumented with a new kind of photosensors, arrays of SiPMs, arranged in assemblies called photodetector modules (PDMs). Each PDM has an area comparable to that of a 3" photomultiplier tube (PMT), with the LAr TPC containing 8280 PDMs in total. Substantial effort was put into the development of this technology, since SiPMs promise a higher effective quantum efficiency, higher reliability at LAr temperature, and a much higher radiopurity than PMTs. All of these properties are crucial for DS-20k since the PSD, which is the most important mechanism for background discrimination in LAr, depends critically on the light yield. Additionally, the large material budget of PMTs is often a limiting factor for neutron- and gamma-induced backgrounds. The LAr TPC will be equipped with arrays of SiPMs, totaling  $21\text{ m}^2$  in area.

In comparison to DS-50, where a full digitization and recording of the waveform of each PMT could be achieved, a custom scheme for the sampling of the two-orders-of-magnitude higher channel count of the DS-20k SiPM PDMs has to be developed. Design parameters for the data acquisition (DAQ) system are driven by rates and occupancies, as well as leading edge timing and limited charge information from each channel, while compromising as little as possible on energy resolution and pulse-shape discrimination.

All components of the detector, especially the inner components, like the LAr TPC, the SiPM arrays, and cables, must be made from materials of the highest radiopurity to keep backgrounds as

small as possible.

The veto detector consists of three separate volumes:

- An inner volume of active liquid AAr, called the Inner Argon Buffer (IAB), surrounding the TPC;
- A passive shell of acrylic loaded with Gd, called the Gd-loaded Acrylic Shell (GdAS), of octagonal shape mounted around the IAB. The GdAS surrounds the TPC in all directions (lateral, top and bottom, with exceptions due to the signal and utility service holes).
- An outer active volume of AAr, called the Outer Argon Buffer (OAB).

A copper cage which acts as a Faraday cage provides the optical insulation from the rest of the AAr external to OAB and, at the same time, it realizes the necessary electric shield for reducing external noise from contaminating the detector signals. The details of the veto design and expected performance are given in Sec. 6.

In order to demonstrate and test technological developments on a scale relevant to DS-20k, the collaboration will build and operate a  $\sim 1$  t prototype. The project is called DarkSide-Proto (DS-Proto) and is described in Sec. 10. DarkSide-Proto will be at an intermediate scale between DS-50 and DS-20k, able to test a number of full size components intended for use in DS-20k. The size of DS-Proto was chosen to be able to validate detector and PDM components, including the readout system, both from the mechanical and performance aspects of the experiment. The full size cryogenic system will also be tested in this way, especially the argon condenser, the gas pump, and the heat recovery system. Functionality and stability control, as well as safety issues during power failures, purification flow rates and general controls are meant to be explored. DS-Proto also serves to validate the readiness of the various production lines in the different institutions of the collaboration to ensure quality control and assurance for the production of components for DS-20k.

For the DarkSide-20k detector to reach its physics goals, a comprehensive plan of calibrations for the LAr TPC and Veto detectors is necessary. The calibration equipment and techniques specific to the DS-20k experiment are described in detail in Sec. 5. In addition to this, it will be important to also utilize measurements taken with external calibration experiments placed within the line of sight of a neutron beam. In the SCENE experiment,[17, 18] a monochromatic, low energy, pulsed neutron beam at the Notre Dame Institute for Structure and Nuclear Astrophysics was used to study the scintillation light yield from recoiling nuclei in a small LAr TPC, but only down to 57.3 keV<sub>nr</sub>. The ARIS experiment was exposed to the highly collimated and quasimonoenergetic LICORNE neutron beam at the Institut de Physique Nucléaire d'Orsay (IPNO) in order to study the scintillation response to nuclear and electronic recoils [10].

The collaboration is now expanding this external calibration work with a new external calibration experiment, the Recoil Directionality (ReD) experiment, described in Sec. 9. The ReD detector is a small LAr TPC (similar in size to SCENE) equipped with the same SiPM tiles planned for use in DS-20k. ReD is designed to select and measure single neutron elastic scatters on argon nuclei, by means of a large acceptance neutron spectrometer, composed of an array of liquid scintillator detectors. Kinematic requirements of the neutron interactions will allow for the precise detection of nuclear recoils in the LAr, since the neutron energy, scattering angle, and drift field direction can all be precisely measured with the use of external neutron detectors.

## 2. PHOTOELECTRONICS

Silicon photomultipliers (SiPMs) are one of the key enabling technologies for large-scale LAr-based dark matter experiments. SiPMs will also play an important role in the next generation of LAr-based neutrino detectors, such as DUNE [16], and liquid xenon based detectors for neutrinoless double beta decay, such as nEXO [19]. SiPMs have a number of performance advantages over traditional PMTs, including higher photon detection efficiency (PDE) and much better single-photon resolution, all while operating at much lower bias voltage. SiPMs can also be efficiently integrated into tiles that cover large areas and feature better radio-purity than PMTs.

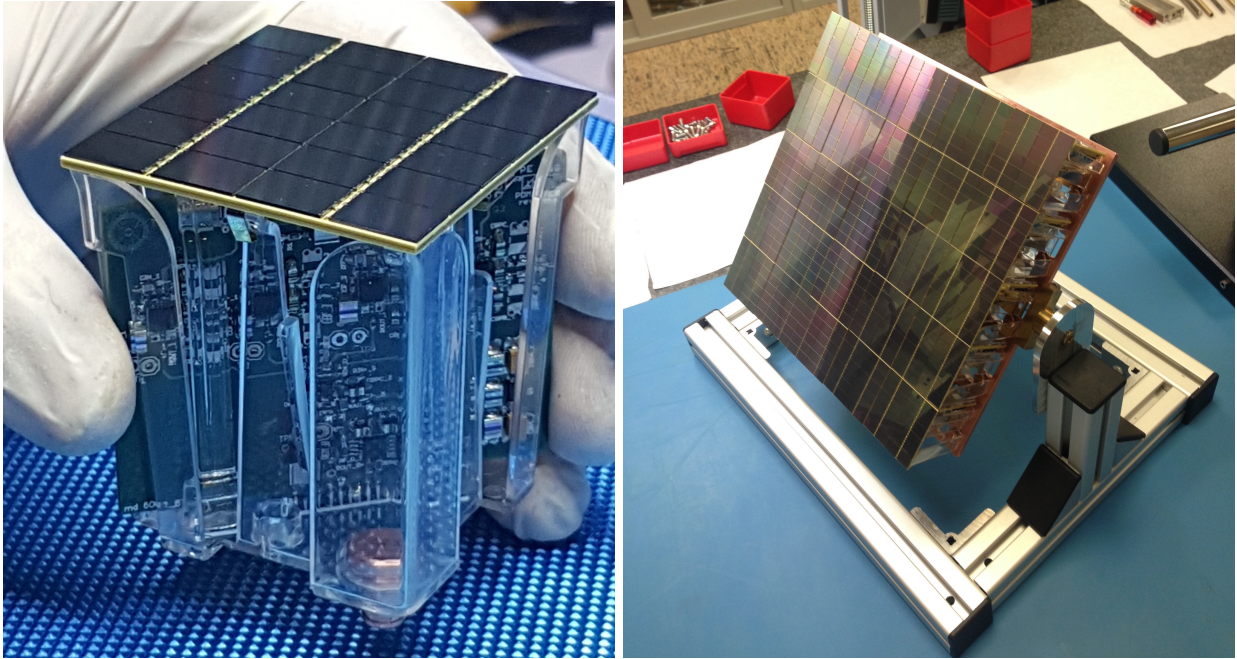


FIG. 3. **Left:** Single channel PhotoDetector Module (PDM) consisting of a  $50 \times 50 \text{ mm}^2$  tile of 24 SiPMs and a front-end board. **Right:** The DS-20k motherboard assembled with 25 PDMs.

### 2.1. PhotoDetector Modules (PDM)

For DS-20k, the photosensing unit will be a “PhotoDetector Module” (PDM), consisting of a large tile of SiPMs covering a total area of  $50 \times 50 \text{ mm}^2$  operating as a single detector (see the left panel of Figure 3). Besides the tile, each module will also contain a cryogenic preamplifier board that will amplify and shape the signal in the immediate proximity of the sensor. The output of the cryogenic amplifier will be passed on to a signal transmitter, also integrated into the PDM, and responsible for transmission of the signal through the cryostat penetration. Finally, the PDM will also include the mechanical structure required to assemble all components and to efficiently dissipate heat in the LAr target, minimizing the production of bubbles. An intelligent power distribution system is also foreseen, capable of disabling individual PDMs in case of failure.

The unique challenge in readout presented by SiPMs is mainly due to their capacitance. At  $50 \text{ pF/mm}^2$ , a single SiPM with a  $5 \times 5 \text{ mm}^2$  surface area passes the nF scale for capacitance. Yet, the experiment foresees a photo-sensing area of  $21 \text{ m}^2$ . The readout of a LAr calorimeter faced a similar challenge, with capacitance for the individual cells often passing the nF scale [20]. Early developments on LAr calorimeter readout [21–24] demonstrated that the use of a transimpedance amplifier (TIA) is preferable to a charge integration amplifier where the noise and rise time are very strongly affected by the large detector capacitance. With this in mind, the DarkSide Collaboration has developed and optimized a TIA (schematic is shown in the left panel of Figure 4) with performance at 87 K in mind [25]. The specific goal was to maximize the amplification factor while preserving a stable signal bandwidth and SNR.

The SiPMs readout scheme strongly affects the PDM performance in terms both of SNR and bandwidth of the signal. A hybrid readout scheme, with parallel-series combination of SiPMs, first introduced for the MEG experiment [26, 27], solves at once these two problems. In this configuration, the output signal of an individual SiPM is reduced by a factor equal to the number of SiPMs put in series, but this disadvantage is offset by the attenuation of the noise gain due to the reduction in the input capacitance. Most importantly, a strong improvement of the bandwidth with respect to the parallel readout scheme is achieved, with six SiPMs easily readout by connecting in parallel three branches of two SiPMs put in series (known as the 2s3p configuration [28], see right panel of Figure 4) with a bandwidth comparable to the one achievable with a single SiPM in

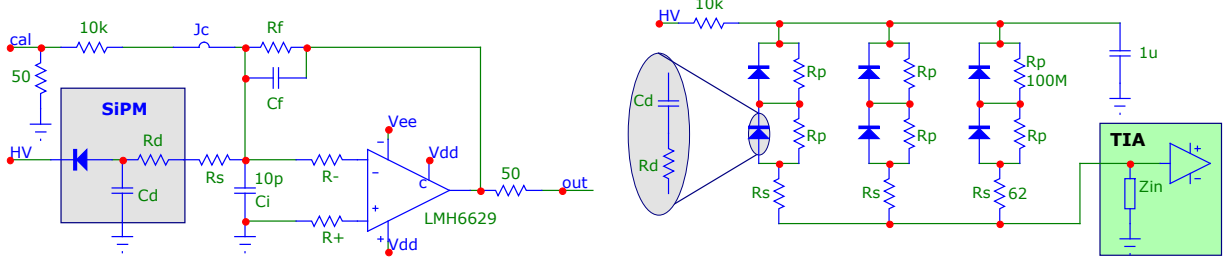


FIG. 4. **Left:** Schematic diagram of the transimpedance amplifier circuit developed to readout SiPMs. **Right:** Schematic diagram of the 2s3p readout scheme optimized for summing six SiPM signal together.

input. Four such readout quadrants are fit in a single PDM, with their output signals summed at the transmission stage.

## 2.2. Signal Transmission

The signal transmission from the PDMs to the warm electronics is of primary importance for the experiment. Given the high number of independent channels, cables would introduce a large mass in the cryostat with the inherent problems of radio-purity and heat load. The delivery of the PDM signals to the outside world through optical fibers will solve at once these two problems. For this purpose an optical analog cryogenic transmitter has been developed. The prototype boards of the opto-link system (optical driver and optical receiver board) have been recently produced. The optical receiver board (32 channels) was successfully tested, while the optical driver board (25 channels) is at the moment undergoing testing.

The PDMs will be located above the anode and below the cathode, fully covering the top and bottom faces of the LAr TPC active volume, to detect both the S1 and S2 signals with high efficiency. The top and the bottom photon readout assemblies will consist of 4140 PDMs each. Multiple PDMs are mounted to a single motherboard to form two larger basic mechanical units called the square board (SQB) and the triangular board (TRB), described in Sec. 3.3.1 and shown in Figure 10. The SQB and TRB have the same edge size of 25 cm. The SQB and TRB are then used to form the full readout planes (shown in Figure 9). The total number of readout channels (top and bottom) is 8280.

## 2.3. PDM Fabrication and Characterization

Following the successful construction of the first Photo-Detector Module (PDM) in March 2018, the Photo-Electronics Working Group proceeded to the construction of the first Motherboard, shown in Figure 3. The FBK company delivered two SiPM runs: the first one with standard doping SiPMs (cell size  $25 \times 25\ \mu\text{m}^2$  and quenching resistor  $10\ M\Omega(77\text{ K})$ ) and the second one with triple doping SiPMs (cell size  $30 \times 30\ \mu\text{m}^2$  and quenching resistor  $5\ M\Omega(77\text{ K})$ ). Since the latter SiPM type is considered the best candidate for the DS-20k experiment, we decided to use the single doping SiPMs for the first Motherboard construction, so that the triple doping type could be mounted later, taking advantage of the experience gained with the mounting of the first Motherboard.

This SiPM run was characterized by a reasonable yield at  $-40^\circ\text{C}$  of about 50 %. A detailed inspection of the SiPM quenching resistor ( $R_q$ ) showed good uniformity for most of the wafers, while the first and the second wafers (W1,W2) had a 20 % larger  $R_q$  (see Figure 5). The optimal working voltage of the SiPM is expected to change as a function of  $R_q$ , so in the forthcoming mass production by the LFoundry company, where hundreds of 8 " SiPM wafers are scheduled, this quenching resistor spread is not an issue since the SiPMs with similar  $R_q$  can be paired. In this way, each Motherboard, with PDMs biased at the same voltage, will be made of devices with

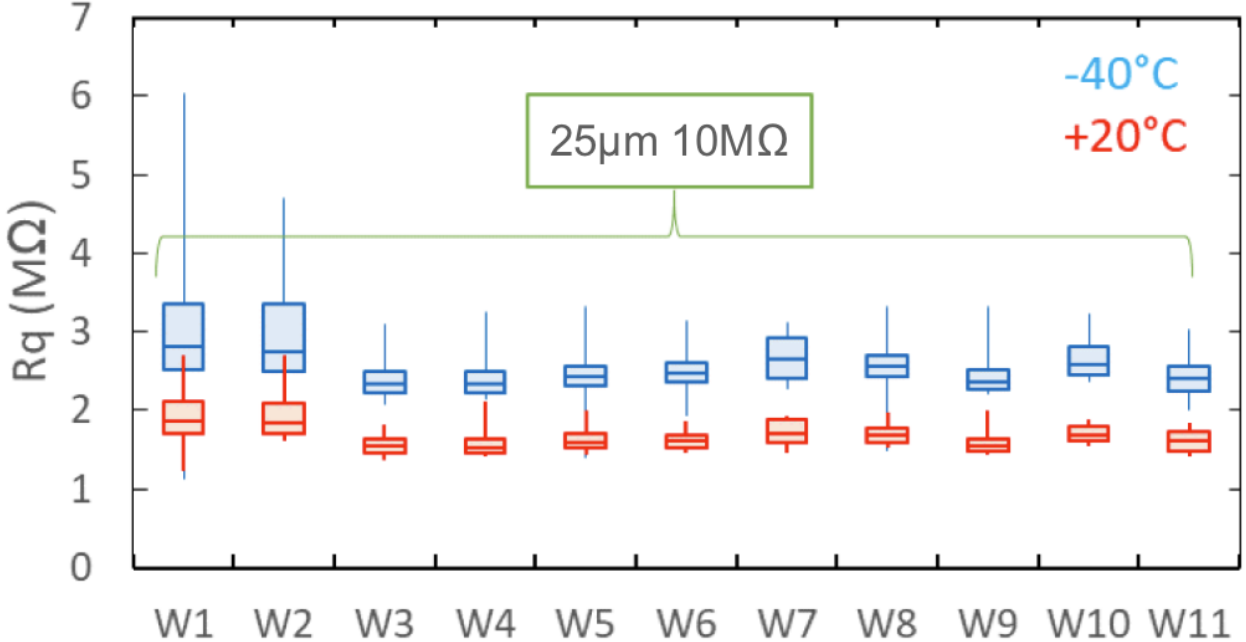


FIG. 5. Average SiPM quenching resistor value vs. wafer number measured at 20 °C and -40 °C.

similar  $R_q$ . Due to the limited SiPMs available in the present production we had to use all of them to make the first Motherboard, and thus all were biased with a common voltage despite the slight difference in  $R_q$ . As a consequence, the tiles made with SiPMs belonging to wafers 1 and 2 were fed with an overvoltage lower than the optimal one for some of the SiPMs, i.e. 5 V. It is worth noting that a dedicated facility for the Motherboard production is not available yet, and therefore the use of equipment through outsourcing and additional man power was therefore required.

The tile and the Front-End Board PCBs were made with an Arlon 55-NT substrate, following the experience gained during the first PDM construction. The electronic components were mounted with outsourced equipment, under the supervision of LNGS personnel. The tile PCBs were tested both at warm and at cryogenic temperatures to verify the correct circuit impedance. After the wafer dicing, the SiPMs were shipped from FBK to Princeton University, where the first Motherboard tiles were bonded by personnel from LNGS, Princeton University and TIFPA. A cryogenic epoxy for the SiPM back-side and a wire-bonding connection for the front-side was used. The 27 tiles, each made of 24 SiPMs, were then shipped to LNGS, using multipurpose acrylic boxes, designed by the Pisa group. This box allows for safe shipping of the tile, offering an adequate protection of the SiPM wire bonding and, at the same, time allows the tile characterization in liquid nitrogen by permitting the insertion of the Front End Board without removing the tile from the box. The tiles underwent a comprehensive test at LNGS both at warm temperature and in LN, including the reverse I-V curve measurement, the power spectrum and the charge spectra. We found just one tile out of the 27 with two SiPM branches (4 SiPMs) not working properly. Another tile showed a noise level higher than the average. These two tiles were therefore excluded from the list of the tiles selected to populate the first Motherboard.

As an example, the left side of Figure 6 shows the tile I-V curves taken at 77 K, indicating a homogeneous behavior.

The right panel of Figure 6 shows the signal to noise ratio (SNR) for the 27 tiles at their optimal voltage. It is worth noting that all of them have a SNR larger than the minimum SNR of 8, required by the DarkSide-20k experiment specifications. For each tile, the SNR was obtained relying on several different procedures and analysis methods. The bar length in the figure represents the spread of each measurement, depending on the method used. The signal-to-noise ratio (SNR) is defined as the ratio between the gain and the width of the baseline noise peak. The gain is measured by fitting the center values of the amplitude multiple peaks and evaluating the slope of a

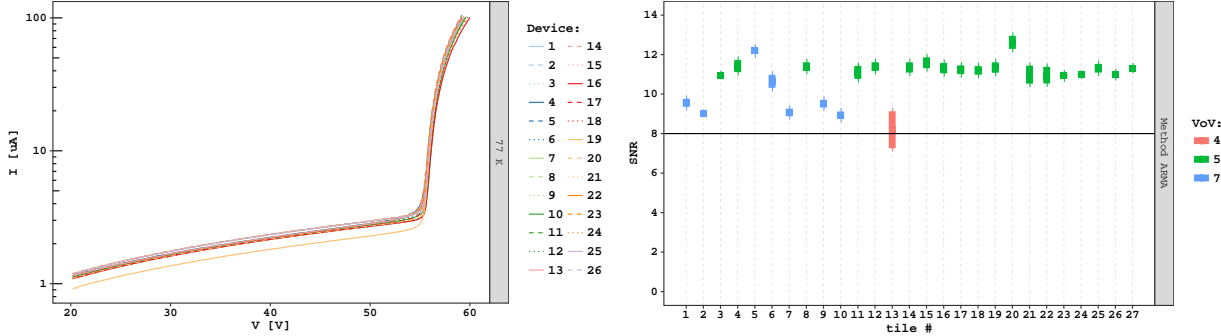


FIG. 6. **Left:** Reverse I-V curves for the SiPM tiles measured at 77 K. **Right:** SNR of the 27 bonded SiPM tiles.

linear fit. The baseline noise is extracted from the average standard deviation of the waveform in a pre-pulse window, 500 ns long, using 500 samples. For most tiles, the distribution of the standard deviation is not symmetric around the peak. The most important contribution to the noise baseline is the presence of one or more photoelectrons not stimulated by the laser pulse. These can originate from a SiPM having an excess of dark-rate or more probably by an excess of after-pulsing.

Since the distribution is not symmetric, the estimate of the baseline noise is intrinsically biased and two options are possible, corresponding to the mean value or the most probable value (mode). Consequently the SNR is defined in a confidence interval between  $\text{SNR}_{\min} = \text{gain}/\text{noise}_{\text{mean}}$  and  $\text{SNR}_{\max} = \text{gain}/\text{noise}_{\text{mode}}$ .

Figure 7 shows the SNR obtained with the common over-voltage of 5 V. Although a few tiles, as expected, manifest a SNR slightly below 8, the SNR is quite good for all tiles used in the assembly of the first Motherboard.

#### 2.4. Motherboard Assembly

Before assembling the first Motherboard, a full mock-up made of an aluminum Motherboard structure, an FR4 Motherboard strip PCB, 25 dummy tiles and FEBs, and the PDM acrylic mechanics was mounted at Bologna. Each PCB had the same dimensions of the final one, while the HV/LV and signal layers were not included in the stack-up. The mounting required just a few hours and the overall procedure was validated, while the mechanics of the different components nicely merged, suggesting just a few minor mechanical improvements.

After these tests, the tiles were finally shipped to Pisa, while the PDM pillars and the copper Motherboard structure were milled at Bologna using 99.997% pure copper sold by the Luvata Company. The first Motherboard was equipped with a PCB strip connecting the PDMs, made of a thin stack-up (0.5 mm) based on a Pyralux substrate and shipped to Pisa to start the mounting of the 25 PDMs on the Motherboard.

The PDMs were assembled in the Pisa clean room, following the prescriptions used for the first PDM, assembled in March 2018. The mounting of the 25 PDMs on the Motherboard was finalized in few days. A picture of the first Motherboard, fully equipped with the first 25 PDMs is shown in the right panel of Figure 3.

In summary the construction of the first Motherboard required the production, testing, selection and bonding of more than 600 SiPMs. Although a cryogenic probe and an automatic bonder were not available yet, the Collaboration was able to increase the number of successfully built PDMs from 1 to 25, in just 6 months. The bonding yield exceeded 95 % (just 1 tile out of the 27 showed problems with the SiPM bonding strategy), while the satisfactory PDM SNR demonstrated the validity of the full Motherboard construction process.

After the completion of the first motherboard, equipped with 25 PDMs each containing 24 single dose SiPM's, the collaboration moved to the construction of a second Motherboard, equipped with triple dose SiPMs. At the moment, half of the PDMs have already been assembled and mounted

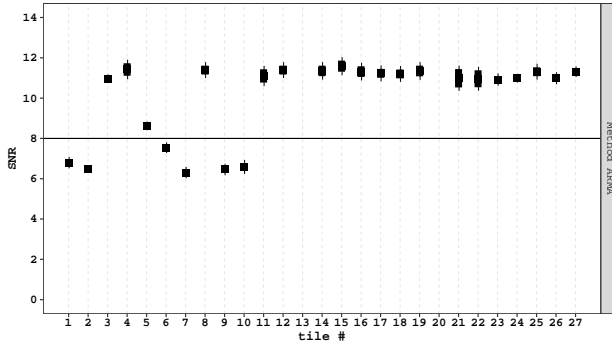


FIG. 7. SNR of the 25 SiPM tiles populating the first motherboard while. Data were recorded while operating the SiPM tiles at an over-voltage of 5 V.

in the copper structure. The remaining PDMs will be mounted within the summer of 2019. The FEBs were already successfully tested, while the SiPM tiles are currently undergoing testing in LN. The next step in the photo-electronics schedule is the production of about 400 PDMs for the DS-Proto detector. These SiPMs will be produced by the LFoundry Company in Avezzano, Italy. The first run is expected in the summer of 2019.

## 2.5. Mass Production

The first engineering run, finalized in September 2018 and tested shortly after, showed the capability of the silicon foundry to implement the FBK technology. The produced SiPMs showed good performance at both room temperature and in liquid nitrogen. A second LFoundry engineering run, presently ongoing, is devoted to the development of the through silicon vias (TSV). This post-production rework requires some delicate mechanical manipulation of the SiPM wafers.

The DS-20k SiPM packaging foresees the production of more than 10 000 PDMs in 2.5 yr. This remarkable effort requires a large clean room, relying on cutting edge technology equipment and trained personnel. The GADMC selected for the NOA DS-20k SiPM packaging facility a clean room at the *Tecnopolo dell’Aquila*, with surface exceeding 700 m<sup>2</sup>. The clean room will be soon refurbished to comfortably host the needed equipment and personnel. This facility will be managed by GSSI, through an agreement with INFN that will soon be finalized. Concerning the procurement of the equipment for the DS-20k PDMs mass production, the cryogenic probe tender was just approved by the INFN Executive Board and the flip-chip bonder tender will follow in the weeks to come.

## 3. INNER DETECTOR AND CRYOGENICS SYSTEM

### 3.1. DS-20k LAr TPC

The DarkSide-20k LAr TPC is the dark matter detector and the central element of the experiment, with all auxiliary detectors and systems specified and designed in support of it. The DS-20k LAr TPC will use 50 t of LAr extracted from an underground source as the target material for WIMP detection. An ultra-pure acrylic vessel is used to contain the LAr. Features directly fabricated onto the inner surfaces of the acrylic vessel will form the TPC itself. These feature are the TPC field cage system, the anode and the cathode and are implemented on the acrylic panels with a commercial conductive polymer coating, called Clevios™. Use of this coating eliminates the use of metal conductive materials.

The same pure acrylic material, in the form of 4 mm thick sheets, is used to hold the Enhanced Specular Reflector (ESR) reflector foils installed to maximize light collection. The TPC is designed such that all the inner surfaces facing the active volume are coated with TPB, a wavelength shifter,

DS-20k TPC Dimensions	
TPC Drift Length	350 cm
Octagonal Inscribed Circle Diameter	355 cm
Total LAr Mass	51.1 t
Active LAr Mass	49.7 t
Fiducial Cut Distance (vertical)	70 cm
Fiducial Cut Distance (radial)	30 cm
Fiducial LAr Mass	20.2 t
Nominal TPC Fields and Settings	
Drift Field	200 V/cm
Extraction Field	2.8 kV/cm
Luminescence Field	4.2 kV/cm
Cathode Voltage	-73.8 kV
Extraction Grid Voltage	-3.8 kV
Anode Voltage	ground
Gas Pocket Thickness	7 mm
Grid Wire Spacing	3 mm
Grid Optical Transparency	97 %
SiPM PDM	
Number of PDM on TPC Top	4140
Number of PDM on TPC Bottom	4140
PDM Effective Area	50 × 50 mm <sup>2</sup>

TABLE I. DS-20k LAr TPC detector parameters.

to ensure the complete conversion of the 128 nm argon scintillation light to 420 nm, where the SiPMs' peak in their PDE. Two identical photosensor arrays of 4140 channels each are placed on top and bottom of the TPC, but outside of the acrylic vessel. The TPC is mounted inside a neutron veto detector, whose most important component is a 10 cm thick, gadolinium loaded, acrylic shell that completely encapsulates the TPC. This plastic shell defines two 40 cm thick active volumes, respectively named the inner and outer buffer, filled with liquid AAr. The buffers are further segmented with ESR, also coated with TPB. The whole apparatus is placed inside a light and electromagnetic shield barrier, contained in the ProtoDUNE-like cryostat filled with AAr.

**Sealed PMMA Vessel:** An acrylic (PMMA) vessel will be used to confine the UAr rather than a metallic vessel, since PMMA is extremely radiopure, resulting in a residual neutron background estimated to be  $<10^{-3}$  for the exposure of 200 t yr. As described above, the TPC active volume is confined in all directions by the sealed PMMA vessel that is formed by bonded plates or panels. In order to use the UAr more efficiently, all the UAr will be sealed in this PMMA vessel, so that no other external vessel will be required (as shown in Figure 8). The body of the PMMA vessel will be fused together by 5 cm thick acrylic plates, and then flanged and sealed with the top and the bottom lid, that serve as the anode plate and cathode plate of the TPC, respectively.

The ESR-acrylic reflector panels are located inside the acrylic vessel. The top and bottom PDM arrays are placed outside of the acrylic vessel, immersed in the AAr of the neutron veto detector. PDM arrays will be isolated from any light generated in the veto detector. In this way, 97.3 % of the total argon is active, resulting in the most efficient usage of UAr. All cables, HVFTs, and most mechanical structures are moved outside of the UAr volume as well, resulting in less outgassing and hence higher purity of the UAr.

The HV Cathode connection through the acrylic vessel is being studied and a new design will be tested to adapt the cable connection to the cathode itself. The acrylic vessel design integrates the HV connection so that the contact point is outside the vessel. In this case, both the HV cable and the HVFT are in the AAr volume. The HVFT will penetrate through the veto cryostat.

A commercial conductive and transparent Polymer coating, Clevios™, is found to be a very promising alternative to the traditionally used indium tin oxide (ITO) thin film coating. Clevios™ is being used in industrial applications such as transparent electrodes for touch panels and printed electronics. The main advantage of Clevios™ is its composition. Being a water-based solution, the large-area coating needed for the anode and cathode will be easier to accomplish with respect to an

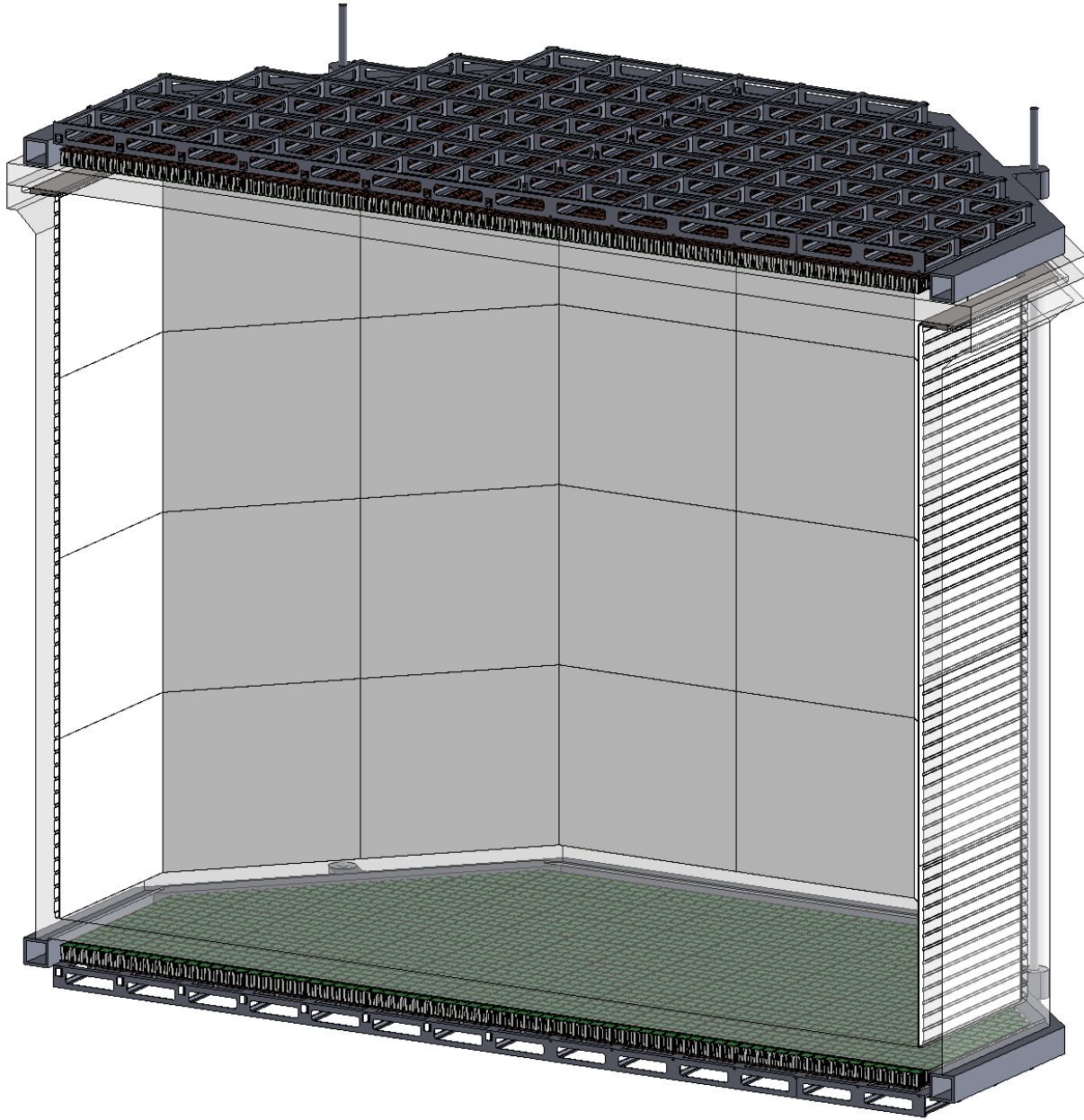


FIG. 8. Artist rendering of the PMMA vessel and the TPC.

ITO coating. A sample of 100 g has been procured for the radioactivity assay. The initial ICP-MS assay results from PNNL are encouraging, and further analysis of Rn emanation is scheduled at Krakow. In terms of the optics, three coating samples of Clevios<sup>TM</sup> on acrylic plates were provided by The Heraeus Company. The wet coating thickness of each sample is 4  $\mu\text{m}$ , 8  $\mu\text{m}$  and 12  $\mu\text{m}$ , respectively, and their transparency has been measured at Princeton University. A 1.5 % absorption at 420 nm was observed for a 4  $\mu\text{m}$  thick Clevios<sup>TM</sup> layer, which is a good result comparable to the 98 % transparency of ITO measured in DS-50. Further studies, including coated thickness resistivity, TPB coating on Clevios<sup>TM</sup>, and durability in LAr are ongoing. Besides the anode and cathode, the new design replaces the bulky copper field shaping rings with Clevios<sup>TM</sup> conductive coatings. Consequently, the use of this polymer will reduce the expected background, as well as the total cost, and make the fabrication and installation of the TPC simpler.

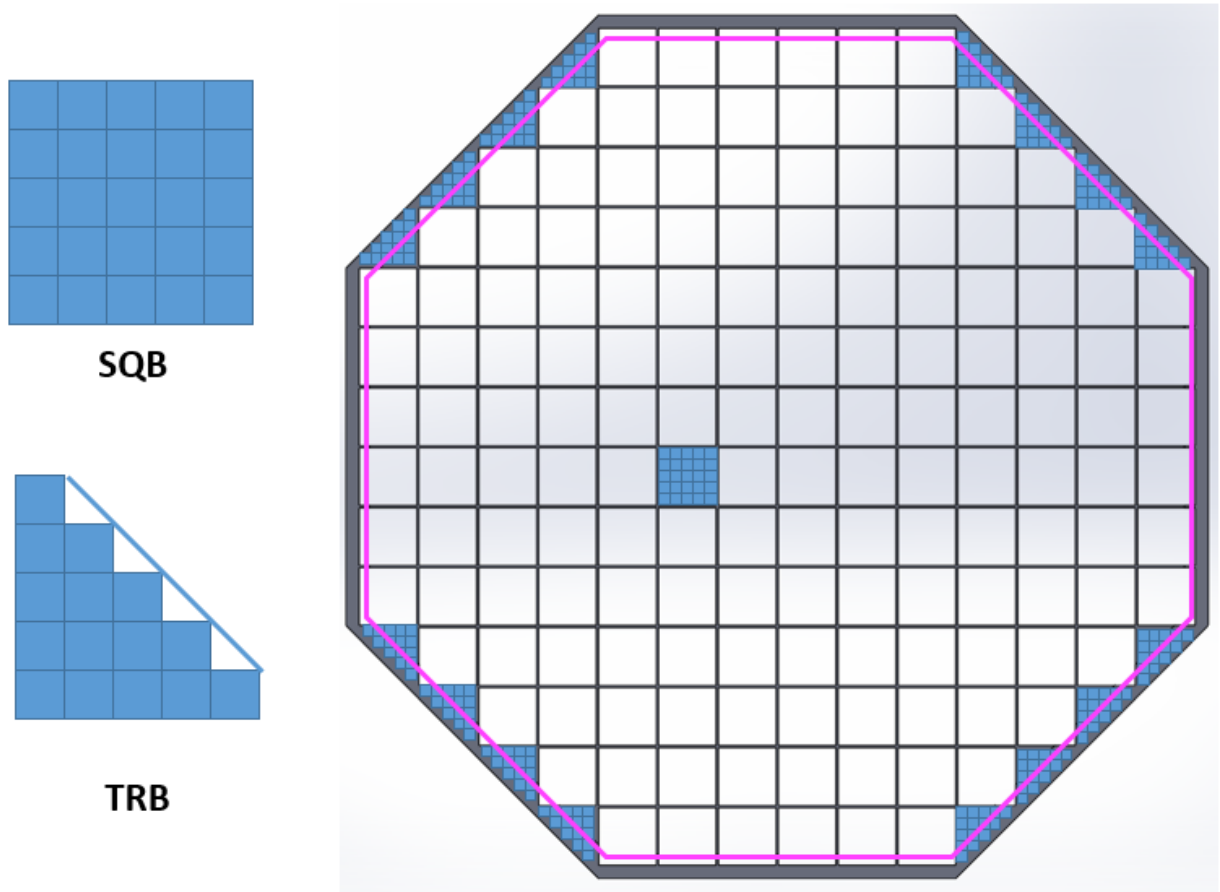


FIG. 9. Patterning scheme for the PDMs. Pink lines indicate the edges of the TPC active volume.

**LArTPC Size Consideration:** Since the SiPM tiles are all square shaped, the DS-20k TPC will be an octagonal shape to best fit the coverage of the PDM, while optimizing the fiducial mass. The size of the TPC is determined by the patterning strategy of the SiPMs, driven by the design size of the square and triangular motherboards (SQB and TRB, respectively). Figure 9 shows the current SiPM pattern strategy for both the top and bottom arrays. Each array consists of 156 SQBs and 16 TRBs. Each TRB contains 15 PDMs and each SQB contains 25 PDMs, as shown in Figure 10. Thus, the number of PDMs used in each array is 4140, while the total number envisioned in the TPC is 8280. Based upon this pattern strategy, and considering that the edge of the active volume of the TPC will shrink about 2.7 cm from the edge of the SiPM array, the distance from edge to edge of the octagonal active volume will be 355 cm. The height of the TPC will be 350 cm. With this design, the total mass of LAr in the active volume and fiducial volume (with 70 cm vertical and 30 cm lateral cuts) are 49.7 t and 20.2 t respectively.

**Reflector Panel:** In order to get rid of the conventional PTFE reflectors, which would be the predominant source of neutron background and Cherenkov background due to the enormous mass required for DS-20k, ESR foils will be used as the TPC reflector. The ESR is a thin layer foil which has reflectivity of 98 % for 420 nm light, with a thickness of only 50  $\mu\text{m}$ . In order to hold the ESR foils in place and maintain their flatness during the operations, 4 mm thick UVT acrylic sheets will be used. The thickness of the backside acrylic sheet is chosen to be 4 mm, providing the panels with enough strength to maintain the flatness of the ESR foils. The surface of each ESR foil facing the active LAr volume will be coated with TPB.

The entire reflector panel of the TPC is shown in Figure 11. The ESR mountings are strategically arranged such that no gaps can develop during the cool down of the TPC, hence guaranteeing 100 %

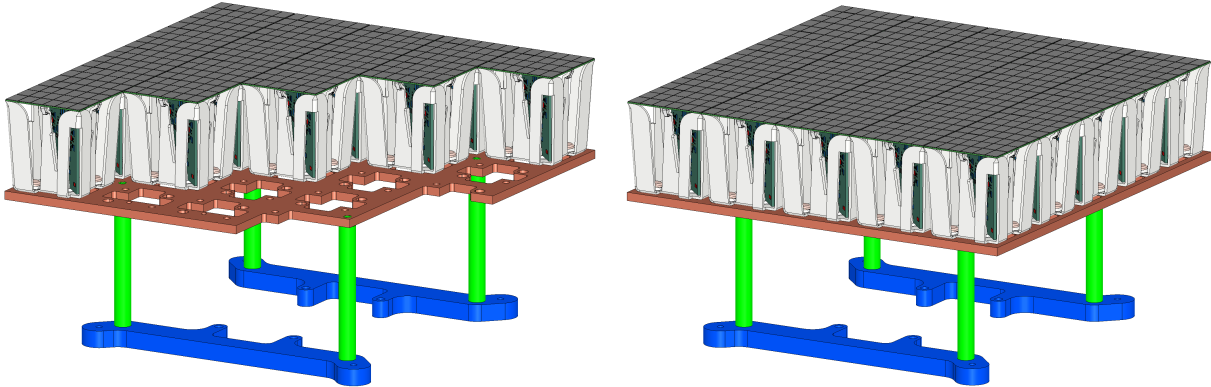


FIG. 10. Schematic drawings of the two types of DS-20k PDM motherboard arrangements. **Left:** triangular with 15 PDMs arranged for center and edge placement. **Right:** square with 25 PDMs.

TPB coverage. Each ESR-acrylic sub assembly will be fixed by several acrylic screws, with the screw heads facing the active volume. To avoid losing any light, each head of the screw will also be coated with TPB. By design, some space is left between the acrylic and the ESR to allow venting of any gas during the filling with LAr, but also to allow the LAr to fill the space between the back of the ESR and the acrylic panel. The flat and corner assemblies will be mounted on the field cage, which is attached to another set of acrylic structures by PTFE screws. The ESR holding panels are not connected at the corners in order to accommodate the shrinkage when the assemblies are cooled to LAr temperature. Overlaps between ESR foils at each joint are also designed for the same reason. A small mock-up to mimic the shrinkage has been built at UC Davis, whose results have confirmed the design concept. Repeated tests in liquid nitrogen showed that all parts moved in the desired way during cooling down and warming up, which proves the design idea.

**Field Region:** Within the sealed acrylic vessel, the electrode features of the TPC are realized using the Clevios<sup>TM</sup> conductive polymer coated directly onto the acrylic vessel. The inner surface of the acrylic vessel will be machined with grooves such that recessed areas have geometries similar to an electrode ring, and when coated with the Clevios<sup>TM</sup> comprise the TPC field-shaping rings that are highly uniform across the height of the TPC.

The relative permittivity of LAr and GAr are 1.54 and 1.03, respectively. By applying electric potentials of zero,  $-3.8\text{ kV}$ , and  $-73.8\text{ kV}$  to the anode, extraction grid and cathode, respectively, three different field regions are formed in the TPC:

- The uniform drift field of  $200\text{ V/cm}$  in the liquid phase, formed by the geometry of the field cage. The drift distance between the cathode Clevios<sup>TM</sup> layer and the extraction grid is  $350\text{ cm}$ ;
- The extraction field in the liquid phase above the grid is  $2.8\text{ kV/cm}$ . The distance between the extraction grid and the surface of the LAr is  $3\text{ mm}$ ;
- The electroluminescence field in the gas phase is  $4.2\text{ kV/cm}$ . The gas gap between the surface of the LAr and the Clevios<sup>TM</sup> layer acting as the anode is  $7\text{ mm}$  thick.

These values are based on the settings used for DS-50, while since the DS-20k gas pocket will be operating at a higher pressure, the extraction and luminescence fields will be scaled by the ratio of the electric field to the pressure of the gas pocket. The final values to be used will be confirmed with the DS-Proto detector that is designed to confirm final design choices for the DS-20k LAr TPC.

As the top boundary of the active volume, a  $5\text{ cm}$  thick acrylic window serves as the diving bell to maintain a stable gas pocket. A thin layer of Clevios<sup>TM</sup> conductive polymer is coated on the inner surface to act as the anode and a layer of TPB coated onto the Clevios<sup>TM</sup> layer to shift the scintillation light wavelength. The Clevios<sup>TM</sup> layer coating geometry is optimized for gas pocket electroluminescence field uniformity, as shown in the left panel of Figure 12. Right below the liquid surface is the extraction grid, composed of stainless steel wires (not shown in figure) stretched in parallel with  $3\text{ mm}$  spacing and held in place via small posts set into a stainless steel frame. Slots going in the radial direction and on the rim of the acrylic diving bell act as a concentric guide, to compensate the different thermal expansion coefficients between the acrylic and stainless steel

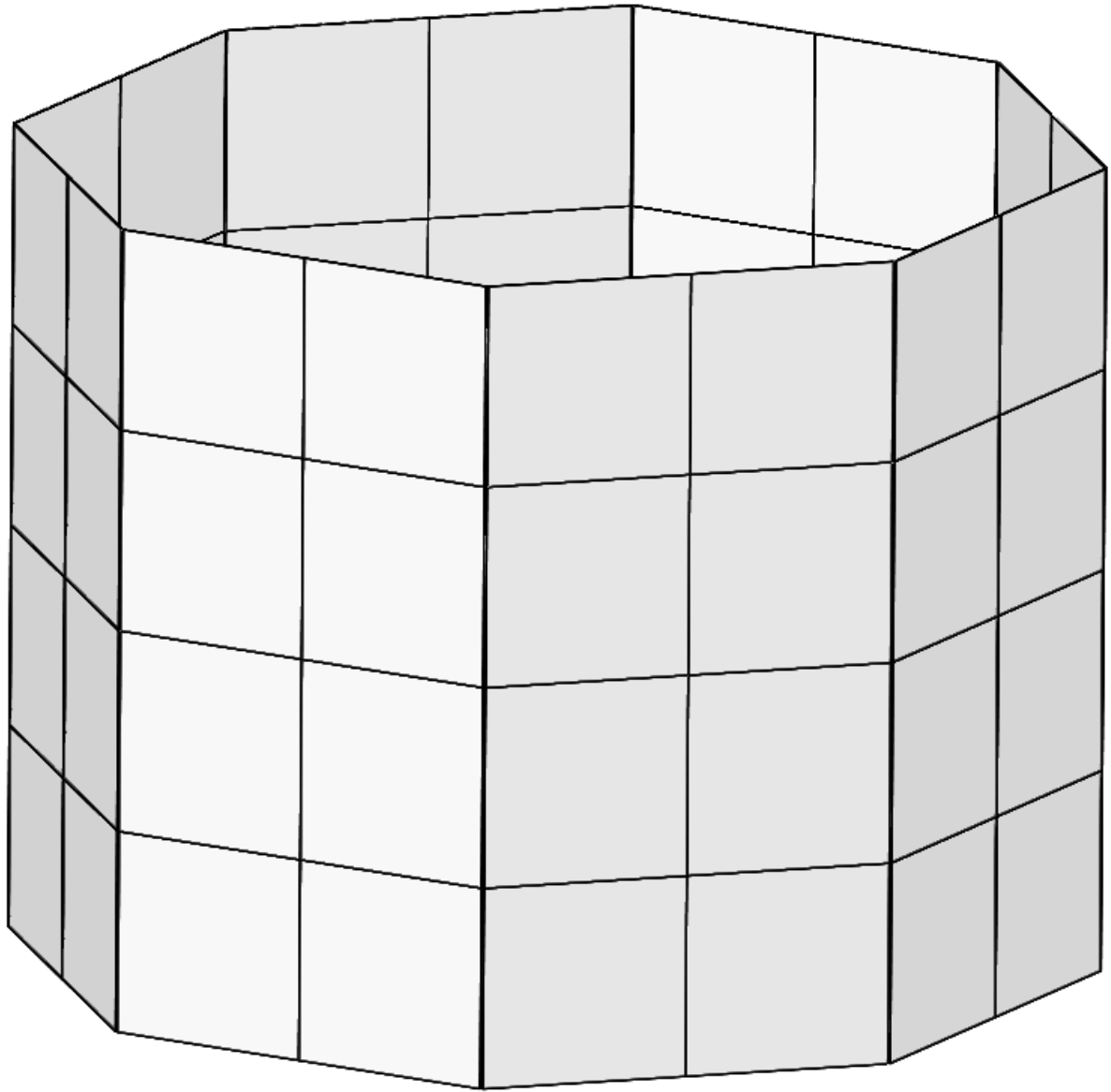


FIG. 11. 3D model of the full DS-20k LAr TPC reflector panels system.

while maintaining precise alignment. The LAr level will be maintained at the top surface of the grid frame. Suitable tensions will be pre-loaded on each of the grid wires to minimize the sagging, an effect that would distort the electroluminescence field. The frame must be stiff enough to sustain the total tension load of all wires, while having as little mass as possible. Both simulation studies and prototyping tests are well underway and have presented a feasible design for the extraction grid.

The bottom boundary of the active volume, shown in the right panel Figure 12, is a 5 cm thick acrylic window coated with a thin layer of Clevios<sup>TM</sup> on both sides. A layer of TPB will be coated on the top Clevios<sup>TM</sup> layer for wavelength shifting. The edge of the top Clevios<sup>TM</sup> layer is in contact with a C-profile feature on the walls of the acrylic vessel, which acts as a field shaping ring and smooths the electric field lines in the corner of the cathode region. Similarly, the bottom Clevios<sup>TM</sup> layer is in contact with a smoothing-profile solid guard copper ring to provide connection for the ground bias and electric field minimization. The 5 cm thick acrylic window can easily sustain

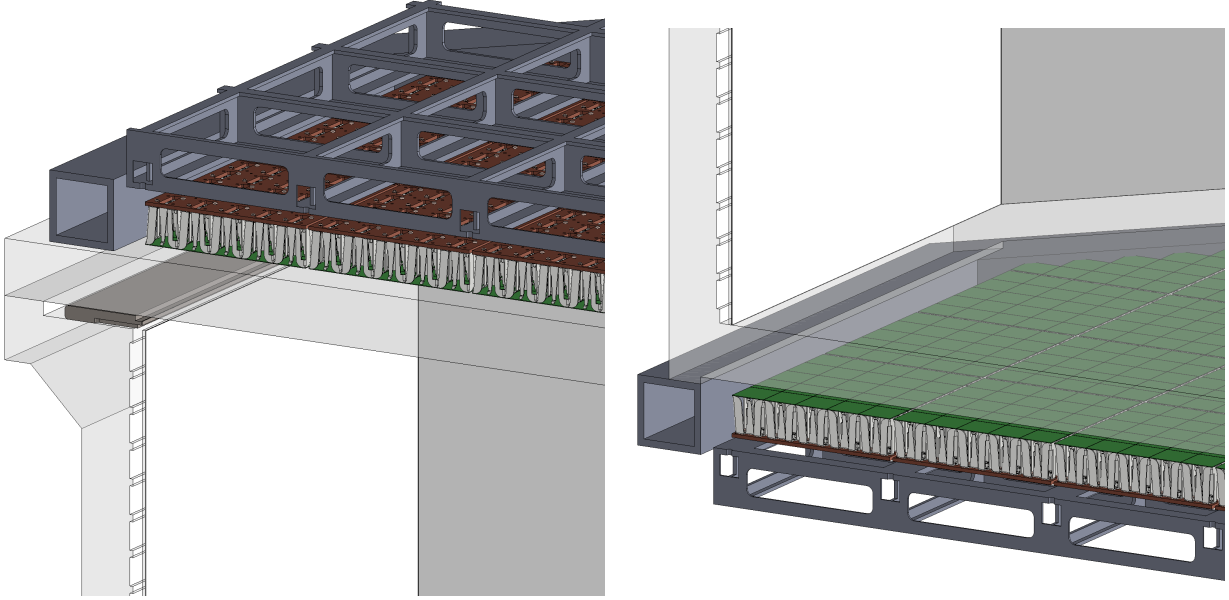


FIG. 12. **Left:** 3D model of the LAr TPC anode and extraction grid region. **Right:** 3D model of the LAr TPC cathode region.

the applied electric field with this design. Figure 13 shows the full field mapping modeled with the COMSOL Multiphysics software. Since the vessel is sealed, there is no path for HV to break through the acrylic at the cathode region. To confirm this, a full scale mock-up will be built to confirm the cathode HV delivery method around the acrylic vessel bottom. The bottom surface of the cathode acrylic window will have a convex shape to avoid bubble accumulation. Any bubbles generated by the bottom photon detector array, or any other parts, will be driven outwards and rise to the top of the AAr cryostat.

A one tonne-scale prototype with full features of the DarkSide-20k TPC will then be built to validate the design comprehensively. General considerations, such as the requirements of surface and bulk contamination, coating procedures, handling and bonding of acrylic, are based on knowledge available within the GADMC. Detailed plans and procedures are currently being developed. All mock-up designs and tests will use final DS-20k geometries and full size components in order to confirm the validity of the final DS-20k mechanical design and functional parameters. The DS-20k LAr TPC parameters are summarized in Table I.

### 3.2. Cryogenics

The main system parameters of the cryogenics system are given in Table II. The parameters that are listed in bold are considered to be system requirements, most often driven from experience gained during operations of the DS-50 cryogenics system.

The cryogenics system is derived from the successful scheme of the DS-50 cryogenics and gas handling system. Additional lab tests, already performed over the past 4 years, demonstrated individual or integrated features required for the performance of the control system and the safety of the large amount of UAr in the DarkSide-20k system. A full P&ID diagram is already developed as shown in Figure 14. There are two major linked systems: one for the AAr in the veto shield inside the ProtoDUNE cryostat and one for the UAr in the sealed acrylic vessel for the LAr TPC. The AAr cryogenics system can be the same as the demonstrated ProtoDUNE system already built at CERN, or an optimized version specific for the LNGS installation. The UAr cryogenics system for the TPC will be an upgraded system based on DS-50. The ProtoDUNE cryostat is a passively insulated system so that its thermal load is not subject to the availability of the electric

Parameter	Value
<b>ProtoDUNE Cryostat parameters for AAr</b>	
ProtoDUNE Cryostat inner width	8548 mm
ProtoDUNE Cryostat inner height	7900 mm
LAr height in ProtoDUNE Cryostat	7500 mm
Total AAr in ProtoDUNE Cryostat	700 t
ProtoDUNE Cryostat insulation per unit area	6.5 W/m <sup>2</sup>
Thermal Heat Load of ProtoDUNE Cryostat	2.7 kW
TPC PDM Cold Electronics Power	1.5 kW
Veto PDM Cold Electronics Power	0.5 kW
AAr System Design Mass Circulation Speed	10 000 std L/min
Minimum heat recovery efficiency of AAr heat exchanger	>95 %
AAr Turn Over Time	30 d
Total Cooling Power Required	10 kW
LAr boiling threshold at 3 m depth	60 mW/cm <sup>2</sup>
Minimum AAr condenser cooling power to hold LAr inventory	2.7 kW
ProtoDUNE AAr top pressure	1.075 bar
<b>TPC Cryogenics Parameters for UAr</b>	
Total UAr mass during normal operation	51.1 t
TPC UAr Cryogenics Design Mass Circulation Speed	1000 std L/min
Minimum heat recovery efficiency of UAr heat exchanger	>95 %
UAr Turn Over Time	20 d
Total Cooling Power Required for UAr	500 W
UAr Turn Over Time	20 d
UAr electron lifetime required for stable S2 generation	>5 ms (<0.01 ppb O <sub>2</sub> equiv.)
Pressure stability achieved in DarkSide-50	0.023 psi (RMS)
Nominal flow rate of single DarkSide-20k GAr circulation pump	500 std L/min
Total mass of LN <sub>2</sub> storage in cooling system	30 t
Efficiency of radon purification by activated charcoal trap	<2 $\mu$ Bq/kg after trap
Maximum required helium leak rate at all welds and joints	$2 \times 10^{-9}$ std cm <sup>3</sup> /s

TABLE II. DarkSide-20k cryogenics system parameters.

power. Liquid nitrogen is the primary cooling source of the entire cryogenics system. A minimum storage of the liquid nitrogen is maintained such that the system will be protected during power failure mode. A full scale version of the condenser box for the underground argon has already been designed and all parts procured. The cryogenics test of the condenser is planned at the CERN cryogenic division in summer 2019.

Heat exchangers are strategically placed throughout the system for LAr filling and LAr removal at the various required speeds for the different operational modes. The continuous argon circulation for purification is driven by a set of specialized gas argon pumps (developed within the collaboration). Combined with the integrated heat exchanger systems, the system can handle high circulation rates (10 000 std L/min AAr, and 1000 std L/min UAr) drawing either, or both, liquid and gas phase argon to effectively remove electronegative impurities. The designed P&ID system allows the use of SAES hot getter to effectively remove N<sub>2</sub>, CO<sub>2</sub>, and O<sub>2</sub>. The total cooling power of the cryogenics system is designed to handle the total heat load from the power dissipated by the cold electronics operating inside the liquid argon volume.

The cryogenics system for the LAr TPC in DS-20k shares the same principle as that fully demonstrated in DS-50, which has been running smoothly for five years. The long-term TPC pressure stability, an essential parameter for S2 resolution, has been achieved with incredible success, quantified as 0.023 psi RMS. A drift electron lifetime of  $\geq$ 5 ms has been achieved, resulting in an oxygen contamination in LAr of less than 0.01 ppb, which is greatly beneficial to the low-mass dark matter search, as recently published in [13, 14]. The immunity to total power failure (including UPS system failure), as tested in the commissioning phase and verified by a recent accident of total LNGS blackout, secures the safety of the entire LAr TPC, especially the valuable UAr.

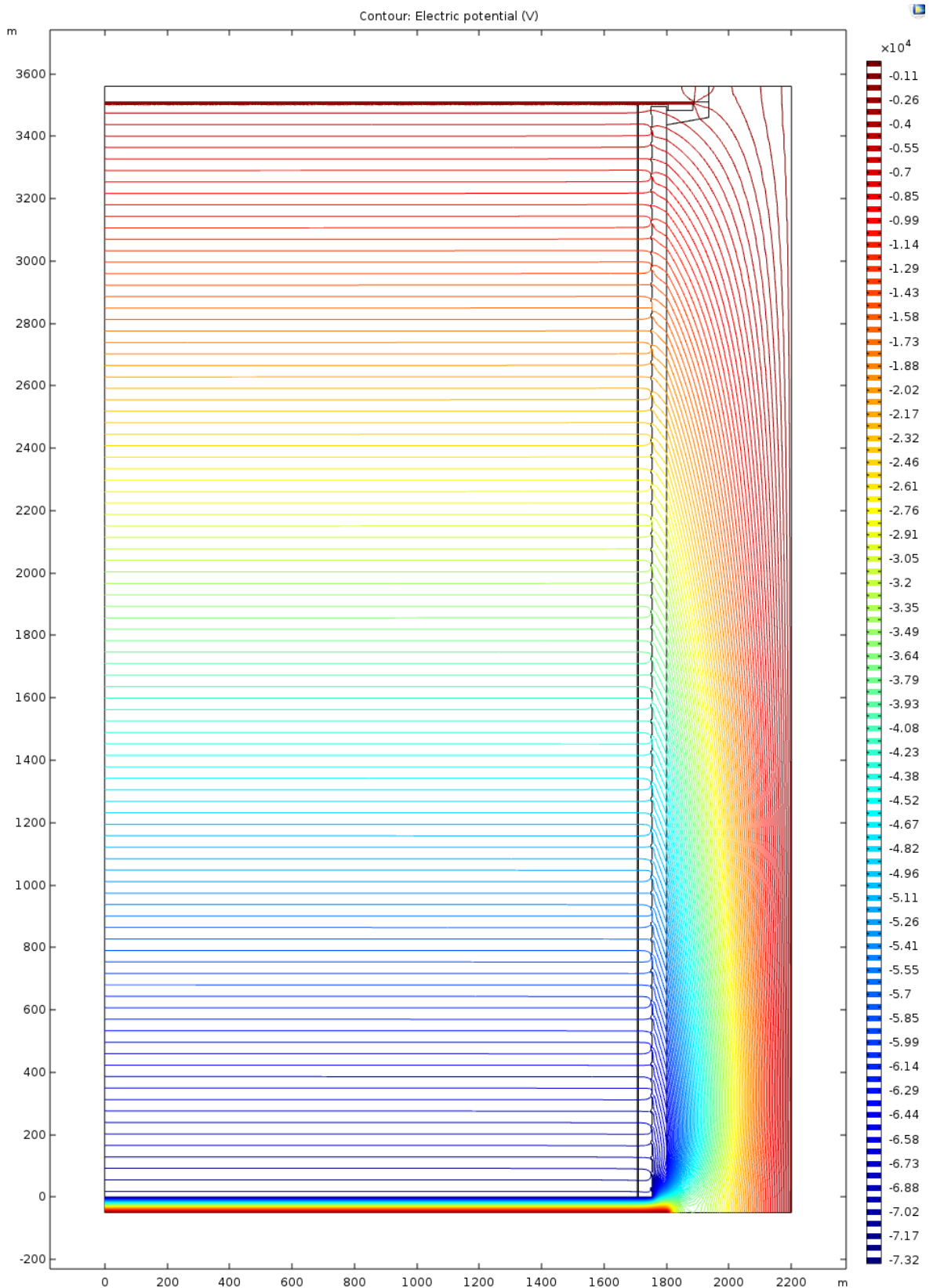


FIG. 13. Equipotential lines mapping in the DS-20k TPC showing an extremely uniform field distribution, modeled with the COMSOL Multiphysics program. Parameter settings for the calculation are those defined in Table I.

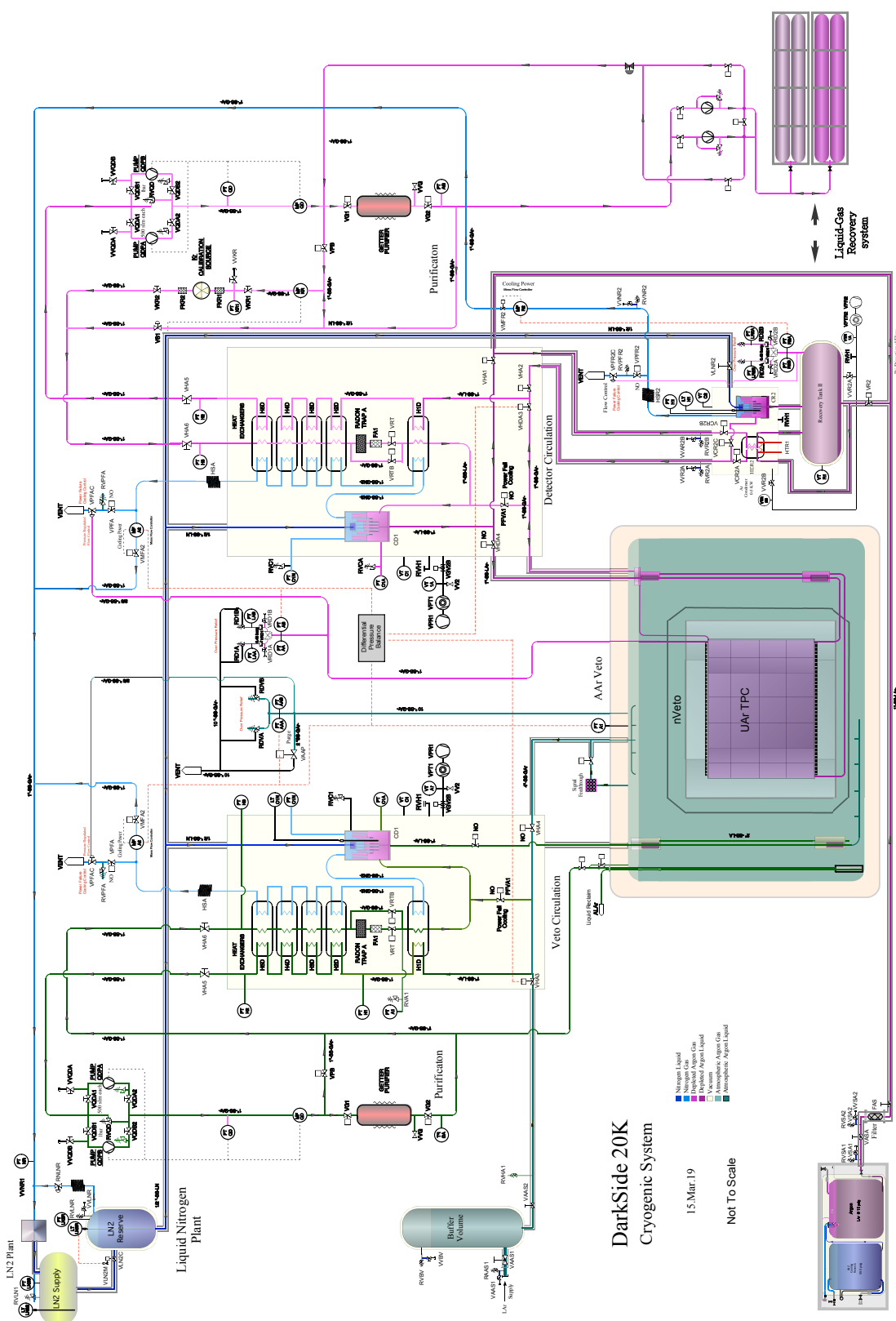


FIG. 14. DS-20k cryogenics system P&ID.

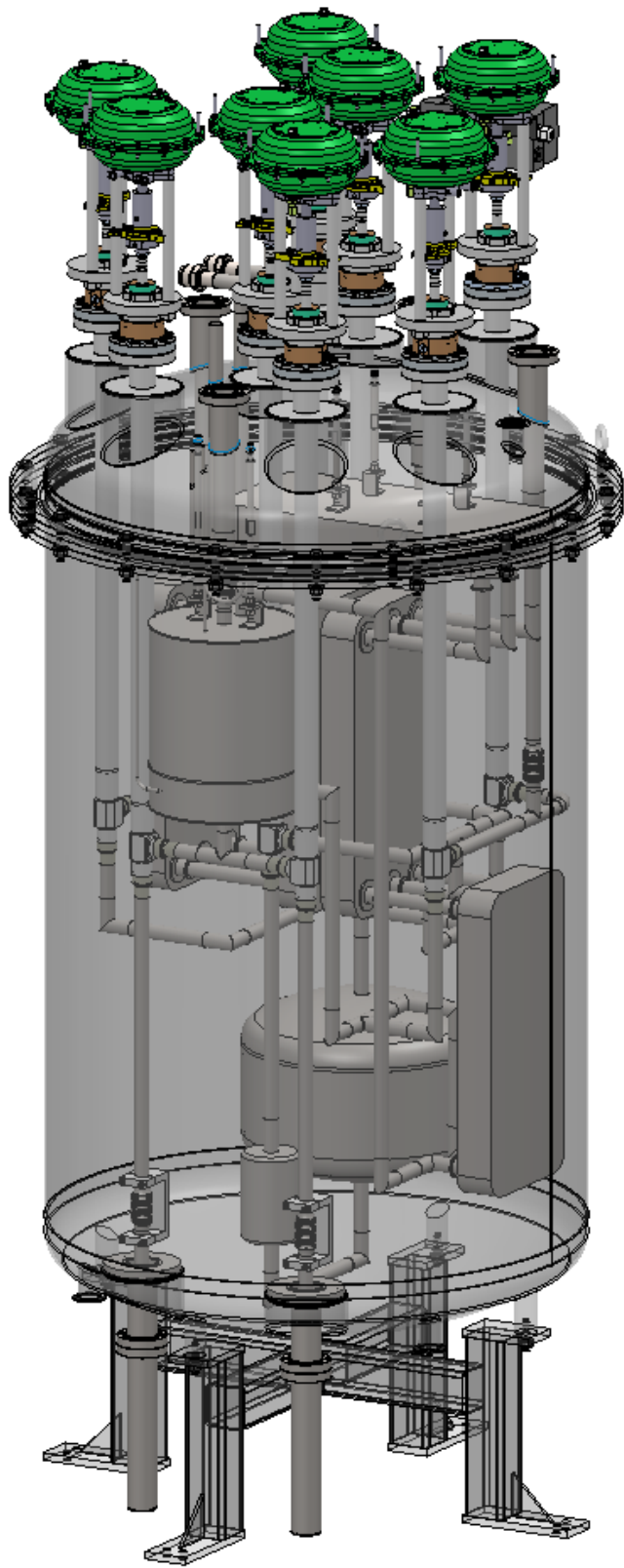


FIG. 15. DS-20k condenser box.

The features of the DS-50 cryogenics system are fully implemented into the DS-20k system, not only by simply scaling up the argon volume, but also upgrades based on experience and lessons learned. A major improvement is to increase the circulation speed to the required 1000 std L/min, to initially reach the purity requirement of LAr in a couple of turn-over times of 20 d. Another major improvement is to increase the cooling power needed to accommodate such a large circulation speed. A full-size prototype LAr condenser, the core component in the cryogenics system, has been built and tested at UCLA, and a cooling power of 2.2 kW (latent heat only) has been achieved, nearly twice that needed for the DS-20k UAr cooling requirement. The main components of the UAr cryogenics system condenser box have already arrived at CERN and are ready for welding and the first test to follow in summer 2019.

The UAr cryogenics system is made up of several sub-systems (while the AAr system will be similar except at larger scale in volume and power, but with lower requirements on purity): the liquid argon handling system, the liquid nitrogen reserve system, the purification system, the cold box, the gas circulation pump, the recovery and storage system, the integrated heat exchanger system, and heat exchangers close to the TPC. The overall schematic is shown in Figure 14, including the AAr cryogenics system for the veto detector, which employs the same principle. Two cryogenics systems share the same liquid nitrogen reserve loop, but have separate argon loops of UAr and AAr, respectively. Also shown in the figure is the condenser box integrated with the heat exchangers and inline radon trap.

The LAr handling system delivers the clean radon-free UAr, which is initially stored in the recovery storage system capable of storing the full target of UAr for DS-20k. Two options are being considered, full liquid phase storage or gas phase high-pressure storage. The gas handling system will be adopted to either solution in order to pre-purify the UAr before filling the TPC volume. The system is also designed such that the UAr can be recuperated from the inner detector to the recovery system, as needed, if an emergency occurs or at the end of the experiment.

The LN<sub>2</sub> reserve system is a closed loop with a LN<sub>2</sub> plant located outside of Hall C and a few local liquid nitrogen dewars. The system delivers liquid nitrogen as the source of cooling power to the condensers in the inner detector UAr cryogenics system, the AAr cryogenics system, and the recovery system, if liquid phase storage is chosen, and recuperates the boiled-off nitrogen gas to liquify it back into the LN<sub>2</sub> system. The UAr purification system purifies the argon in gas phase during the circulation. A commercial SAES getter system has already been proven to work well in DS-50 and an identified model with increased circulation capability will be used in DS-20k.

The cold box, as shown in Figure 15, is one of the key components of the DS-20k cryogenics system, which contains all the major cryogenic handling components. Apart from the condenser, the cold box contains five heat exchanger modules to efficiently pre-cool the argon gas by cold nitrogen gas and cold outgoing argon gas. In this way the necessary cooling power is reduced dramatically. The radon trap is placed between the coldest and the second coldest heat exchanger modules to ensure that the argon passing through is still in its gas phase, while at its lowest temperature, which maximizes the radon removal efficiency. Eight cryogenic valves and several temperature and pressure sensors are also installed to control and monitor the system. Tubings are chosen as 1" OD stainless steel, in order to accommodate the argon circulation speed up to 1000 std L/min.

The stainless steel LAr condenser contains 127 0.5" OD top-sealed tubes finely patterned on a thick plate as the thermal exchanging part of the condenser. The condenser is therefore separated into the nitrogen volume on the top and the argon volume on the bottom. A so-called *chicken feeder* is mounted at the end of the liquid nitrogen delivery tube to maintain a continuous liquid nitrogen dropping. The flow of the evaporated nitrogen gas is monitored by a mass flow meter and adjusted by a control valve, both located at ambient temperature. The control valve uses the LAr TPC pressure from both UAr and AAr as feedback signal to automatically adjust the evaporated nitrogen gas flow rate, which is essentially the cooling power of the condenser, hence in return maintains the LAr TPC pressure at the desired set point and balanced with AAr system with an incredible stability, as demonstrated in DS-50.

Based on the successful demonstration of the gas circulation pump in DS-50, which provides a

speed up to 50 std L/min, the gas circulation pump of DS-20k uses the similar design, relying on two components: linear motors and reed valves. The linear motors, consisting of a piston and cylinder pair, can provide a continuously adjustable pumping power. The reed valves guide the gas flow direction when the linear motors going back and forth. Two balanced linear motors will be placed face to face, to counteract the vibration produced during the motor operation. The combination of the linear motors and the reed valve allows the pump to work in a frictionless condition, resulting in a long lifetime. The initial fast circulation requires a speed of 1000 std L/min to achieve a good UAr purity level, and then the circulation speed can be decreased to only maintain the purity and stability. This minimum flow could be very low since the UAr system essentially is embedded in the AAr system while all cold electronics are outside the UAr volume so no cooling power is required. To achieve such a high circulation speed, flexibility of operations, as well as the ease of the pump development, two individual circulation pumps will be placed in parallel, each providing a circulation rate up to 500 std L/min. A full-size prototype circulation pump has been fabricated at UCLA and Princeton, and passed the initial tests. It was shipped to CERN and is being certified for the EU safety requirement. Once fully tested, it will be integrated into the prototype cryogenics system for the full-system test.

The heat exchangers close to the TPC are basically large heat exchangers using many tubes as the thermal exchanging parts, similar to the concept of the LAr condenser described above, but with a much increased thermal exchanging surface area. Outgoing LAr from the LAr TPC absorbs heat from the incoming liquid-gas mixture of purified argon here, boils off into gas phase, and then enters the circulation loop. This heat exchanger is located above the LAr TPC and ensures that all outgoing argon above it will be in gas phase, avoiding otherwise a large argon head height coming directly from the LAr TPC to the lowest heat exchanger modules in the cold box. This would result in an argon pressure below its triple point at some point in the argon loop and causing argon to freeze. Another set of near TPC heat exchangers are strategically placed close to bottom level of the UAr TPC for fast recovery during the draining stage. This lower level heat exchanger is completely passive during normal operations and only useful during the draining phase. The entire near TPC heat exchangers are immersed in LAr inside the ProtoDUNE cryostat, which serves as a thermal bath for them.

The integration and tests of the full scale UAr cryogenics system at CERN is ongoing. The first pass FEA engineering has proven the design load is as anticipated and fabrication is officially approved. All condenser box components, large pneumatic cryogenics valves and associated auxiliary components are on site at CERN for integration. The full scale cryogenics test of the DarkSide-20k UAr system will be performed over the summer of 2019.

#### 4. MATERIAL ASSAYS

Trace radioactivity in detector materials can be a dominant background for the direct dark-matter searches. In addition to this bulk contamination, a major source of background can be caused by the cosmogenic activation of the materials and by the surface contamination (due to radon diffusion and plate out of the radon daughters produced in the surrounding air). Beta and alpha particles produced by the radionuclide decays can typically contribute to the background only if the atom is in contact with the LAr target, while gammas and neutrons, the last ones from spontaneous fission and  $(\alpha, n)$  interactions, can produce background from more distant sites.

A strategy for selecting the materials, as well as machining, storing, transporting and mounting the detector components, is mandatory in order to control the backgrounds and to maximize the physics reach of DS-20k. This will be accomplished by developing the “background budget” to identify materials’ purity requirements. In addition to the assays on the raw purchased materials, performed to identify the right technologies and compositions, we are developing cleaning and handling procedures to meet radiopurity standards, and performing assays to validate processes for the construction and commissioning of the detector and its components.

In DS-20k this responsibility is delegated to the Materials and Assays Working Group (M&A WG),

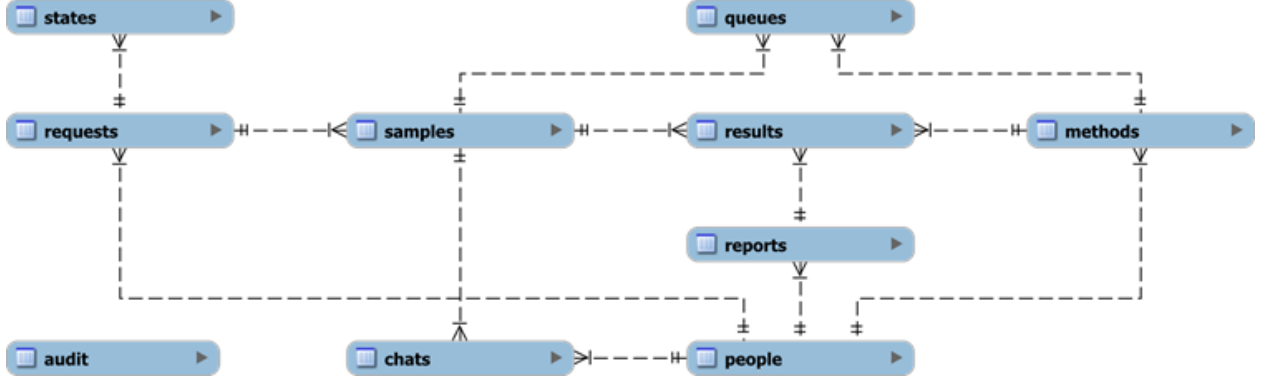


FIG. 16. A simplified DS-20k materials database structure. Information on each relevant aspect of the assay process is stored in the database, facilitating the management of the whole assay process.

a single Working Group within the collaboration, comprised of experts in each of the assay methods and representatives from each institution that hosts assay capabilities. The group coordinates and schedules the assays according to the pre-evaluated radiopurity requirements, the urgency, the capacity of the available assaying resources and their queue.

The goal is to assay and approve *all* materials or items selected to reside within the cryostat, particularly by scrutinizing the entire  $^{232}\text{Th}$  and  $^{238}\text{U}$  decay chains. This calls for multiple assays with multiple techniques for each sample, as different techniques are applicable to different sub-chains of the  $^{232}\text{Th}$  and  $^{238}\text{U}$  decay chains. These results are combined with the  $(\alpha, n)$  cross-sections, calculated according to the chemical composition of the material in order to extract the neutron yield expected in the detector.

#### 4.1. Radio-purity database

The need for fast access to, and exchange of data between different Working Groups (WG) is addressed by the DarkSide Materials Database (MDB). Information on the radioactive content of materials to be used for DS-20k construction is stored therein, and is crucial for the comprehensive estimation of the background budget for the experiment. The MDB contains all the relevant information about samples: chemical composition, origin (production batch), data-sheets, pictures, part of the detector where it will be placed, history of assays etc. This information is included in the total background budget estimation and carefully evaluated. Rules for handling and cleaning of samples, developed and verified during the screening process, are also stored in the database. Later, during the detector construction and integration, reproducible results of the estimated internal background may be expected upon application of the provided handling and cleaning procedures.

The database helps to systematize the radioactive background budget estimation, material selection and tracking, assay prioritization, and cleaning and handling methods. Additionally, the database is also used to balance the workload and assay resources between numerous institutions involved in the task by coupling assay needs with assay capabilities of members of the Materials WG.

The MDB structure reflects the flow of the material assay process, aiding material selection and application during the construction phase of the experiment. The database consists of several cross-related tables, holding information on the status of the assay requests, screening methods, samples, assay results and people (institutions) involved (see Fig. 16). It also keeps track of the queues in different facilities, and the history and the current status of any assay performed within the M&A WG. A convenient web-based interface is provided for the users (see Fig. 17), dedicated to: ease submission of new assay requests from other Working Groups; browse and report of the assay results (including uploading the results); and to manage the assay status of the samples and queues at different facilities.

Sample name		Description		Batch		DS-20 reference		Search ▾							
Show 25 entries				Copy CSV Hide empty Show all Column visibility ▾				Search: capa							
ID	Report	Name	Reference	Method	Sample	Date	$^{60}\text{Co}$	$^{137}\text{Cs}$	K	$^{40}\text{K}$	$^{234m}\text{Pa}$	Pb	$^{210}\text{Pb}$	$^{210}\text{Po}$	$^{226}\text{Ra}$
1910	253	Capacitor 22pF	273 Non-satisfactory	PDM module	HPGe GeDSG (Matthias Laubenstein, LNGS, INFN),	complete	2018-12-13	<6 [mBq/kg] (3 sigma)	<6 [mBq/kg] (3 sigma)	1.5±0.7 [Bq/kg] (1 sigma)	<1 [Bq/kg] (3 sigma)				<1 [Bq/kg] (3 sigma)
36	5	Panasonic SMD capacitors	5 Decision pending	PDM module	HPGe GeCris (Matthias Laubenstein, LNGS, INFN),	complete	2017-12-14	<2 [mBq/kg]	<4 [mBq/kg]	<1 [Bq/kg]	<2 [Bq/kg]				<6 [mBq/kg]
1854	246	Panasonic capacitors	57 More assays needed	PDM module	HPGe BEGe (Matthias Laubenstein, LNGS, INFN),	complete	2018-08-30	<7 [mBq/kg]	<5 [mBq/kg]	<2 [Bq/kg]	<7 [Bq/kg]				<0.2 [Bq/kg]

FIG. 17. Interface web page, presenting a selection of assay results for various types of capacitors. The database is also used to manage the assay process of each sample.

Assay results obtained for the materials used for DS-50 were also imported to the new database. Currently the database stores almost 2000 assay results (more than 120 assays performed since 2017) of nearly 300 samples, and counts (see Tab. III). The M&A WG has established protocols to efficiently handle the radioactive budget of the experiment.

#### 4.2. Managing Assay Capabilities

To ensure the radiopurity of all detector materials to the levels defined by the background model, the M&A WG has developed a radiopurity assay program that takes advantage of facilities throughout the collaboration. Overall, it is anticipated that this program will span approximately three years and will involve around a thousand more assays, including searches for radiopure materials, development and validation of cleaning and handling procedures, and screening of all detector components. The collaboration has extensive and diverse assay capabilities that are sufficient to complete this program on schedule, with extra capacity to handle additional unforeseen assays. Estimates of the capacity available to DS-20k for each assay type are summarized in Tab. IV. The assay challenges are organized into six focus areas: mass spectrometry (ICP-MS), radon emanation, direct gamma assay (HPGe), surface assays (alpha activity), cosmogenic activation and materials handling and process development.

#### 4.3. Radioactive budget

The radioactive budget states the expected background of everything that goes into the detector, taking into account material's (element) radiopurity, mass, composition, shape and location. These parameters are the input of Monte Carlo simulations, performed using a Geant4-based package written within the collaboration and called G4DS. The result of the simulation is the efficiency of our detector for rejecting the background coming from different sources, either because of geometrical reasons or because of active tagging of undesired events. The neutron budget is calculated on a single-element basis, so the mentioned inputs (radiopurity, composition and the position in the detector) are needed for every component of the detector.

The most critical requirement in terms of radiopurity is given by the  $\alpha$  activity, mainly caused by the naturally occurring radioactive chains of  $^{232}\text{Th}$  and  $^{238}\text{U}$  and potentially producing neutrons through  $(\alpha, n)$  reactions. The cross section of this reaction is calculated using the *neucbot* program,

Assay Method	Number of assays
ICP-MS	50
Germanium spectroscopy	40
Chemical extraction of Po	20
Surface $\alpha$ 's counting	5
Radon emanation	5
Other	3

TABLE III. Summary of the assays performed since 2017 in preparations of the DS-20k construction, with breakdown by assay method.

Assay Method	Capacity [assays per year]
ICP-MS	60
Germanium spectroscopy	35
Chemical extraction of Po	20
Surface $\alpha$ 's counting	10
Radon emanation	10

TABLE IV. Summary of the assay capabilities available for DS-20k.

where the energy spectrum of neutrons is generated as well. Hence, the (chemical) composition and construction of each component needs to be known with sufficient detail in order to calculate the interaction cross-sections correctly.

Provided that some construction elements may be in similar locations, and that a component may be used in different places, a cross-linked, multi-tab spreadsheet is used to calculate the expected neutron budget. Propagation of any modifications or updates in a coherent way is easy to maintain. A summary of background budget components is tabulated in a user-friendly form, collecting all the relevant information structured following the same organization scheme as the Working Groups in the collaboration (Veto, TPC, PhotoElectronics, etc). M&A WG is in close cooperation with other WGs through dedicated group representatives, aiding selection of proper construction materials at the early stages of the design. The background budget is constantly evolving and converging as the material assay campaign progresses, such that more components' activities are determined. It is estimated that over 1000 more assays will be performed until the completion of the detector construction, for more than 150 expected material samples.

## 5. CALIBRATION

Calibrations for both the TPC and the Veto range from low-level detector issues, such as the single-photoelectron response of individual photosensors, to high-level physics issues like the acceptance as a function of energy for nuclear recoils. The combination of radioactive sources, neutron generators, and light sources ensures a robust calibration plan to reach ultimate science goals of DS-20k.

### 5.1. Distributed Gas Sources

Full volume calibration of the TPC will be achieved with distributed gas sources:  $^{83m}\text{Kr}$  and  $^{220}\text{Rn}$ . Gas sources are simple to implement, since they are added to the argon recirculation stream and feature short halflives, quickly decaying out from the argon target volume. The monoenergetic decays of  $^{83m}\text{Kr}$ , distributed through the active volume of the TPC, can give a key calibration point in the WIMP recoil energy region. The 3D reconstruction of events in the TPC allows a full mapping of position-dependence of the light yield using the  $^{83m}\text{Kr}$  source. This means that, while broad dissemination through the active volume is important, a uniform distribution is not required.

The  $^{83m}\text{Kr}$  decays quickly ( $\tau = 2.64$  h) to a stable nuclide and causes no long-term contamination or background to the WIMP search. The DS-20k  $^{83m}\text{Kr}$  source is based on the source used successfully in DS-50. A tiny droplet of a solution of  $^{83}\text{Rb}$  ( $\tau=124.4$  d) is adsorbed into a piece of charcoal, which, after drying, is placed between two particulate filters in a branch of the argon recirculation system which is normally isolated by valves and can separately be pumped to vacuum. In DS-50, an initial 8.5 kBq of  $^{83}\text{Rb}$  gave a  $^{83m}\text{Kr}$  trigger rate of hundreds of Hz, even though the flow subsequently passed through a cooled radon trap. In DS-20k, the challenge will be to get the  $^{83m}\text{Kr}$  broadly distributed in the 49.7 t active mass before it decays. To further this, LAr will be returned to the TPC after repurification via numerous tubes whose endpoints will be distributed over the surface area of the TPC side panels.

$^{220}\text{Rn}$  and its short-lived daughters produce several  $\gamma$ -rays,  $\beta$ 's, and  $\alpha$ 's of various energies, making it an attractive distributed calibration source that can be implemented in a similar manner as the  $^{83m}\text{Kr}$  source, except for the need to bypass the charcoal trap before insertion into the gas stream. The source of  $^{220}\text{Rn}$  may be prepared as an electroplated  $^{228}\text{Th}$  on stainless steel or copper. Enclosed in a small metal-sealed and vacuum-tight volume equipped with a VCR/CF port. The advantages of the  $^{220}\text{Rn}$  source are the following:

- $^{220}\text{Rn}$  and its daughters are short-lived, the longest half-life in the chain is 10.6 h for  $^{212}\text{Bi}$ , therefore the activity introduced into the detector will disappear after a few days;
- The high energy alphas appearing in the chain (6.05 MeV, 6.09 MeV, 6.29 MeV, 6.78 MeV, and 8.78 MeV);
- The coincident  $^{220}\text{Rn}$ - $^{216}\text{Po}$  and  $^{212}\text{Bi}$ - $^{212}\text{Po}$  decays will allow to study the homogeneity of the distributed sources, and possible LAr flow patterns as well as potential “dead volumes” that are not affected by the LAr circulation;
- Drift of the charged ions inside the LAr volume (interesting also with respect to Po isotopes from the  $^{222}\text{Rn}$  chain);
- Low-energy  $\beta$ 's appearing in the chain may be used for calibrations of the low-energy response of the detector.

To avoid removal of the  $^{220}\text{Rn}$  source by the charcoal trap it should be bypassed during the calibration run. Release of  $^{220}\text{Rn}$  from the source should be done in a way that avoids contamination of the detector with residual  $^{224}\text{Ra}$  (half-life 3.6 d) or  $^{228}\text{Th}$  (half-life 1.9 yr). A similar risk exists for the  $^{83m}\text{Kr}$  source, but has been thoroughly mitigated and never observed.

## 5.2. Gamma Sources

Three external  $\gamma$ -ray sources,  $^{60}\text{Co}$ ,  $^{133}\text{Ba}$ , and  $^{137}\text{Cs}$ , are planned for use in the TPC calibration. The combination of these sources in the absence of  $^{39}\text{Ar}$  gives an excellent calibration of the electron recoil PSD band, energy scale and provide valuable data for tuning of the detector response in the Monte Carlo simulation. The  $\gamma$ -ray sources were chosen to span the energy range of interest in combination with the distributed  $^{83m}\text{Kr}$  source: 41.5 keV for  $^{83m}\text{Kr}$ , 122 keV for  $^{60}\text{Co}$ , 356 keV for  $^{133}\text{Ba}$ , and 662 keV for  $^{137}\text{Cs}$ . Sources will be miniature in size to be inserted inside the source guide tube for TPC, the overall design of which is shown in Figure 18.

## 5.3. Neutron Sources

Neutron sources are of particular interest for calibration of the nuclear recoil PSD band and the efficiency of the neutron veto, a key feature of the DS-20k design. Small ( $\alpha,n$ ) sources such as  $^{241}\text{AmBe}$  and  $^{241}\text{Am}$ - $^{13}\text{C}$  will be fabricated for this purpose.  $^{241}\text{AmBe}$  is utilized as a tagged neutron source utilizing 4.4 MeV gamma in 56 % cases.  $^{241}\text{Am}$ - $^{13}\text{C}$  can serve as a gamma-free source for Veto neutron calibration, after slowing down alphas for ( $\alpha,n$ ) reaction to always produce daughters in the ground state. Sources will be small in size to be delivered with the source guide.

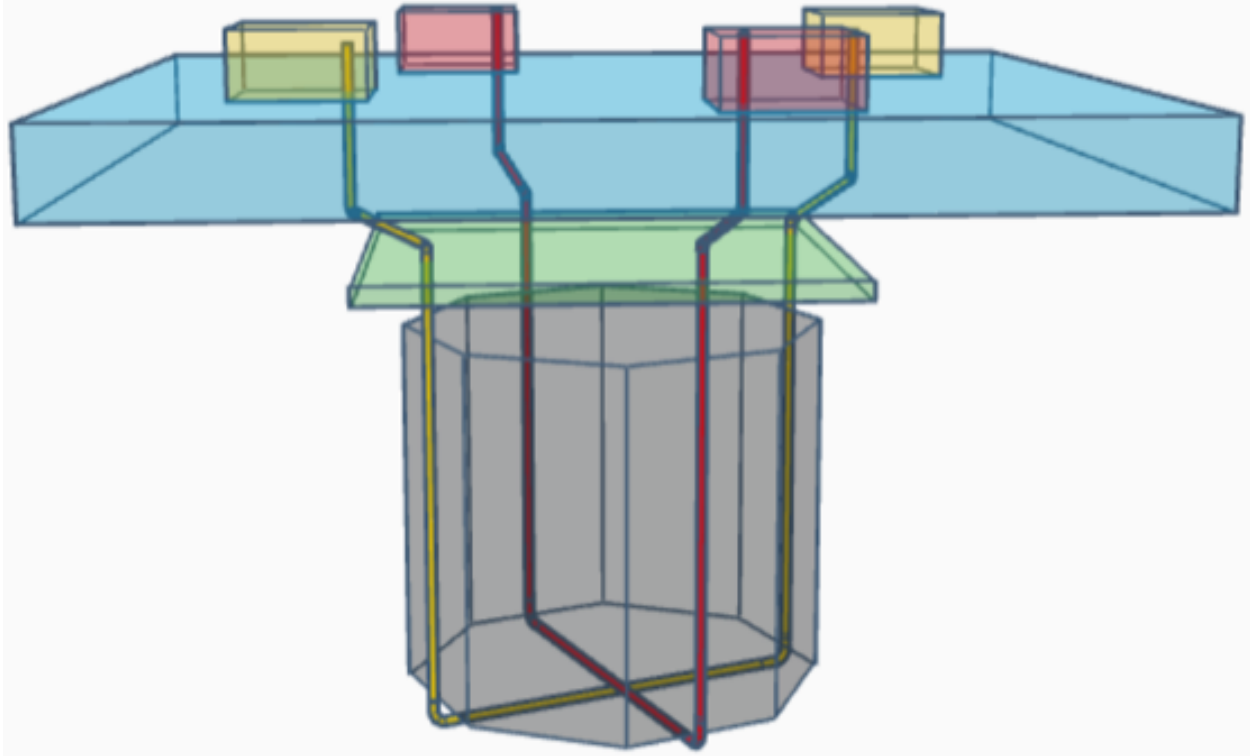


FIG. 18. Schematic representation of the system of guide tubes for insertion of sources.

While the  $^{241}\text{Am}^{13}\text{C}$  source represents the best choice for calibration of the neutron detection efficiency, interactions in the source holder and materials between the source and the TPC produced significant electron recoil background in the DS-50 TPC, problematic for characterization of the nuclear recoils of argon nuclei. The  $^{241}\text{AmBe}$  source was shown to be more suitable for this calibration. The 4.4 MeV  $\gamma$ -ray is promptly emitted in the  $^9\text{Be}(\alpha, n)^{12}\text{C}$  nuclear reaction in about 56 % of cases. By tagging the 4.4 MeV  $\gamma$ -ray in the Veto in a very tightly constrained time interval prior to the signal in the TPC, a very pure sample of nuclear recoils is obtained. The  $^{241}\text{AmBe}$  calibration in DS-50 provided the best available nuclear recoil calibration of the DS-50 TPC *in situ*, and was in excellent agreement with the nuclear recoil calibration from the stand-alone SCENE experiment [17].

The main novelty planned for the  $^{241}\text{AmBe}$  calibration is a custom production of a miniature (a few mm)  $^{241}\text{AmBe}$  source, since the typically available commercial sources cannot fit within the planned narrow guide tube system. The miniature  $^{241}\text{AmBe}$  source will rely on the procedure developed by the neutrino group at the University of Alabama [29]. The group successfully fabricated an  $^{241}\text{AmBe}$  source with an outer capsule dimension of just 2 mm in diameter and 7 mm long, with an activity of 50 neutrons per second using 1.9 MBq of  $^{241}\text{Am}$ . Fig. 19 shows the outer and inner source capsules. The inner capsule is made of tungsten to efficiently suppress the 4 MeV gamma emission from the  $^{241}\text{Am}$ . A very pure Be powder is mixed with  $^{241}\text{Am}$  high purity powder in an alcohol solution in a miniature test tube with a special micropipette and then transferred into the tungsten capsule. After the alcohol evaporates, the procedure is repeated. In the end, the mixture of  $^{241}\text{AmBe}$  is compressed with a wire for higher source activity. The wire is also used to seal the tungsten capsule. The tungsten capsule is placed inside the stainless steel capsule and welded shut. The source is then ready for certification and use. The outside capsule has a threaded part to attach the source to the rest of the calibration system.

Photoneutron sources such as YBe emit nearly monoenergetic 157 keV neutrons, suitable for the low energy end of the nuclear recoil band. However, such source requires 15 cm thick tungsten shield to block copious  $\gamma$ -rays present in the source. Thus, this source is very bulky and requires

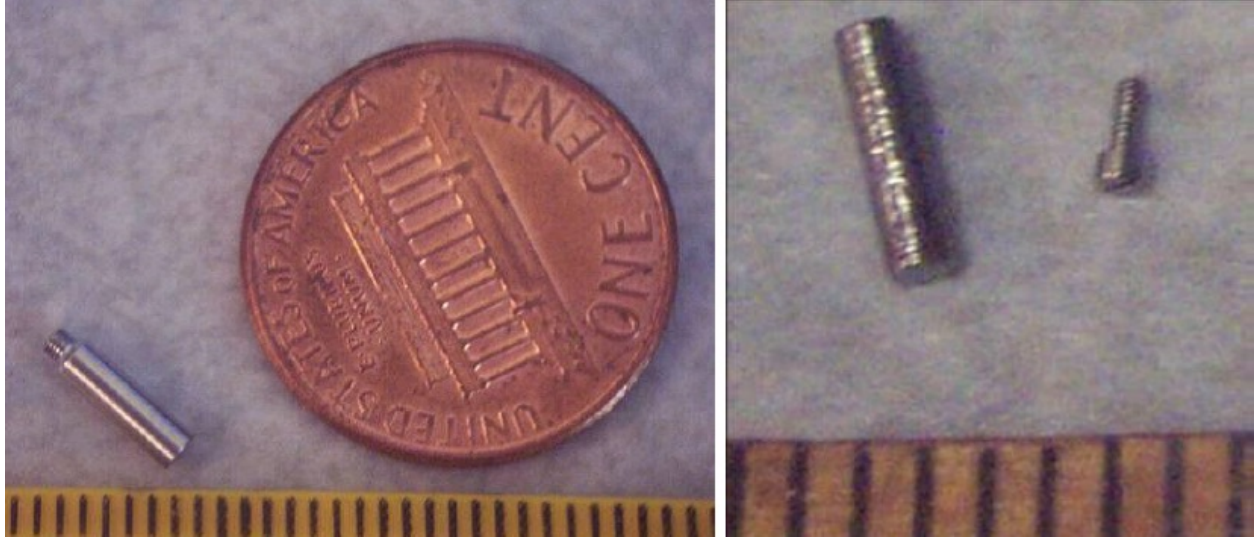


FIG. 19. **Left:** the outer capsule of the custom made  $^{241}\text{AmBe}$  source from the Alabama group [29]. **Right:** the inner tungsten capsule of said  $^{241}\text{AmBe}$  source.

a separate deployment system. Deployments will be monitored via a camera system to avoid any undesirable contact while operating in a delicate Veto.

#### 5.4. Guide Tube System

Implementation of calibration sources is being finalized, following the completion of the designs of the TPC the Veto, and the AAr cryostat. In parallel, plans are being developed for the calibration needs of the DS-20k prototype detectors for x-y positioning, light yield and nuclear recoil calibration. While work is still in progress, the overall schematic of how to guide radioactive sources from the roof of the AAr cryostat, down around and inside of the Veto detector, and then back up to the cryostat roof, is shown in Figure 18. The guide tube systems have been designed for simple, safe and efficient calibration of the Veto and TPC using miniature radioactive sources. They will allow deployment of the sources inside the Veto without direct contact with the argon, eliminating risks associated with it.

The guide tube system will bring radioactive sources from the top of the AAr cryostat, to locations along the TPC exterior. The sources will be delivered through an enclosed stainless steel tube coming vertically down from the top of the cryostat, passing by the TPC PMMA vessel and around its bottom. The guide tubes will be 3 cm (1.18") in diameter to minimize shadowing, dead space and radioactive background coming from the stainless steel. The stainless steel tube segments will be connected with Swagelok connectors. In addition, relatively small tube diameter will help for tighter control of the source location, especially important in the case of the gamma sources.

The miniature sources will be attached to the stainless steel guide wire that will be pushed with a wire driver powered by a stepper motor. A sleeve, made out of the PTFE tubing, will envelope the guide wire and the source to significantly reduce friction while the source and its guide wire are being pushed around. The wire driver will be equipped with a set of encoders and two sensor boxes for accurate positioning of the source. A pair of ring type inductive proximity sensors placed inside the sensor box will be used to reset the encoders when sources pass through a sensor at exactly known locations. The system will be purged with a low pressure nitrogen to eliminate any residual radioactivity that may have entered into the tubes.

Except for the sensor box, all other parts of the guide tube system that require power, control and nitrogen flow will be at the top of the AAr cryostat. An elaborate testing program must be performed to ensure high quality and safety of the calibration when using the guide tube system.

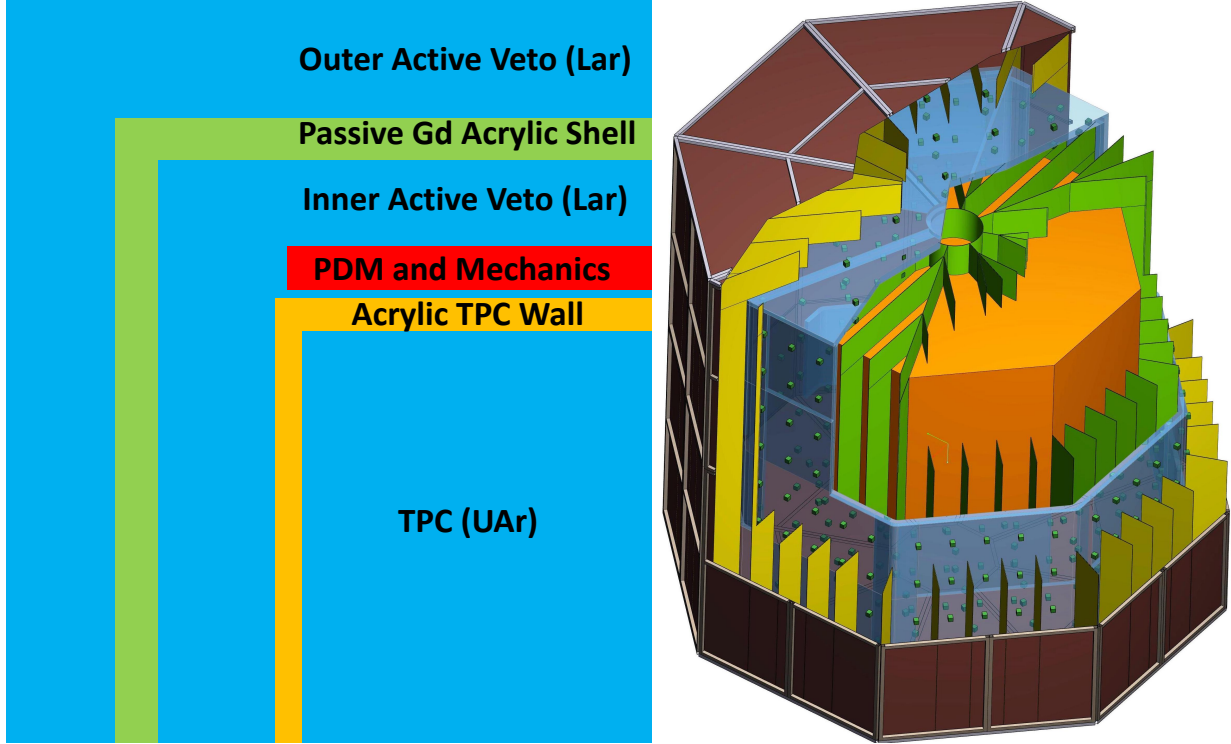


FIG. 20. **Left:** schematic conceptual view of the veto detector. **Right:** 3D cut-away view of the DS-20k veto detector.

All parts will be radio-assayed and the entire system will be tested off-site for robustness, precision and reliability. Dedicated survey is planned to record the exact guide tube path around the TPC PMMA vessel.

## 6. VETO DETECTOR

### 6.1. Overall Design

Benefiting from the implementation of a ProtoDUNE-like AAr cryostat, the Veto detector will utilize AAr as the scintillation material. The Veto detector is composed of three separate volumes; a passive octagonal acrylic shell loaded with gadolinium called the GdA and mounted around the TPC and providing  $4 - \pi$  coverage, a 40 cm thick inner volume of active liquid AAr called the Inner Argon Buffer (IAB) and sandwiched between the TPC vessel and the GdA, a 40 cm thick outer active volume of AAr called the Outer Argon Buffer (OAB) contained between the GdA and the outer copper Faraday Cage. The Faraday Cage will contain the Veto and TPC and optically and electrically isolate them from the remaining outermost AAr volume contained within the cryostat. A schematic drawing of the Veto concept is shown in the left side of Figure 20, as well as a 3D cut-away drawing which presents the preliminary design.

The required thickness of both the IAB and OAB of about 40 cm has been determined by MC simulation. The required thickness of the GdAS determined by the same simulation, is about 10 cm with a required Gd loading of 1 to 2 % by weight. The GdAS moderates neutrons emitted from all of the detector materials, particularly from the ones which make-up and surround the LAr TPC, while also enhancing the neutron capture probability with the inclusion of the Gd. The capture of the neutron on a Gd nucleus results in the emission of multiple  $\gamma$ -rays. These  $\gamma$ -rays interact in the IAB and OAB, their detection efficiency setting the required GdAS thickness and Gd loading fraction, as well as the minimum required IAB and OAB thickness.  $\gamma$ -rays are detected by use of

scintillation light emitted by the liquefied AAr in both the IAB and OAB.

Vertical segmentation of the IAB and OAB is foreseen to reduce the pile-up rate of  $^{39}\text{Ar}$  events from the AAr. The concept of this is shown in the cut-away view of the detector in the right panel of Figure 20, while the exact details are still being optimized by use of the Monte Carlo simulation. SiPMs will be mounted on the sides of the GdAS such that they are facing both the IAB and OAB. The basic detector element is the same PDM used in the TPC, but with a different front-end board coupled to it that is optimized for the geometry of the Veto detector. Tests are in progress to investigate the possibility of using an integrated electronics readout design for the Veto detector.

All of the inner surfaces of the Veto, including the external walls of the TPC and the walls of the vertical sectors, will be covered with reflector foils coated with wavelenght shifter (TPB), so that the VUV argon scintillation light is shifted to longer wavelengths where the LAr is very transparent. This light is then trapped within a segment of the Veto detector by multiple reflections until it reaches a SiPM. The optimal number of segments is being studied with the Monte Carlo simulation. We expect no more than 5 segments for each edge of the octagon. The segments are not liquid tight to allow flow of the argon through them, with a dedicated fluid-dynamics simulation planned to be performed to ensure that the LAr can be properly re-circulated throughout the proposed geometry.

The overall Veto detector design and the Monte Carlo simulation results will be validated using smaller prototype setups. Due to the nested nature of the detector system, strategic planning for the detector integration is also a big part of the development planning.

This conceptual design promises to achieve the most important criteria for the DS-20k detector, which is the efficient detection of neutrons such that no instrumental background interferes with the potential nuclear recoil signal from a WIMP scattering off of an argon nucleus. The design concept is scalable and lends well to serve as the basis for the future 400 t scale detector designed to collect an exposure of 1000 t yr in absence of instrumental background. The Veto design is based on elements which require no R&D and therefore can be built out of materials already available, with the only exception being the gadolinium loaded acrylic. We have established good contacts and an agreement with a company available to test in its laboratory techniques to mix gadolinium compounds with liquid MMA before starting the polymerization process. Taking into account that we do not need the final Gd-doped acrylic to be transparent to light (it acts only as passive neutron moderator), and that the homogeneity of the mixture is also not a critical parameter, several known difficulties related to metal loading into plastic scintillators are not an issue. After the success of the small scale laboratory test done in 2018, the company who will likely provide the high-quality acrylic for the JUNO experiment has agreed to produce samples of gadolinium loaded acrylic using their industrial production line. Radio-purity tests will be performed on these samples once they are available.

## 6.2. Assembly

The assembly sequence starts with the mounting of the bottom part of the GdAS along with its PDMs. This component will rest on a stainless steel support structure (Veto support structure) that is itself supported by the cryostat floor via temporary feet. The TPC is then lowered into its place above the bottom of the Veto detector. Once in place, the TPC is mechanically connected to the support structure of the Veto through mounting pillars. This choice has been driven by the aim of reducing the mass of the support structure of the TPC and avoiding relative movements between the TPC and the VETO during construction, commissioning and detector operation.

Once the TPC is fixed to the Veto support structure, the lateral panels of the GdAS and their PDMs are mounted. The vertical thin panels that divide the IAB into segments are then installed. The top GdAS panels are assembled next. Once the construction of the IAB is completed, PDMs are installed on the external surfaces of the GdAS and the panels which divide the OAB into segments are integrated. Then the copper frames that are used as the main structure of the Faraday cage are installed in the outermost part of the Veto. Finally the Veto detector is hanged from the cryostat roof using a dedicated support structure and several Kevlar ropes. One the Veto detector

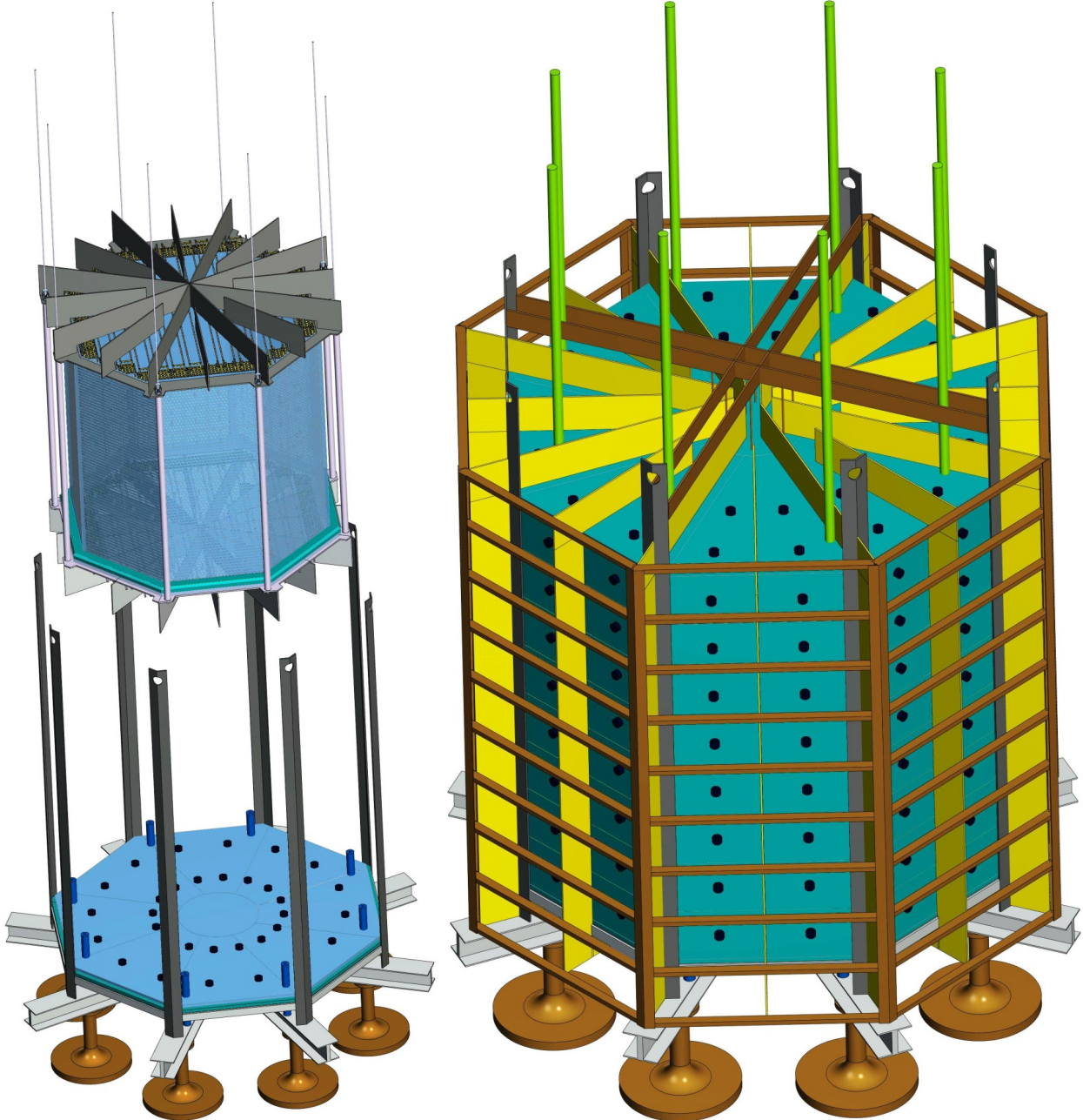


FIG. 21. **Right** Conceptual view of the placement of the TPC within the Veto support structure. **Left** 3D drawing of the DS-20k Veto detector, along with the temporary bottom support structure used for assembly and the Faraday cage.

construction is completed, the temporary pillars used to support the Veto on the cryostat floor during the construction are removed.

### 6.3. Background Rejection

The combination of the signals occurring inside the IAB and OAB, within a given time window, is used to tag and reject neutron captures. If a neutron produces a signal in the TPC, it will mimic that of a WIMP signal, meaning that it produces a single energy deposit with energy in the range

Material	Mass [tonne]	$^{238}\text{U}$ [mBq/kg]	$^{226}\text{Ra}$ [mBq/kg]	$^{232}\text{Th}$ [mBq/kg]	Neutrons $[10\text{ yr}]^{-1}$	+TPC $[200\text{ t yr}]^{-1}$	+TPC+veto $[200\text{ t yr}]^{-1}$
TPC Vessel	2.7	$1.2 \times 10^{-2}$	10	$4.1 \times 10^{-3}$	$1.1 \times 10^3$	0.17	$1.7 \times 10^{-2}$
TPC SiPMs	0.12	-	-	-	$1.1 \times 10^4$	0.16	$1.6 \times 10^{-2}$
TPC Electronics	1.0	-	-	-	$2.5 \times 10^4$	0.36	$3.6 \times 10^{-2}$
TPC Mechanics	1.1	3.9	3.9	1.9	$1.8 \times 10^3$	$1.8 \times 10^{-2}$	$2.0 \times 10^{-3}$
Veto SiPMs+elec.	0.40	-	-	-	$1.3 \times 10^4$	0.10	$1.0 \times 10^{-2}$
Veto Acrylic	13	$1.2 \times 10^{-2}$	10	$4.1 \times 10^{-3}$	$5.2 \times 10^3$	$4.2 \times 10^{-2}$	$4.0 \times 10^{-3}$
Veto Reflectors	1.0	$1.2 \times 10^{-2}$	1.0	$4.1 \times 10^{-3}$	$4.0 \times 10^2$	$2.4 \times 10^{-2}$	$2.0 \times 10^{-3}$
Veto Steel	1.1	3.9	3.9	1.9	$1.8 \times 10^3$	$1.4 \times 10^{-2}$	$1.0 \times 10^{-3}$
$\text{Gd}_2(\text{SO}_4)_3$ $\alpha$ 's on self	0.26	7.0	7.0	0.2	$2.1 \times 10^2$	$2.0 \times 10^{-3}$	$<1.0 \times 10^{-3}$
$\text{Gd}_2(\text{SO}_4)_3$ $\alpha$ 's on PMMA	0.26	7.0	7.0	0.2	$7.2 \times 10^2$	$6.0 \times 10^{-3}$	$1.0 \times 10^{-3}$
Copper Cage	1.0	0.30	0.30	$2.0 \times 10^{-2}$	$1.2 \times 10^1$	$<1.0 \times 10^{-3}$	$<1.0 \times 10^{-3}$
Cryostat Steel	250	50	$1.0 \times 10^3$	3.9	$1.0 \times 10^6$	-	$<1.0 \times 10^{-3}$
Cryostat Insulation	40	$3 \times 10^3$	$8.0 \times 10^3$	$3.0 \times 10^3$	$8.0 \times 10^7$	-	$<1.0 \times 10^{-3}$
<b>Total</b>						<b>0.9</b>	<b>0.09</b>

TABLE V. Radiogenic neutrons sourced by the LAr TPC construction materials, veto and cryostat materials, with details of expected contamination levels, background after TPC cuts, and residual background after combined TPC and veto cuts, all relative to the full 10 yr run time and the full fiducial 200 t yr exposure. The number of expected neutrons is calculated from the expected contamination levels and material composition. Note that no specific activity is reported for the TPC SiPMs and associated electronics: in this case the predicted neutron yield is the results of an extremely detailed calculation, accounting for the cumulative contribution of several tens of components, individually assayed. The same consideration holds for the veto SiPMs and electronics, which contribution is reported in combination. For neutrons due to  $(\alpha, n)$  reactions resulting from  $\alpha$ 's originating from impurities in  $\text{Gd}_2(\text{SO}_4)_3$ , the contribution is broken down between those due to reactions on Gd sulfate itself and those due to reactions in the PMMA matrix containing the Gd sulfate; the mass fraction of Gd in the GdAS 1 %, for the anticipated 2 % concentration by mass of  $\text{Gd}_2(\text{SO}_4)_3$ . (For ease of conversion: 1 ppt( $^{238}\text{U}$ )  $\simeq 1.2 \times 10^{-2}$  mBq/kg; 1 ppt( $^{232}\text{Th}$ )  $\simeq 4.1 \times 10^{-3}$  mBq/kg.)

30 keV<sub>nr</sub> to 200 keV<sub>nr</sub>. This also includes fiducial volume cuts which exclude events occurring at a distance from the TPC walls less than 30 cm in the radial direction and less than 70 cm from the top and bottom. For events that pass this fiducialization, the Veto is then searched within a time window of 800  $\mu\text{s}$  around the TPC trigger time. To minimize dead time losses due to  $\beta$ -decay from  $^{39}\text{Ar}$  in the veto filled with AAr, a 800 keV threshold is set for each of the two parts of the Veto detector, while a lower 100 keV threshold is set for events with coincidence signals in both parts of the Veto detector.

The design of the Veto and the choice of all the materials used to build the entire detector are set by the requirement of having less than <0.1 events untagged neutrons during the total exposure of 200 t yr. The radioactive contamination of the materials used to build the Veto is therefore also considered and limits are set by requiring that the corresponding neutron background induced in the TPC, after the implementation of all analysis cuts, is well below the above mentioned threshold of <0.1 events in 200 t yr.

DS-20k is designed to operate with zero backgrounds, meaning that all sources of instrumental background are reduced to <0.1 events over a 200 t yr exposure. All background from minimum-ionizing radiation sources will be completely removed thanks to the combined action of PSD of the primary scintillation pulse and comparison of the primary and secondary scintillation (see the “Project Narrative” for details on the suppression of background from  $pp$  scatters on electrons and Ref. [30] for that from  $^{222}\text{Rn}$ ,  $^{220}\text{Rn}$ , and progenies).

We focus here on the leading source of background, that is neutrons from the LAr TPC construction materials. We simulated the response of the LAr TPC, IAB, and OAB to  $(\alpha, n)$ , which is expected to be the dominant contribution to the instrumental background budget. The geometry of the LAr TPC is that described in the rest of the document. The LAr TPC vessel is made of 5 cm-thick PMMA, which helps to mitigate backgrounds by moderating the neutrons coming from the detector’s construction materials. For the PMMA, we assume the purity achieved in Ref. [31], while for the Gd-loaded acrylic, we assume the purity of the scintillator of Ref. [32].

The results of the Monte Carlo simulation are summarized in Table V, where it is seen that the final results meet the goal of <0.1 events in the full 200 t yr exposure. The two main sources of contamination are the electronics of the SiPMs and the insulation of the cryostat. The collaboration is now working to further improve the materials selection, which could reduce the expected neutron flux coming from those components.

The only remaining background for WIMP searches will be the signal from the coherent scattering of atmospheric neutrinos on argon nuclei, with an expected 3.2 events over the 200 t yr exposure. DS-20k will thus be the first experiment in a position to detect this important signal.

Surface contamination due to plate-out of radon on the surfaces is an additional source of background that can not be neglected. Radon is present in the outdoor air with a concentration of few to 10 Bq/m<sup>3</sup>, while inside buildings and in underground laboratories the concentration is typically higher (up to 120-150 Bq/m<sup>3</sup>). <sup>210</sup>Pb atoms accumulate on every surface of materials exposed to air and decay to <sup>210</sup>Bi that produces <sup>210</sup>Po. This is the potentially dangerous isotope because the  $\alpha$  originating in its decay could produce neutrons. We estimate the concentration of <sup>210</sup>Pb adsorbed on an acrylic surface using data measured for polyethylene exposed to the SNOLAB air. We roughly expect a few tens of neutrons (before the analysis cuts) per day during the time which the entire surface of the acrylic is exposed to atmospheric air. This sets specific requirements for the cleanliness of the acrylic surfaces and on the mounting procedures of the Veto, which must be done in a radon free environment.

## 7. DATA ACQUISITION

The current design for the DS-20k electronics and its data acquisition system (DAQ) accommodates both the large number of sensors and the long drift-time (expected maximum electron drift time is 4 ms) of the LAr TPC, as well as the readout of the Veto detector. The trigger rate during normal dark matter search data taking has three major contributions: background events from detector materials, background events from <sup>39</sup>Ar, and random triggers. In order to estimate the first term, the event rate measured in the UAr exposures of DS-50 is taken, excluding the contribution from the PMTs and from the remaining <sup>39</sup>Ar in DS-50. This is scaled by the ratio of surface areas of DS-20k and DS-50, a factor of 55, obtaining an expected rate of 27 Hz. It is noted that these events will be concentrated at the surfaces of the active volume.

By using UAr and making the assumption of an <sup>39</sup>Ar reduction factor of 1400 with respect to AAr, there will still be an additional rate of about 16 Hz generated by <sup>39</sup>Ar decays, uniformly distributed throughout the active volume. In summary, events with correlated S1 and S2 signals are expected in DS-20k at a rate of about 50 Hz. On the other hand, the average singles rate per channel is dominated by the dark count rate (DCR) of the SiPMs. With the required 0.08 Hz/mm<sup>2</sup> specification, this will imply a singles rate per PDM of about 200 Hz. The event rate in the Veto detector, instead, will be dominated by <sup>39</sup>Ar decays in the instrumented AAr buffers.

### 7.1. General DAQ scheme

The baseline scheme for the TPC and Veto detector DAQ electronics hardware foresees an optical signal receiver feeding a differential signal to a flash ADC digitizer board that is connected to a large Field Programmable Gate Array (FPGA). The digital filtering capability within the digitizer board would allow the discrimination of single photoelectron signals and the determination of the time and charge of the individual channel pulses. For large and slow signals, such as the S2 ionization-born pulses in the TPC, the digitizer board would provide a downsampled waveform matching the expected signal bandwidth of a few MHz.

The combination of the data processing will provide the needed data reduction to allow triggerless operation of the readout for the TPC. Data from the Veto and TPC detectors will be transferred to the front-end data processing units where further data reduction will be performed. Finally the

data will be passed to an online event building processor that will select interesting events and write them to permanent storage.

In normal data taking mode, an event could be identified by a coincidence of hits in the TPC within a specified time window. A coincidence of 7 hits in 200 ns would result in a random trigger rate well below 0.1 Hz. Nuclear recoil events at the trigger threshold, producing about 15 PE in 5  $\mu$ s, would result in the collection of 6 PE to 8 PE within the first 200 ns. Thus, the trigger would be 100 % efficient for the WIMP-like signals of interest.

The event building and software trigger stage is realized with modern commodity CPUs and connected through fast ethernet with the front-end DAQ processors. Given the low expected rate, the trigger-less option is foreseen to be feasible to implement. The expected combined event size for the TPC and Veto detectors is projected to be well below 1 MB.

Synchronization between the TPC and Veto DAQ is fundamental for the effectiveness of the design, and will be provided and maintained during the data taking. The clock source of the TPC DAQ will be used as reference and digital signals (like GPS time stamps or trigger IDs) will be generated to uniquely identify each event regardless of the trigger origin or the detector. A pulsed signal distributed to all the modules will be used to check and correct the alignment of each channel among the TPC and Veto detectors.

The DAQ system will be located in an electronics room which will be placed on the roof of the AAr cryostat. The environment will allow personnel access while minimizing the length of the optical fibers used to transmit the data from the TPC to the signal receivers.

## 7.2. Digitizers

The basic readout element of the proposed DS-20k DAQ system is a multi-channel board hosting several fast ADCs linked to a large FPGA for digital signal processing. This will be connected to a host CPU for control, monitoring and data formatting using as an output channel through a 1 Gbit/s to 10 Gbit/s ethernet connection to an external computer. The ADC will have 14 bits resolution and 125 MHz sampling speed. The board will accommodate one octal fADC chip for each of the 8 mezzanine boards, allowing it to handle 64 channels in total with a single board with a VME64 6U form factor. Data from the ADCs will be sent using high bandwidth JESD interface directly to a large FPGA. The board will host a Xilinx made Zync Ultrascale+ with a quad-core ARM Cortex A53 processor. Recent progress on this development includes the full implementation of the JESD interface and the ability to output data at the maximum specified speed. Specialized firmware is to be provided by the collaboration for noise filtering, basic data formatting and zero suppression to be implemented in the FPGA.

The development of this electronics board is an ongoing partnership between the CAEN Company from Viareggio, Italy, which was selected as the provider of the electronics by the INFN, and the collaboration. The basic layout of the boards and the components that will comprise them have been selected and the first prototype will be available for testing in the summer of 2019. In the meantime, work in close cooperation between the GADMC and the CAEN firmware experts is ongoing to implement the needed signal filtering algorithms. In parallel, a DAQ system for the initial prototype TPC tests has been deployed at CERN in order to acquire data from up to two PDM Motherboards, amounting to 50 PDM channels.

## 7.3. DAQ software

The Maximum Integrated Data Acquisition System (MIDAS) has been chosen as a framework for developing the DAQ readout and related online control software for the DS-20k detector. The MIDAS DAQ package has been used extensively within the DEAP-3600 experiment, and together with the CAEN hardware provides a nice baseline for the digitization and recording of the raw data. A collaboration between the MIDAS and CAEN developers has been established to ensure that the

interfacing of the front-end hardware is compatible with the back-end hardware and software that will ultimately compile and write the data to permanent storage.

MIDAS is also well suited for handling the DAQ of the DS-Proto, for which, at least in the first stage, has a readout strategy and hardware implementation similar to those used in the DEAP-3600 experiment. The DEAP-3600 hardware is mainly composed of 32xVME-V1720 and 4xVME-V1740 using the proprietary CAEN CONET2 optical link to 5 different computers, providing optimum individual link data throughput using the A3818C PCIe interface. The DS-Proto readout will be, in the first phase, based on 5 CAEN VME-V1725 and a custom trigger module developed by the TRIUMF group. This system has been already installed at CERN in the first part of 2019 in order to provide the DAQ system for the first 50 channels (2 motherboards) of DS-Proto. In a later stage, the readout for DS-Proto will be based on the new digitizer boards from CAEN, previously described. Work has started toward designing an evolution of the MIDAS software to accommodate the new hardware boards and provide the needed event building and software trigger capability.

## 8. COMPUTING

The data storage and offline processing system must support transfer, storage, and analysis of the data recorded by the DAQ system, for the entire lifespan of the experiment. It must provide for production and distribution of simulated data, access to conditions and calibration information and other non-event data, and provide resources for the physics analysis activities of the collaboration. Necessary components for data storage and offline systems are the software framework and services, as well as the data management system, user-support services, and the world-wide data access and analysis job-submission system. The design of the system is built upon the knowledge acquired in the construction and operations of the DS-50 detector.

The large number of channels in the LAr TPC makes it impractical to digitize and save the full waveform of each channel, as done in DS-50. Nevertheless, the charge and hit time information that will be saved will preserve all the necessary details about the amplitude and time evolution of the signals generated in the target. With appropriate filtering and compression, in addition to the expected background reduction described elsewhere in this document, the amount of data selected for recording in DS-20k is expected to be only a few times that of DS-50. The DS-50 experiment typically collects about  $9 \times 10^5$  events/d, of which  $8 \times 10^5$  events/d come from laser calibrations, with the remaining  $1 \times 10^5$  events/d from the dark matter search. The size of a DS-50 laser calibration event is about 0.1 MB, while the size of a dark matter search data event is about 2.6 MB. This is expected to decrease by a factor of 3 to 4 in DS-20k, despite the much larger number of channels. Taking into account the event size and data rate, the improved background rejection and data filtering, and using the experience from DS-50, the short-term storage required at the experimental site is expected to be 20 TB. The total storage inventory required for the experiment is expected to be more than 20 PB, including the storage needed for simulated and reconstructed events.

### 8.1. Computing systems and data workflow

The primary event processing will occur at the experimental site in the software trigger farm. Pre-processed data is archived on the temporary storage at the experimental site and copied to central computing centers (Tier-1/Tier-2). These facilities archive the pre-processed data, provide the reprocessing capacity, provide access to the various processed versions, and allow analysis of the processed data. Derived datasets produced in the physics analyses are also copied to the Tier-1/Tier-2 facilities for further analysis and long-term storage. The Tier-1/Tier-2 facilities also provide the simulation capacity for the DS-20k experiment.

Bulk data processing is expected to be performed using low cost commodity cluster computing based on commercial CPUs. Final data analysis will be performed either directly at the Tier-1/Tier-

2 centers or on commercial CPUs hosted at institutes participating in the experiment. There is also the option of using the considerable free resources available on the Open Source Grid, which many experiments are currently using to run their reconstruction and analysis jobs.

The amount of short term storage currently available at LNGS for DS-50 consist of 7 TB of front-end storage used as temporary buffer and located in the underground laboratory, plus 710 TB of disk space in the above ground computing center for short- and long-term storage of DS-50 data. From there, raw data are copied to CNAF and Fermilab for reprocessing and analysis. CNAF is making available 1 PB of disk storage and 300 TB of tape storage. At Fermilab, there is 50 TB of fault-tolerant disk storage and about 620 TB on the dCache-based tape system for long-term storage. It is expected that much of this inventory will be recycled for the DS-20k experiment, aside from what is necessary for ongoing storage of DS-50 raw data. Any necessary additional tape storage will be purchased and installed. The total amount of storage for the ten years of data-taking, including calibration and simulated data, is 20 PB of disk storage and 20 PB of tape storage. The processing power currently used for reprocessing and analysis of DarkSide-50 data includes a farm of 400 cores at LNGS for production and validation, plus 400 job queues at CNAF and 25 guaranteed batch slots (soon to increase to 60 guaranteed batch slots) on the Fermilab grid system.

Currently, a single DS-50 event takes about a half of a second to reconstruct on a typical 2.8 GHz processor, meaning that 100 dedicated cores can maintain reconstruction in realtime for an event rate up to 200 Hz. Assuming a factor two increase in the cpu time needed to reconstruct an event, a factor ten to simulate a full event, a real data plus calibration event rate of 100 Hz, and a sample of simulated events of the same dimension of the real-data one, DS-20k needs 100 dedicated cores to maintain reconstruction in realtime of the collected real data + calibration events, and 1000 dedicated cores to produce the simulated samples. Moreover, 2000 physical cores are sufficient to reprocess all physics events collected in one year in a three month time period.

## 8.2. Software Environment

DS-20k will adopt an object-oriented approach to software, based primarily on the C++ programming language, with some components implemented using other high level languages (Python etc.). A software framework has been built up during the DS-50 experiment which provides flexibility in meeting the basic processing needs of the experiment, as well as in responding to changing requirements. In order to support code reuse, build a system optimized for both the offline and software trigger environment, and provide common user access to low-level algorithms used for I/O and data persistency, the C++ code will make heavy use of object oriented abstract interfaces techniques.

The reconstruction combines information from the TPC and the veto detectors. A typical reconstruction algorithm takes one or more collections of information from the event data model (EDM) raw data stream as input, calls a set of modular tools, and outputs one or more collections of reconstructed objects. Common tools are shared between reconstruction algorithms, exploiting abstract interfaces to reduce dependencies. Analysis of calibration data will also be performed within the reconstruction and simulation software environment.

DS-20k will produce roughly 2 PB of data annually, combining the data processing, simulation, calibration, and distributed analysis activities. A data storage and management infrastructure is necessary to allow efficient storage and access to all this data. Two types of data storage are foreseen. The first is a file-based data and the second is relational-database-resident data. File storage is used for bulky items such as event data (physics data, calibration data and simulation data). Database storage is used for other types of information, including technical data like detector production, installation, survey and geometry data, online/TDAQ databases, conditions databases (online and offline), offline processing configuration and bookkeeping information, and to support distributed data and database management services. File-based storage of C++ objects will be implemented through the use of ROOT I/O, which provides high performance and highly scalable

object serialization to random-access files. Database storage will be based on SQL-based relational databases (MySQL and SQLite). All these technologies are widely used and well tested in HEP experiments.

Computing resources will be accessed through Grid middleware components and services. These provide services for software installation and publication, production operations, and data access for analysis through a uniform security and authorization infrastructure, as well as interfaces for remote job submission and data retrieval, and job scheduling tools designed to optimize utilization of computing resources. The Grid infrastructure will be based on the infrastructure and the software tools and services developed for the LHC Computing Grid (LCG) project.

The High-Level Software Trigger (HLST) provides the online event selection. The trigger is based on an online version of the DS-50 reconstruction software, which has been optimized and tailored for the DS-20k online environment running on farms of Linux PCs and/or GPUs farms. Overall, the HLST has to provide the required rate reduction and pre-processing of raw data, including the production of global event records in analysis EDM format. The HLST will use the offline computing environment, allowing DS-20k considerable commonality in the design and management of the selection software itself. This also allows the HLST to use various offline software components, like detector description, calibrations, EDM, and reconstruction algorithms. The same infrastructure can be used for data monitoring by simply replacing or augmenting the selection algorithms with those for monitoring.

### 8.3. Simulation

G4DS is a Geant4-based simulation toolkit specifically developed for DarkSide. The modular architecture of the code was developed in order to describe the energy and time responses of all the detectors belonging to the DarkSide program, namely DS-10, DS-50, and DS-20k, but other variations of the geometries as well. For each of them, G4DS provides a rich set of particle generators, detailed geometries, real data tuned physical processes, and the full optical propagation of the photons produced by scintillation in liquid argon and by electroluminescence in gaseous argon. The main goals of G4DS are to accurately describe the light response, calibrate the energy responses in S1 and S2 and the time response expressed by the  $f_{90}$  variable, tuning of the analysis cuts and their efficiency estimation, prediction of the electron and nuclear recoil backgrounds, and definition of the signal acceptance band.

G4DS tracks photons up to their conversion to photoelectrons, which occurs when a photon reaches the active region of a photosensor and survives according to the quantum efficiency. The conversion of the photoelectron into a charge signal is handled by the electronic simulation, an independent, custom-made C++ code. The electronic simulation embeds all the effects induced by the photosensors (e.g. after-pulse and cross talk) and by the electronics itself (e.g. saturation). The electronic simulation also has the option to overlap simulated events and real data baselines in order to provide more realistic simulations. As output, it produces waveforms for each channel with the same data format of the real data, in order to be processed by the same reconstruction code.

G4DS can also track events generated by FLUKA and TALYS simulation codes, previously developed within the collaboration. The FLUKA simulation is mostly used to study cosmogenic neutrons and isotope productions, while TALYS is used for ( $\alpha, n$ ) reactions, both providing input for the prediction of the nuclear recoil background.

## 9. THE ReD EXPERIMENT

The ReD project aims to characterize the light and charge response of the LAr TPC to neutron-induced nuclear recoils, especially at low energy, and to explore for the possible directional dependence suggested by the SCENE experiment [17, 18]. ReD encompasses the irradiation of a

miniaturized LAr TPC with a neutron beam at the INFN, Laboratori Nazionali del Sud (LNS), Catania. Neutrons are produced via the reaction p( $^7\text{Li}$ , $^7\text{Be}$ ) from a primary  $^7\text{Li}$  beam delivered by the TANDEM accelerator of LNS. A  $\Delta E/E$  telescope, made by two Si detectors, identifies the charged particles ( $^7\text{Be}$ ) which accompany the neutrons emitted towards the TPC. Neutrons scattered from the TPC are detected by using an array of nine 3" liquid scintillator (LSci) detectors, using EJ309 liquid scintillator coupled to ET 9821B PMTs. The Si telescope and the TPC are not at the same height: this is mandatory in order to tag neutron scatterings (n,n') from a non-horizontal interaction plane. All LSci are placed such to tag recoils having the same energy, i.e. the same scattering angle with respect to the incident neutron, but different angle with respect to the drift field of the LAr TPC, thus allowing to search for a possible directional response. Thanks to the support provided by INFN CSN2, the entire set-up has been procured, integrated, commissioned and deployed to the "80 deg" beamline of LNS. The first beam run test took place in June-July, 2018.

The core detector of ReD is a custom-made TPC designed by UCLA, which is a miniaturized version of the LAr TPC for DS-20k. The TPC is a cube with size of about 50 mm. An acrylic vessel defines the active volume, with the top and bottom acrylic windows ITO coated to allow for the application of the electric field, and the side ESR-acrylic sandwich reflection panels to maximize the reflectivity of the chamber. All of the internal surfaces are coated with TPB to wavelength shift the argon scintillation light. The drift field is kept uniform along the drift coordinate by means of the field shaping rings, deposited by thin-coating the walls of the acrylic vessel with ITO. The drift length, extraction length and electroluminescence length of the ReD TPC are 5 cm, 3 mm and 7 mm, respectively. The ReD TPC uses all the innovative features of the DS-20k design, in particular the optoelectronic readout based on SiPM developed by FBK and the cryogenic electronics. Two 5x5 cm<sup>2</sup> tiles are available from FBK, each made by 24 rectangular SiPMs. The tile on the top of the LAr TPC has a 24-channel readout, in order to improve the ( $x, y$ ) sensitivity, while the bottom tile has a standard 4-channel readout. A dedicated 24-channel Front End Board (FEB) has been designed and produced by INFN-Na in collaboration with INFN-Bo and LNGS.

The LAr TPC is contained in a new cryogenic system. The commissioning of the system was carried out in Naples. Starting from April 2018, the new TPC and cryogenic system were operated and tested. Measurements were taken with lasers, low-energy  $\gamma$  sources and neutrons from a DD generator. This allowed for the first characterization of the LAr TPC and for an integrated test of: operating procedures, photosensors, DAQ, slow control, data handling and reconstruction algorithms. The system was successfully operated in single and double phase modes, with a light yield of about 10 phe/keV at null field. The new LabVIEW-based slow control developed by INFN-Genova was also integrated and commissioned. The set-up was irradiated in Naples with the DD neutron gun from the Temple University, such to assess the PSD performance of the LAr TPC. The run also included one LSci, allowing for the first test of the DAQ for a system made by two different types of detectors. All nine LSci detectors had been previously tested and characterized at INFN-Roma1.

The commissioning and the characterization of the system in Naples opened the way for the deployment of the system at the beamline of LNS. The entire set-up (TPC with cryogenic system, liquid scintillators with their PMTs and the mechanical support structure) was shipped and reassembled in Catania in June 2018. Meanwhile, the beamline had been refurbished on the basis of the experimental design, optimized with dedicated Monte Carlo simulations, and the mechanical clearance requirements. The configuration was conceived to allow the tagging of nuclear recoils between 20 and 100 keV traveling in the parallel and orthogonal directions with respect to the TPC drift field, by varying the primary beam energy only. Furthermore, having a dedicated liquid scintillator at small scattering angles opens the possibility to study the response of the TPC to very low-energy nuclear recoils, O(1 keV). A new scattering chamber was installed with a new beam pipe. The  $\Delta E/E$  telescope was installed inside the vacuum scattering chamber, commissioned and consists of two Si detector (20  $\mu\text{m}$  and 200  $\mu\text{m}$  thickness, respectively) by ORTEC.

Initially, the cryostat and the liquid scintillators had to be mechanically aligned with respect to the target with a precision of the order of a few mm. The alignment was performed by following a

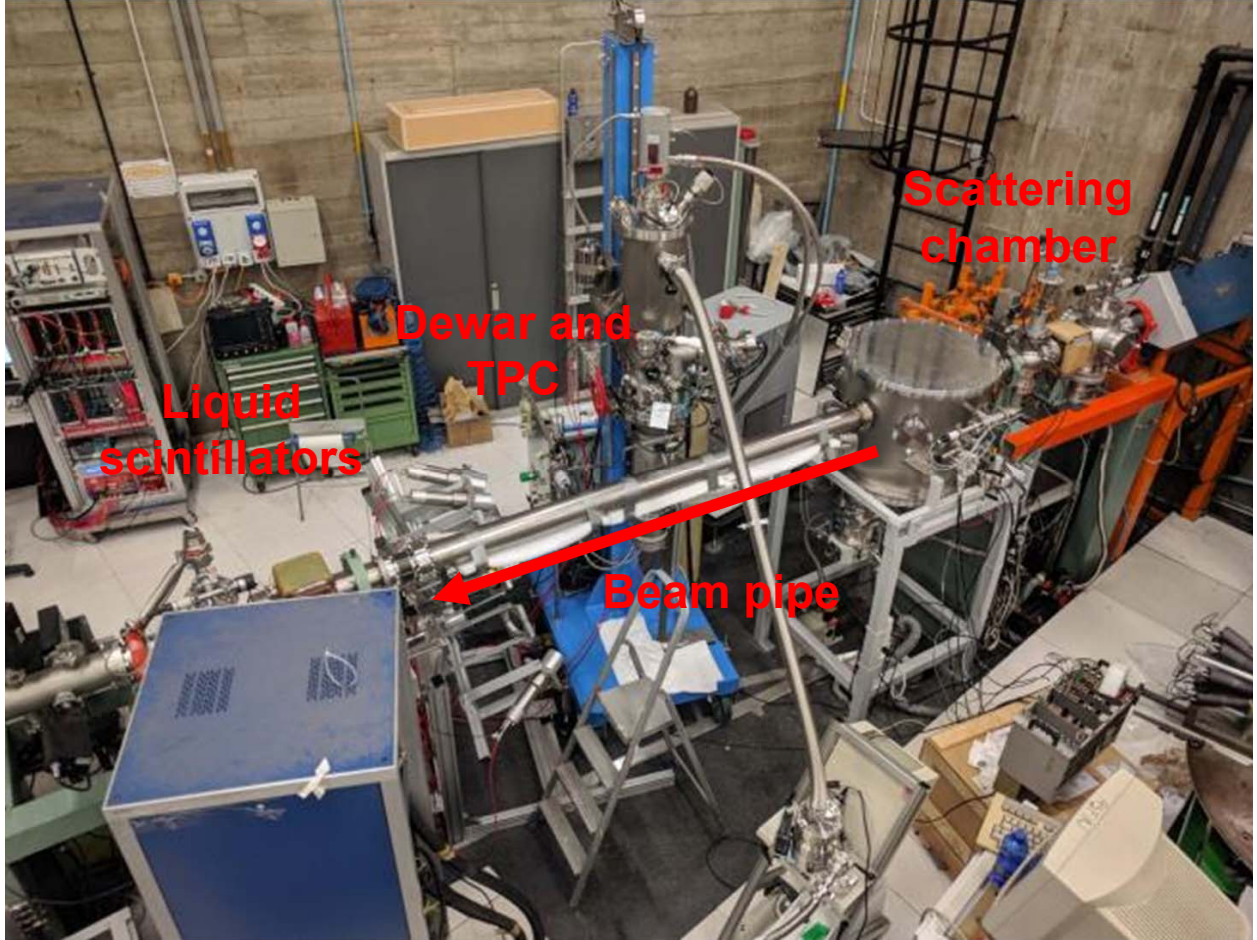


FIG. 22. Photo of the “80 deg” beamline at LNS, after the deployment and alignment of ReD. The targets and the Si telescope are hosted inside the vacuum scattering chamber.

detailed procedure worked out in advance. The ReD set up in Catania is displayed in Fig. 22.

After the scientific approval of the project by the Scientific Committee (PAC) of LNS, a test beam run was scheduled in June-July 2018, meant for technical tests and commissioning. The individual detectors were first commissioned and tested individually, by using the laser and radioactive sources. Light yield and timing were checked by using  $^{241}\text{Am}$  and  $^{22}\text{Na}$ , respectively. A  $^{252}\text{Cf}$  fission neutron source was used to characterize the pulse shape discrimination performance of both the LAr TPC and the LSci detectors. The light yield of the TPC was measured to be about 8.5 phe/keV, while the electron drift lifetime about  $250\ \mu\text{s}$ , i.e. much longer than the total drift time (about  $40\ \mu\text{s}$  at the operational field of  $0.2\ \text{V/cm}$ ), with no hints of degradation in time. The calibration of the LSci detectors indicated a 50 % trigger efficiency at  $20\ \text{keV}_{ee}$  and a time resolution of 1.2 ns (rms), which is sufficient for the measurement of the time-of-flight.

The integration of the three detector systems was done with the TANDEM beam. Neutrons were produced by sending a  $^7\text{Li}$  28 MeV beam onto a set of  $\text{CH}_2$  targets having thickness between 150 and  $250\ \mu\text{g/cm}^2$ . The intensity of the beam impinging on the target after the collimator, measured by the Faraday Cup installed at the far end of the beam pipe, ranged between 0.5 and 7 nA. The DAQ software handled 41 readout channels from three FADC boards (CAEN V1730), at 500 MHz sampling rate. A data-to-disk rate of 40 MB/s has been achieved. The Si telescope was placed at 5 deg with respect to the beam. The scattering kinematics allows for two solutions with  $^7\text{Be}$  in this direction, one having an associated 7.5 MeV neutron at 22.5 deg, the other with a 2 MeV neutron at 45 deg. The LAr TPC is at 22.5 deg from the target, i.e. it is hit by 7.5 MeV neutrons, produced in association with the  $^7\text{Be}$  detected by the Si telescope. The beam energy and the scattering angles

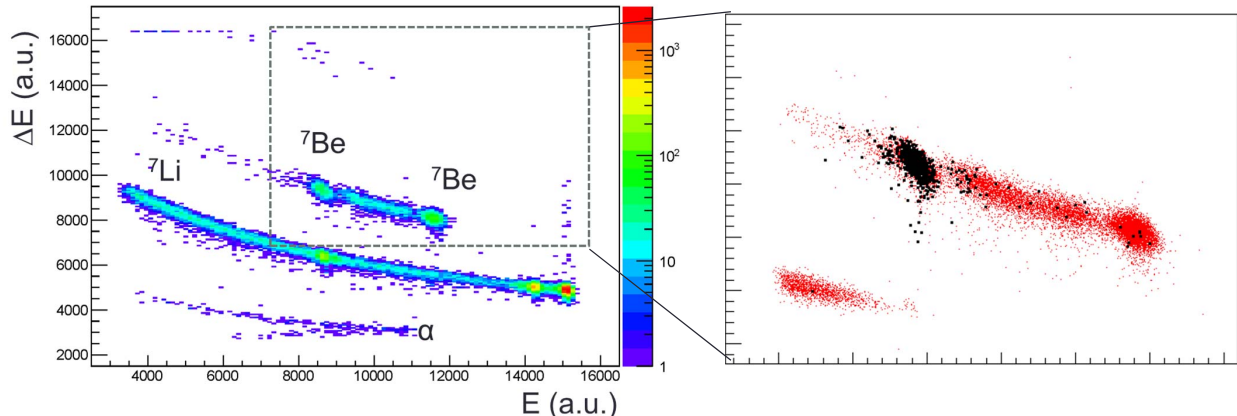


FIG. 23. **Left:** scatter plot of the amplitudes of the  $\Delta E$  and  $E$  Si detectors, placed at 5 deg with respect to the beam axis. **Right:** zoom of the previous scatter plot in the region of the  ${}^7\text{Be}$  loci; the black markers are events having a coincident signal in the TPC.

cause the experiment to select nuclear recoils in the TPC of approximately 70 keV.

About 24 hours of data have been taken in the best operating conditions. Data has been taken in both single and double phase modes and with two different trigger schemes, i.e. “Si and TPC”, “Si and any PMT”. The latter scheme yields a large fraction of accidentals, due to the large singles rate of the PMTs (kHz), but it gives potential access to low-energy recoil in the TPC, which would fail to trigger the TPC (low S1, or S2 only). Those events can later be searched for offline in the data analysis. Typical trigger rates were between 0.1 and 0.7 Hz. Events were observed with the proper signature, i.e. a  ${}^7\text{Be}$  nucleus detected by the telescope, a nuclear recoil in the LAr TPC and a neutron scattering in the liquid scintillators. Neutron-induced recoils events in the TPC and in the LSci detectors are clearly separated from  $\gamma$  signals, either physical or accidental, by means of pulse shape analysis. As expected, the time difference  $\Delta t$  between the pairs of detectors features a peak of physical coincidences, sitting on a plateau of accidentals. The scatter plot of the amplitudes of the  $\Delta E$  and  $E$  Si detectors is displayed in the left side of Figure 23. It shows the ability of the telescope to discriminate the charged products of the beam-target reactions, i.e. the main  ${}^7\text{Li}$  band due to elastic scattering and the two  ${}^7\text{Be}$  loci corresponding to the two solutions allowed by kinematics. The right side of Figure 23 shows the same distribution (zoomed), with the black markers referring to the events having a coincident signals in the TPC. As expected, coincident events between Si and TPC are mostly associated to  ${}^7\text{Be}$  locus from the “correct” kinematical solution.

After another LNS test beam in September 2018, the ReD TPC has been transported back to Naples, to complete the characterization and re-commissioning in the lab there. Tests have been performed to characterize the basic TPC performance in terms of light yield, uniformity, electric field configuration and S2/S1 ratio in double phase. The system was calibrated with ordinary  $\gamma$ -sources and with an internal  ${}^{83m}\text{Kr}$  source, which generates a uniform distribution of mono-energetic events. Activities are still ongoing to characterize the extraction and multiplication fields. A campaign was also carried out at LNS to measure the neutron detection efficiency of the liquid scintillators, using a fission  ${}^{252}\text{Cf}$  source. A test beam for the characterization of the neutron beam is going to be performed at LNS in June 2019 and for this run only the Si detectors and the LSci detectors will be deployed.

The ReD project has received scientific approval by the Scientific Committee of LNS (PAC) for a five-week beam allocation that is granted for 2019. Upon completion, the ReD LAr TPC will be transported back to Catania and a new beam run with the full setup will be scheduled.

## 10. DARKSIDE-PROTO

### 10.1. Prototype Overview and Status

The objective of the DS-Proto experiment is the construction and operation of a prototype detector of intermediate size ( $\sim 1$  t), to fully validate the new DS-20k technologies for their integrity in both the mechanical and functional aspects. The prototype will be constructed using the materials planned before screening, in order to speed up the mechanical validation, and will therefore not necessarily be a physics-results oriented detector. This may evolve over time to include elements of the detectors as materials are screened and made available, and eventually all parts could be replaced with radio pure materials to form the basis of another experiment with high-sensitivity to low-mass WIMPs. Thus, DS-Proto is not intended to replace validation and tests made in laboratories, but rather complement them with the integration with the rest of the detector. The prompt execution of DS-Proto is crucial to fulfill the overall schedule of DS-20k. DS-Proto is on the critical path of the project.

The program for DS-Proto is expected to span over three different phases:

1. Design, construction and assembly at test site of the LAr TPC, with the size available for two motherboards integration;
2. Integration of 50 preproduction PDMs to the LAr TPC; assembly, commissioning, and operation of full read-out and DAQ for 50 PDMs; The  $xy$  resolution and S2 gas pocket optimization will be done during this phase.
3. Assembly and commissioning of full system, including 370 first production PDMs; full readout and DAQ operational; evolution towards final configuration.

The plan for DS-Proto was reviewed, approved, and funded by the CNS2 of INFN. Funding has already been secured from the NSF for the development and fabrication of multiple components for the TPC, the cryogenics system and resources for kick-starting the UAr extraction site preparations. Requests for funding from other participating groups are being evaluated or will be submitted in the near future.

In August 2017 the collaboration and LNGS reached and finalized an agreement [33] with the Accelerator & Technology Sector of CERN and its Technical Division to construct and commission the DS-20k cryogenics at CERN, with support from the Cryogenics Group and the Vacuum, Surfaces and Coatings Group (both groups are part of CERN’s Technical Division). The extension of this program to carry out the first surface operation of DS-Proto at CERN before moving the detector to LNGS was agreed by the CERN Accelerator & Technology Sector via an Addendum to the above agreement. The necessary space and facilities are the same as for the test on the DarkSide-20k cryogenics and are already allocated.

A cryostat for DS-Proto has been built by Tecno Alarm, s.r.l., Roma, and delivered to CERN in August 2018 (see Figure 24). The 1 mBq/kg U/Th AISI 304 L Stainless Steel was procured from NIRONIT Edelstahlhandel GmbH & Co and it is good enough to be used for a possible physics run in LNGS.

Assembly and test of the DS-20k cryogenics will take place at CERN, during the summer and last quarter of 2019. Construction of DS-Proto is expected at the end of 2019 or early 2020. The first test operation with a reduced number of photosensors is expected by summer 2019, followed by a second operation with a full complement of PDMs by early 2020. Full characterization of the prototype performance and physics runs will be performed after installation at LNGS. The detailed program of the activities to be carried out underground is under study.

We anticipate that, since the DS-Proto will be a stand alone system, sharing the DS-20k cryogenics system at LNGS will not be possible. However over the past few years of R&D for the DS-20k cryogenics, we have realized and tested several key components which will be more than capable of handling the prototype system. These parts can be used for DS-Proto with minor system integration together with most of the DS-50 and existing R&D devices.



FIG. 24. The DS-Proto cryostat and components delivered at CERN.

## 10.2. The DS-Proto TPC

The DS-Proto TPC mechanics, including the structural elements, the field cage, the reflector cage, the transparent cathode, the transparent anode (also serving as a diving bell for the containment of the gaseous phase), the SiPM PDM assemblies, the high-voltage feed through system, will all be built utilizing, on a scaled down overall dimension, the same design and construction techniques foreseen for the baseline of DS-20k (see Figure 25).

The photodetector modules will be arranged to cover the top and bottom of the TPC. Both top and bottom planes consist of 185 photodetector modules assembled into 5 SQBs and 4 TRBs. As described in section 7, the readout chain will employ commercial components used during the first phase, allowing for full digitization of the signals. The final electronics components that will be used in DS-20k will be used as they become available at each stage of the development. It is also foreseen that the optical signal transmission will be tested on a significant number of channels with this detector.

The DS-Proto photosensors are contained in 18 Motherboards made of one set of 5 (SQB) and 4 (TRB) PDMs on top, and another identical set on bottom. With both planes, the DS-Proto TPC requires 370 PDM to be fully covered. Bonding ~9000 SiPMs in a few months is one of the most critical tasks of this detector, to maintain the overall project schedule. The construction strategy relies on two bonding facilities, the first one located at Princeton University and the second one at LNGS. According to the experience gained in the past months, a bonding rate of 3 tiles /d is feasible. We therefore need 60 d to bond the 370 tiles across the two facilities.

The man power at LNGS can be provided by the NOA contracts, while finding man power at

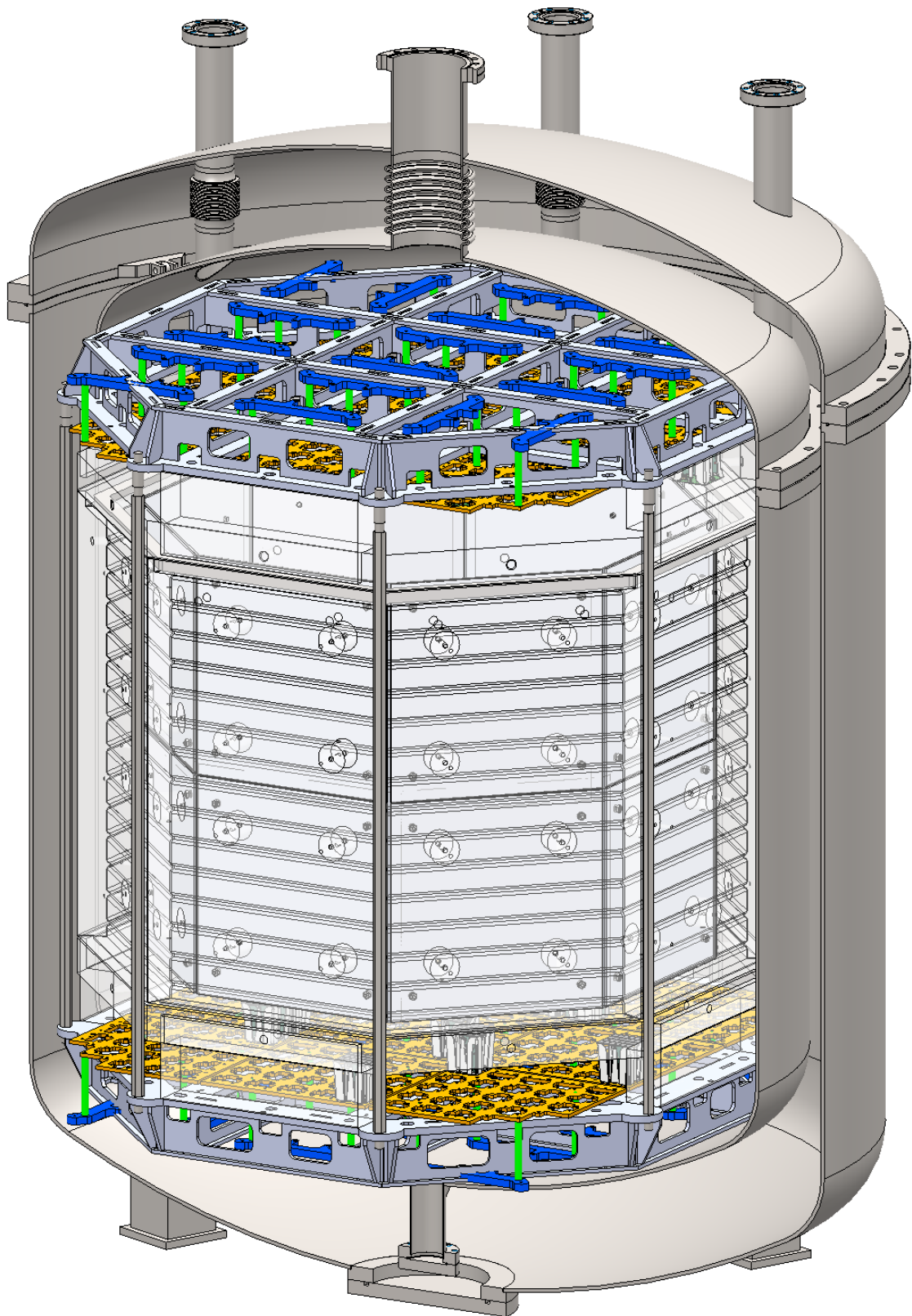


FIG. 25. Conceptual Design of the DS-Proto detector. The cryostat has already been built and delivered at CERN, see Fig. 24.

Princeton University is more challenging. Different options were evaluated, and others are under consideration. The University of Manchester (UK) has identified a candidate who will spend a significant amount of time in the course of the next year to be trained, and then do the work. A tight connection between the two production sites has to be provided, to include the harmonization of the procedures and quality assurance test. A person to provide this interface is being identified. LNGS requires a significant increase of man power since after the bonding the tiles will be equipped with a Front End Board (FEB), and then mounted and tested at LNGS. After the assembly, the tiles and the FEB will be tested in  $\text{LN}_2$ . The first Motherboard, made of 25 PDMs, was just assembled. The Motherboard will be shipped to Napoli, where a comprehensive test at cryogenic temperature is scheduled.

A powerful test facility has to be prepared at Napoli, requiring extra man power. The procedures and the tools to ship the Motherboard from Pisa to Napoli and from Napoli to CERN have to be carefully planned and made available.

### 10.3. Materials for DarkSide-Proto

Since DS-Proto is a test bench of DS-20k, it won't be used to demonstrate the material radio-purity requirements of DS-20k, however, it will be built with the goal of achieving the best radio-purity conceivable at the time of the construction, based on the current results of materials assay campaign. Additionally, DS-Proto can be used to assess the possible contamination related to the detector construction procedures (TPC and PE), evidencing material cleaning/handling issues.

The assessment of the DS-Proto radioactive budget will be obtained through the material assay campaign and the Monte Carlo simulation. The validation of the predictions concerning the neutron/gamma originated by the material contamination will be only possible through data taken underground with the DS-Proto deployed in a properly shielded environment. A physics run, focused on the low-mass WIMP search, will be eventually possible with the S2-only analysis in the keV region. In this context, the minimization of the low-energy gamma background of the prototype will be extremely important to employ as early as possible.

### 10.4. Validation tests and operation

Upon successful completion of the test phase of the different parts, we plan to measure the overall performance of the DS-Proto through some key parameters, such as the S1 light yield, the electron drift time, electro-luminescence field and gas pocket thickness uniformity for high resolution of S2 signals and the  $xy$  position reconstruction. For the purpose of optimizing the S2 signals, the first two Motherboards will be assembled into a small TPC with reduced size drift length (12 cm) to avoid pile-up (see Figure 26). Full test of the S1 response and therefore of the SiPM readout chain can be obtained at the surface by switching off the electroluminescence field. The configuration of the gas pocket (geometry and field) can be varied by changing the distance between the anode and the wire grid, the width of the gas pocket, as well as the electro-luminescence field. The S2 pulse shape can be precisely studied along with different gas pocket configurations, aiming to provide us the best solution for the future LAr TPC design. This set-up will also allow for early studies of the S2 formation and readout, to be carried out while the pre-production of the remaining Motherboards of the prototype is ongoing.

## 11. AAR CRYOSTAT

Figure 2 shows the DarkSide-20k system conceptual sketch, including the copper electromagnetic and light shield, the Veto detector and the LAr TPC, all contained within the large AAr cryostat. A ProtoDUNE-like cryostat will be employed to house the LAr bath which the TPC is immersed

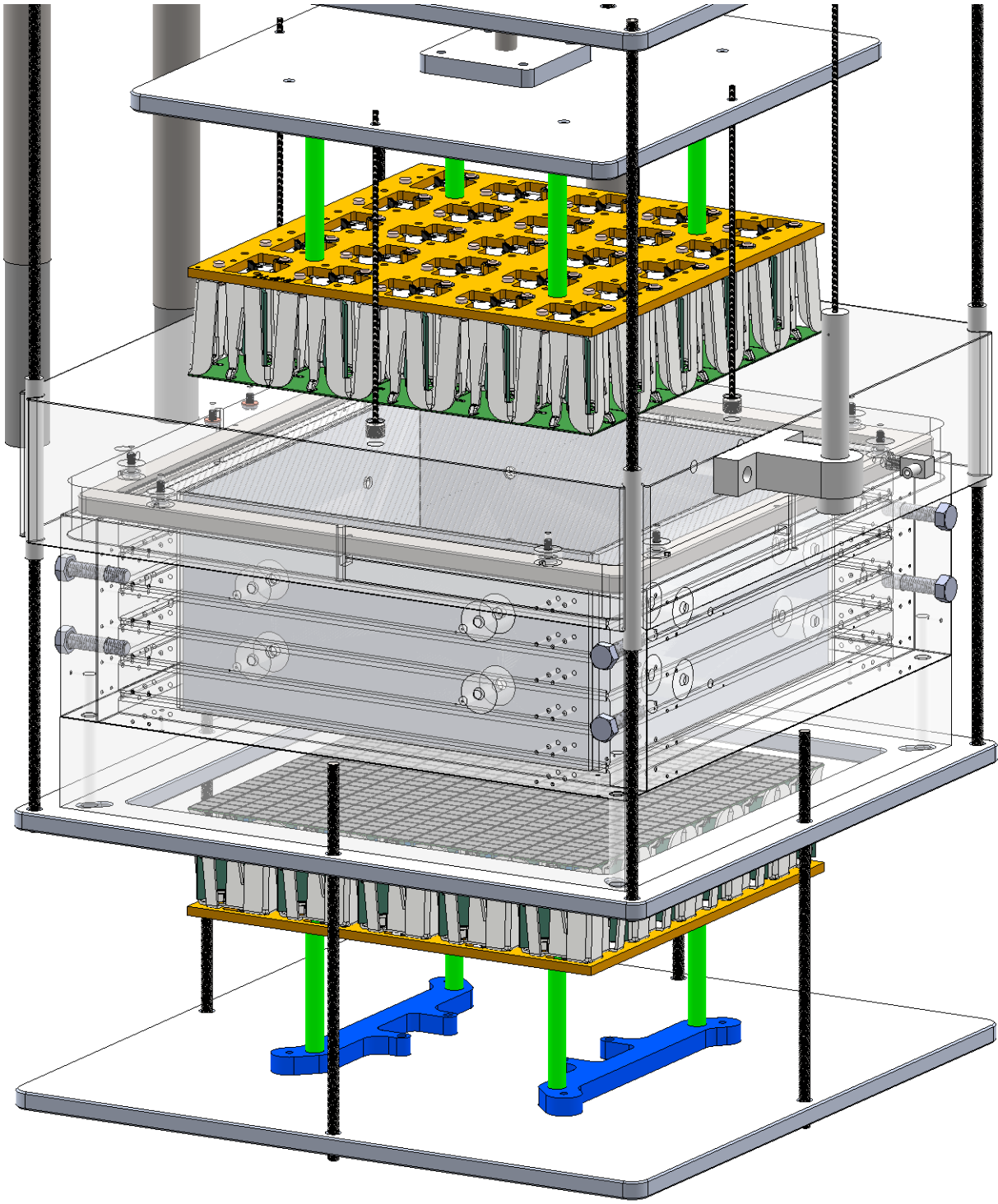


FIG. 26. Schematics of the setup for the optimization of the S2 signals.

in and also acts as the main component of the Veto detector. This allows to minimize the material of the TPC vessel and therefore to limit the possible radio-contaminations very close to the active volume.

Figure 27 shows the finished ProtoDUNE cryostat internal view while being cleaned, as well as the layout of passive thermal insulation materials that were used to construct the cryostat. The design concept for the DS-20k cryostat is based on the experience matured with the construction

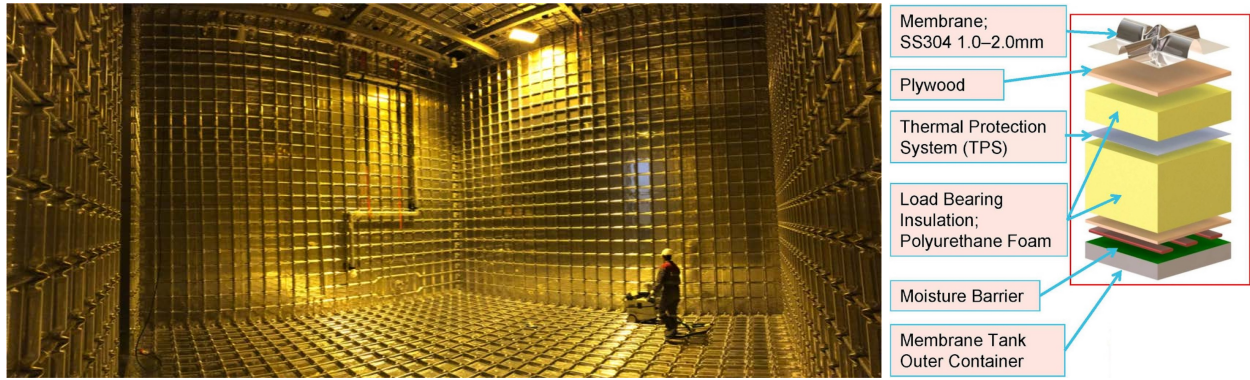


FIG. 27. **Left** Interior view of the ProtoDUNE cryostat used for the single phase LAr TPC test at CERN. **Right** Cryostat insulation construction details from GTT.

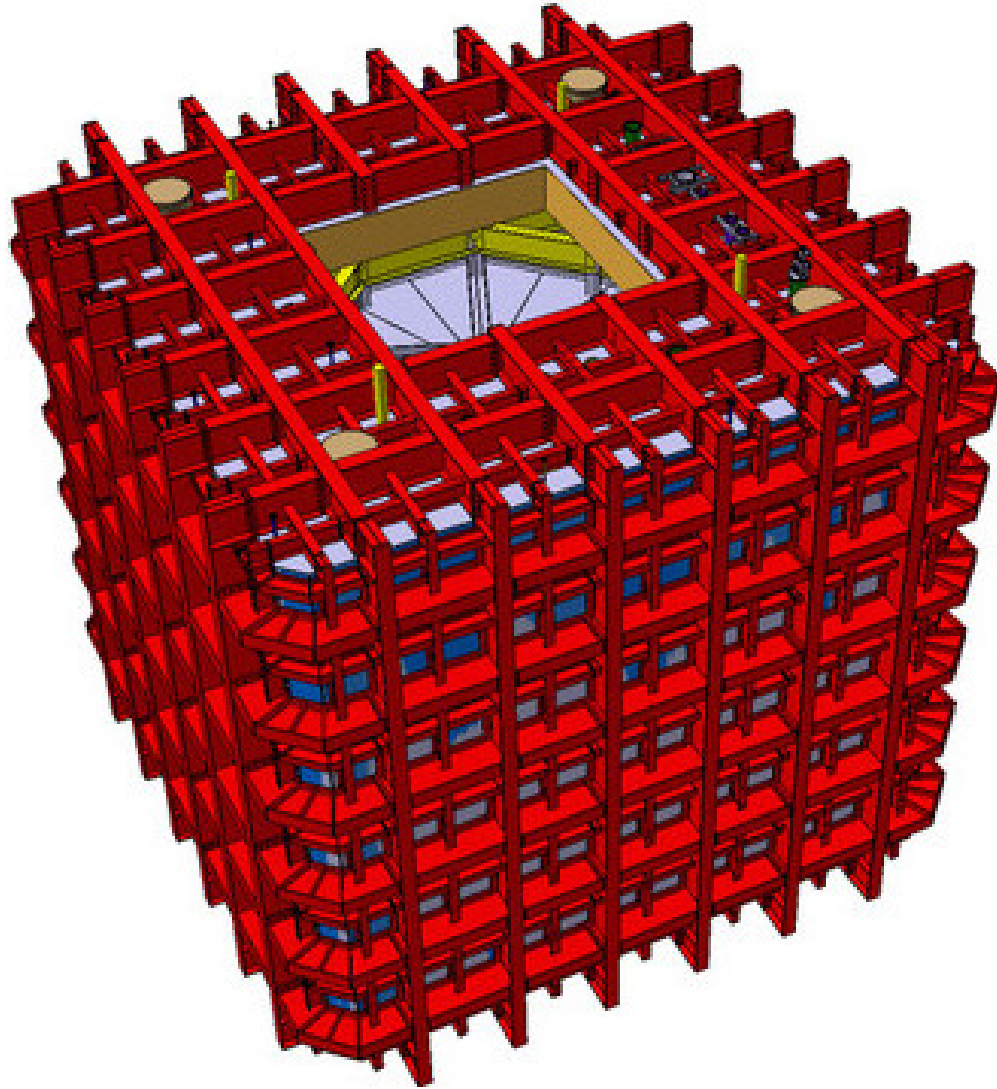


FIG. 28. 3D conceptual external view of the DS-20k AAr cryostat.

of ProtoDUNE cryostat. The technique is adopted from the LNG (Liquified Natural Gas) carriers and vessels, which has proven over many years its solidity and reliability.

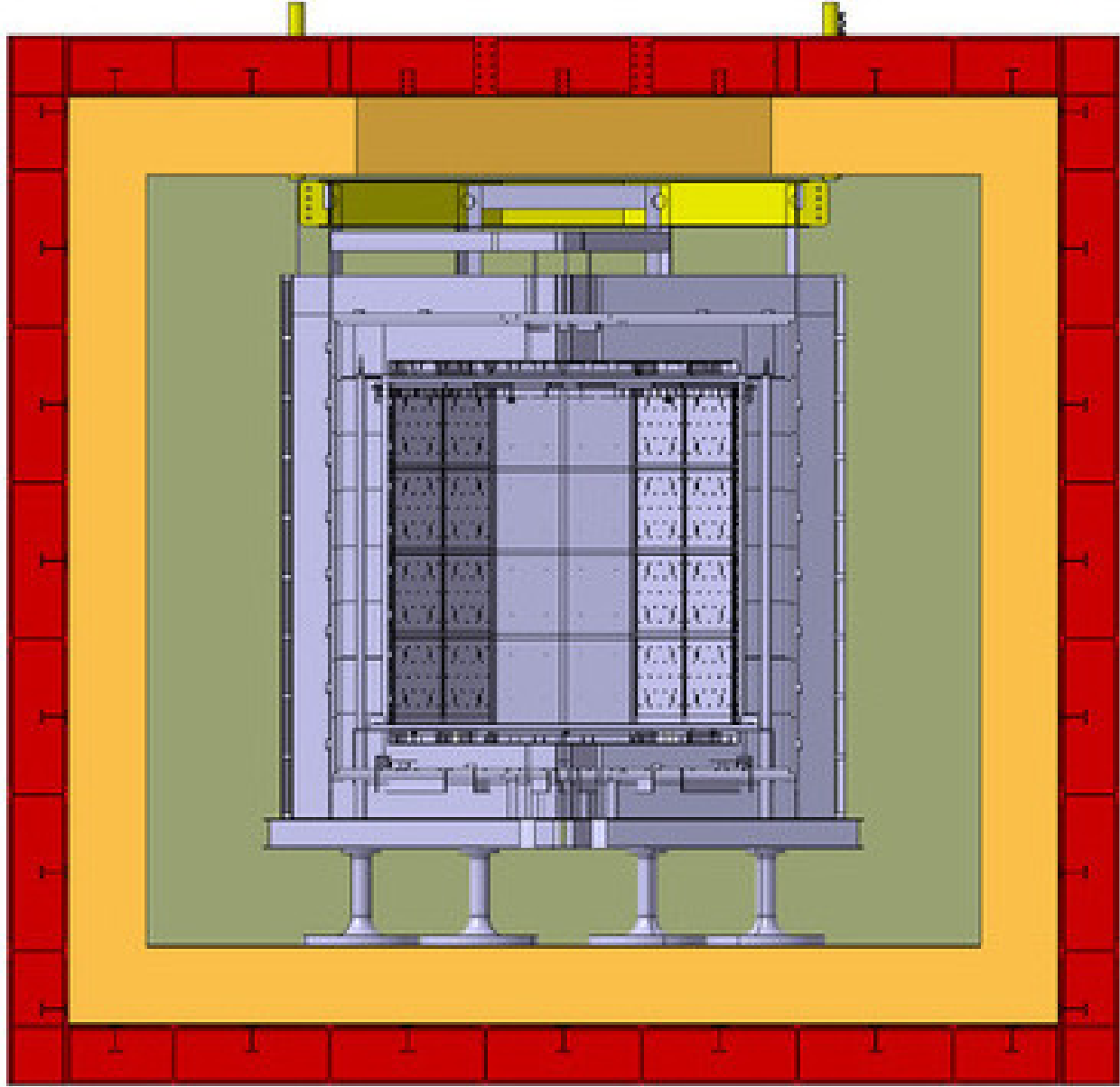


FIG. 29. Cross-sectional view of the large AAr cryostat containing the LAr TPC and Veto detectors and showing the top-cap concept.

Two cryostats of the same size as the one proposed here have been constructed at CERN and one of them has been brought into operation in the second half of 2018. The experience gained there in the design, construction and operation will be fully translated to the DS-20k project, through the involvement of the CERN group that was responsible for the construction and operations of the ProtoDUNE cryostat. For that reason, the same mechanical constraints, dimension and thermal properties have been kept. The DS-20k cryostat is an improved version based on the experiences gained during the construction of the two ProtoDUNE cryostats, namely optimized fabrication and construction and access specific for DS-20k project. A 3D conceptual view of the external part of the cryostat being planned for DS-20k is shown in Figure 28.

To make it as easy as possible for the access and support of the sub-systems of the TPC and the Veto detectors, all components will now be inserted from the roof of the cryostat, with a “closing cap” concept being implemented. This has been previously deployed by the CERN team during other large-dual phase TPC R&D experiments and tested with the construction and operation of

Element	Inlet Purity [ppm]
CH <sub>4</sub>	<0.25
CO	<0.1
CO <sub>2</sub>	<0.1
H <sub>2</sub>	<1
H <sub>2</sub> O	<1
N <sub>2</sub>	<1
O <sub>2</sub>	<1

TABLE VI. Inlet argon purity required for operation of the DarkSide-20k getter.

the first demonstrator for the ProtoDUNE project. A cross-sectional view of the concept is shown in the right side of Figure 29. The plan is to assemble the bottom and sides of the Veto detector using a temporary support frame underneath the Veto detector, and then lower the TPC down into the Veto detector while it is attached to the closing cap, see Figure 21. Once in place, the remaining parts of the Veto detector could be assembled, the entire detector system support transferred to the detector support system of the cryostat, and finally the temporary supports of the Veto detector that we required during construction removed. At this point, the two detector volumes, that of the TPC and that of the Veto, would be filled simultaneously such that the LAr height in both volumes is equal at all times in order to reduce the mechanical stress on all of the detector components.

As mentioned in Sec. 3, the AAr cryogenics system will be built based on the combined experiences of the ProtoDUNE cryogenics and the DS-50 cryogenics. The final optimization decision will be made taking into account that the different requirements of the AAr cryostat for DS-20k compared to those for ProtoDUNE, and the available space in Hall C of LNGS. Penetrations on the roof of the cryostat are being finalized such to meet the requirements of the other sub-systems, as well as to provide the mechanical stability of the cryostat ceiling. The design and development plan will follow the successful experience of ProtoDUNE, with expert engineering assistance provided by the CERN group, while already a firm baseline design is in place and schematically shown in the left side of Figure 14, along with the rest of the DS-20k cryogenics system.

## 12. ARGON PROCUREMENT AND PURIFICATION

A broad strategy has been developed to increase the production of UAr to procure the target required for DarkSide-20k. The Urania project will extract and purify the UAr from the CO<sub>2</sub> wells at the Kinder Morgan Doe Canyon Facility located in Cortez, CO, at a production rate of 250 kg/d. It will be necessary to make a final chemical purification of the UAr before deployment into the LAr TPC (driven by the filtration capacity of the getter purification unit), bringing the chemical impurity levels to those shown in Table VI. Additionally, it would be beneficial to further deplete the UAr of <sup>39</sup>Ar, giving extended sensitivity to DarkSide-20k and producing argon with a level of <sup>39</sup>Ar that is acceptable to be used in an experiment such as Argo. The Aria project will serve to chemically purify the UAr to better than the levels shown in Table VI using a cryogenic distillation column called Seruci-I. The ultimate goal of the Aria project is to process argon through Seruci-I to achieve an additional depletion factor between 10 and 100 (on top of the reduction of <sup>39</sup>Ar already seen in the UAr).

The procurement of the UAr for DarkSide-20k is broken into two main operations, extraction of the UAr by Urania and then chemical purification by Aria using Seruci-I.

### 12.1. Urania

The Urania project will extract at least 60 t of low-radioactivity UAr, providing the required 51.1 t of UAr to fill DarkSide-20k. The Urania project will also lay the groundwork for UAr procurement for future, larger argon-based detectors such as Argo. The goal of the Urania project is to build a

plant capable of extracting and purifying UAr at a rate of 250 kg/d, from the same source of UAr that was used for the DarkSide-50 detector.

The opportunity to build Urania has grown from the strong relationship between the DarkSide Collaboration and the Kinder Morgan Corporation. Based on gas analysis of the Cortez stream provided to Kinder Morgan by the DarkSide Collaboration during the extraction of the DarkSide-50 UAr target, a major industrial partnership between Kinder Morgan and Air Products was established in order to extract helium from the CO<sub>2</sub> at Kinder Morgan’s Doe Canyon facility. The Air Products helium plant began operation in July 2015 and presently supplies 15 % of the production rate to the National Helium Reserve.

The DarkSide Collaboration reached an agreement with Kinder Morgan to feed the Urania plant with a small fraction (15 %) of the gas stream returned to Kinder Morgan by Air Products after helium extraction. This gas stream holds two significant advantages over the gas stream used to extract the UAr for DarkSide-50: it is completely dehydrated, and it contains only trace amounts of helium. These features greatly simplify the process for UAr extraction by the Urania plant, while ensuring the same radioactivity levels, or better. Argon from the active CO<sub>2</sub> wells in southwestern Colorado have been found to contain very low levels of the radioactive isotope <sup>39</sup>Ar, with the concentration shown to be a factor of  $(1.4 \pm 0.2) \times 10^3$  below that of argon derived from the atmosphere [4]. In an effort lasting more than 5 years, DarkSide-50 collaborators at Princeton and Fermi National Accelerator Laboratory (Fermilab) extracted and purified  $(156 \pm 1)$  kg of UAr, slightly more than the  $(153 \pm 1)$  kg needed for the target material in the DarkSide-50 detector.

The Urania feed gas stream is  $\sim 95\%$  CO<sub>2</sub>, plus a few percent of N<sub>2</sub>, one percent CH<sub>4</sub>, 430 ppm of UAr, and traces of higher hydrocarbons. The processing scheme of the UAr extraction plant is optimized for this feed composition in order to achieve an UAr purity of better than 99.9 %. A modular plant consisting of skid-mounted units deployable on concrete platforms is being designed to carry out the processing.

The UAr extraction plant will consist of three gas-processing units, as shown in Fig. 30, followed by a cryogenic distillation unit. The gas-processing units are two CO<sub>2</sub> liquefier/strippers followed by a pressure swing adsorption unit (PSA). The first liquefier accepts gas at  $(49 \pm 1)$  bar, with a flow rate of 16 250 std m<sup>3</sup>/h and a temperature of 5 °C. At these conditions, the CO<sub>2</sub> partially condenses and the stream is separated into 2-phases (gas/liquid) as it goes to the first stripper. In the column a controlled quantity of heat is given by a hot fluid working between the chiller condenser and the column reboilers. The light products are vaporized and recovered from the top of the column in gas phase. The heavy products (mainly CO<sub>2</sub>) are collected from the bottom, compressed to 120 bar and returned to Kinder Morgan as a liquid. The light products coming from the column head are cooled down in the second step to approximately -50 °C and sent to the second stripper. The first column produces 1300 std m<sup>3</sup>/h of product flow, a factor of 5 reduction in the amount of gas to be processed by the more complex downstream units.

The second liquefaction and stripping unit further reduces the CO<sub>2</sub> content, in a similar process as the first stripping unit. The separated CO<sub>2</sub> is joined with that from the first unit and returned to Kinder Morgan. The product gas from the second stripper is re-heated in a heat exchanger and delivered to the PSA unit, which separates the light fractions, including the argon, from the remaining CO<sub>2</sub>. The PSA is composed of four adsorption beds to allow continuous operation with short time adsorption cycles. The desorption of CO<sub>2</sub> is made by decreasing the pressure on the bed. To optimize the performances, the operation of the adsorbers are combined by coupling the purge and pressure swing phases. At the outlet of the PSA adsorption tanks, one buffer tank is provided in order to dampen process fluctuations and allow for continuous operations of the final distillation process. The PSA off-gas is delivered to a recycle compressor and sent back to the second CO<sub>2</sub> stripper inlet for reprocessing.

The PSA is the most critical unit of the entire process since the dynamic adsorption conditions are the most difficult to simulate and predict. Optimization of the sorbent and other operational parameters is being done via a small scale lab setup in which breakthrough tests are being performed for a variety of gas species. A picture of the test setup being used is shown in Fig. 31. Sorbent screening relies on measurements of the breakthrough curves of the different gas species for the

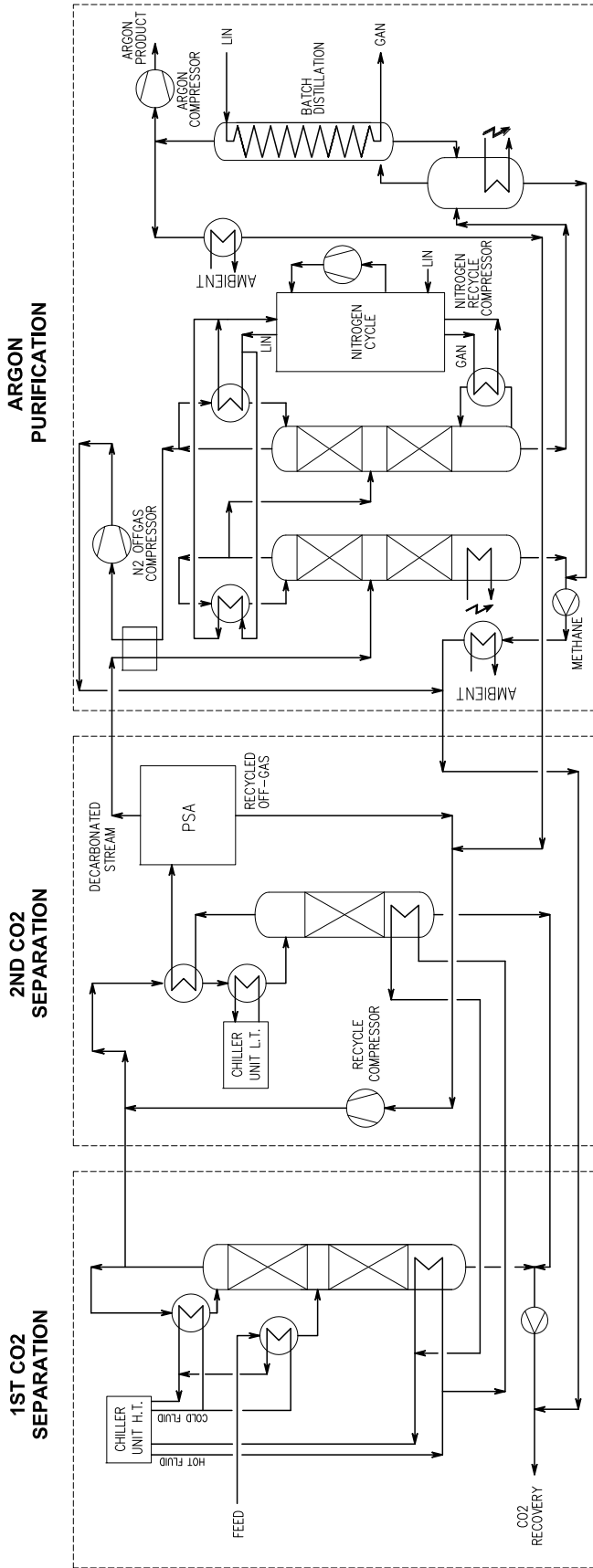


FIG. 30. Process Flow Diagram (PFD) for the Urania UAr extraction plant.



FIG. 31. Test plant in use at Università degli Studi di Napoli “Federico II” for the characterization and selection of sorbents for the PSA unit of Urania.

candidate sorbents. A selection of sorbents which could work for the PSA unit have already been identified, while the final selection of the exact sorbent to be used in the UAr extraction plant will be determined by the test results and consultation with the contracted company who will build the plant.

The final unit of the UAr extraction plant consists of three cryogenic distillation columns. The CO<sub>2</sub>-free product coming from the PSA plant is pre-cooled and sent to the first column, which works at a lower pressure (~9 barg) for the removal of CH<sub>4</sub>. The second column is used to remove the remaining light fractions from the resulting N<sub>2</sub>-rich stream, and the third to perform the final purification of the UAr using a batch distillation process. In addition to removing the CH<sub>4</sub> and N<sub>2</sub> at this point, any <sup>85</sup>Kr present in the stream will also be removed by the series of three cryogenic distillation columns. The CH<sub>4</sub>-rich and N<sub>2</sub>-rich distillation wastes are returned to Kinder Morgan along with the CO<sub>2</sub>. The final product, 99.9 % pure UAr, will be taken in liquid form from the top of the last column and a small portion collected into a tank to check the quality of the argon. The majority of the liquid UAr will be sent to the appropriate cryogenic vessels for shipment to Sardinia, where it will undergo final chemical purification by the Seruci-I column.

The Urania project has recently made significant strides, most importantly with the opening of the tender for the construction and shipment of the argon extraction plant by the INFN. The opening of the tender has officially marked the start date for the progression of the sub-project schedule, and the timeline for the extraction of the 60 t of UAr required for the DS-20k experiment has now been set and has been integrated with the overall project schedule. It is now expected that the tender process will close at the beginning of the fourth quarter in the 2019 calendar year, and at that point a contract will be executed for the construction and delivery of the plant to the extraction site in Colorado, USA.

The tender for the construction of the argon extraction plant has been opened and the winner will be selected and contract signed by the end of October, 2019. The plant will be delivered to the Kinder Morgan Doe Canyon Facility by the end of 2020 calendar year. The current plan is to install and commission the plant in the first three quarters of 2021 calendar year, allowing for extraction

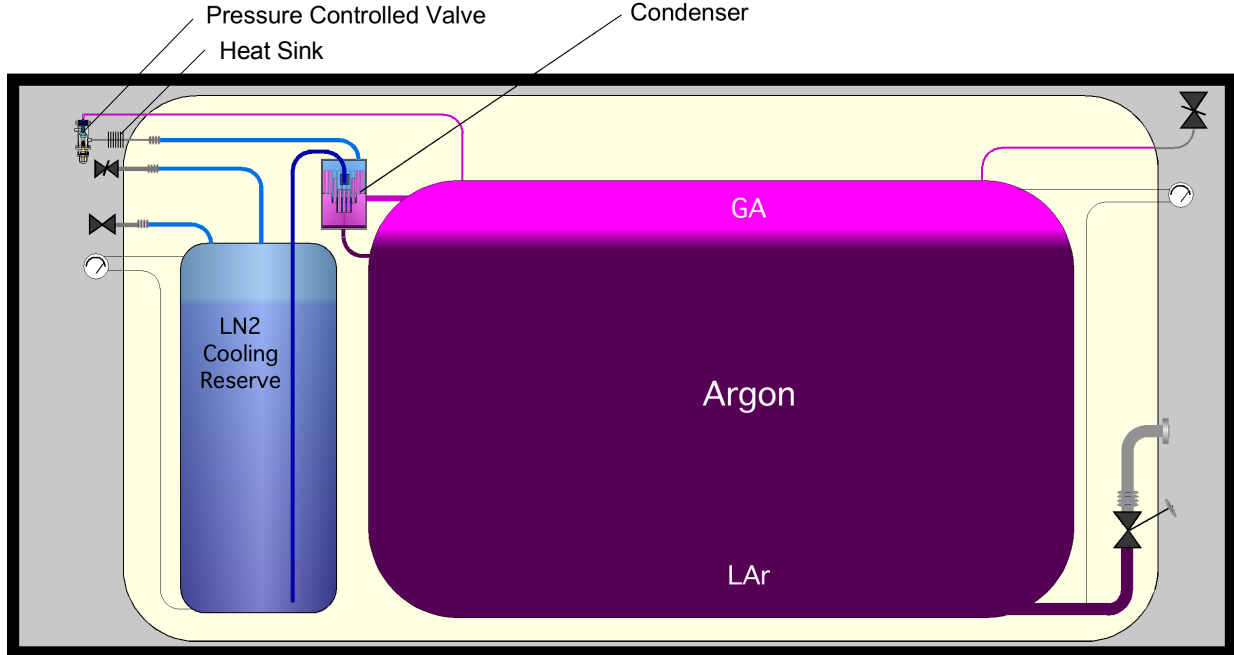


FIG. 32. Schematic view of the cryogenic shipping vessel design, one of the two options for argon shipment from Colorado to Sardinia.

of the 60 t of UAr by the middle of the 2022 calendar year, in order to meet the DarkSide-20k schedule. The preparation of the extraction site is being planned now and will be managed by the collaboration with help from the Kinder Morgan CO2 Company and the contractors hired to carry out the work. Site preparations for developing the facility before the arrival and installation of the plant will begin as soon as the necessary land development permits have been secured and the RFQ process has been completed.

The shipment from Colorado to Sardinia will be done by boat in order to minimize the cosmic activation of the argon. For the shipment of the UAr from Colorado, two options are under investigation. The first option, which was determined to be the baseline method, is to ship the UAr in liquid phase using custom built cryogenic vessels. This is a more efficient and cost effective method, compared to shipping the UAr in gas phase. The custom built cryogenic vessels will have a double wall structure, there will be two inner volumes with the larger one containing the UAr and the smaller containing LN<sub>2</sub>. The outer volume would be at ultra-high vacuum to thermally insulate the two inner volumes from the atmosphere at ambient temperature. During the transport, a LN<sub>2</sub> fed condenser would slowly re-liquify the UAr as it evaporated away, ensuring that none of the UAr would be lost during the trip. A schematic view of the cryogenic vessel design is shown in Fig. 32. A minimum of five cryogenic vessels is foreseen enabling one for Urania production, one for Aria feed, one for Aria production, and two traveling between Sardinia and LNGS for delivery and then LNGS and Sardinia for further production of UAr, at all times.

In the case of cryogenic shipping, the extracted UAr will be shipped to Sardinia in batches of 11 t (roughly every 100 days) in liquid phase, also eliminating the need to liquify the UAr to be reprocessed by the Aria column. After chemical purification in Aria, the UAr will then be shipped to LNGS, also in batches of 11 t, and stored in the argon recovery system. In order to minimize the exposure to cosmic rays, the argon will be stored underground at Seruci and/or LNGS for any necessary long durations.

The second option that is now being investigate as an alternative, is to ship the UAr in high-pressure gas cylinder placed in trailers which can be hauled by trucks. This option is made possible by special cylinders which allow for the storage of argon at pressures up to 400 bar. With pressures of this magnitude, and cylinders that are able to be the size of large trailers, the number of trailers

that would be required for the total DS-20k detector target is something that is manageable, on the order of 10 to 20 depending on the storage pressure. The overall benefit of moving to this option, instead of going with the cryogenic vessel option, is that the gas can be maintained in the cylinders for years without the need of any type of consumable to prevent the loss of the argon. This would basically eliminate the risk of losing any of the UAr during the transport and storage, other than potential loss of the shipment.

The Urania project team is now collecting all of the information that is required to make the technical and economic assessment of the two options. Based on the technical risks and the economic impact on the project, the option that is best for the overall project will be chosen.

## 12.2. Aria

The aim of Aria is to perform chemical purification of the UAr extracted by Urania. Aria will also be the test bench to develop active depletion of  $^{39}\text{Ar}$  from the UAr to possibly provide DAr targets for future larger-scale LAr detectors. Aria consists of a 350 m tall distillation column, Seruci-I, capable of separating isotopes with cryogenic distillation, a process that exploits the tiny difference in volatility due to the difference in isotopic mass [34–39].

The design of the plant started in April 2015 with seed funding from the US NSF through PHY-1314507. Aria is to be installed in a underground vertical shaft of 5 m diameter and 350 m depth, located at the Seruci mine campus of CarboSulcis, a mining company owned by the Regione Autonoma della Sardegna (RAS). In February 2015 a proposal was submitted to the Italian INFN and RAS, and the funding for the Seruci-I column was approved on July 24, 2015. Construction of Seruci-I modules started in September 2015 in a Italian company.

The measurements of the relative volatility of argon isotopes [40–42] and their theoretical interpretation [43–45] marked the birth of the Italian school of condensed matter in Genoa and Milan. The study of the relative volatility of argon isotopes was recently revisited [46, 47] and shows a promising path for the separation of  $^{39}\text{Ar}$  from  $^{40}\text{Ar}$ . Following these studies, DarkSide collaborators developed the framework for comparing  $^{39}\text{Ar}$  to  $^{40}\text{Ar}$ . Algorithms developed to calculate the relative volatility of argon isotopes, based on the extensive and detailed models available in the literature, predict that the volatility of  $^{39}\text{Ar}$  relative to  $^{40}\text{Ar}$  is  $1.0015 \pm 0.0001$ , and that it stays constant within theoretical uncertainties in the range of temperatures practical for the distillation of argon (84 K to 100 K). The small volatility difference can be used to achieve active isotopic separation by using a cryogenic distillation system with thousands of equilibrium stages.

Design of the Aria plant was optimized on the basis of high-precision numerical methods for estimating the isotopic separation of  $^{39}\text{Ar}$  from  $^{40}\text{Ar}$ . DarkSide Collaborators developed two independent numerical codes, one based on the McCabe-Thiele method [48], and a second based on the Fenske-Underwood-Gilliland (FUG) method and its derivative, the Wynn-Underwood-Gilliland (WUG) method [49–51]. Calculations for the isotopic separation power of  $^{39}\text{Ar}$  from  $^{40}\text{Ar}$  and of the processing rate were performed with the custom codes, as well as with software routines supported by commercial chemical engineering CAD programs, such as Aspen [52].

Fig. 33 illustrates the core of the process for isotopically separating  $^{39}\text{Ar}$  from  $^{40}\text{Ar}$ . The process consists mainly of two loops: the process loop where the argon is distilled and the  $^{39}\text{Ar}$  is separated from the  $^{40}\text{Ar}$ , and the refrigeration loop where nitrogen gas and liquid is used to evaporate and to condense the argon. Most of the heat is recovered, thanks to the compressor that pumps the nitrogen gas evaporated in the condenser to the reboiler and to the pumps that move the liquid nitrogen produced in the reboiler to the condenser, making the system as efficient as possible. In Fig. 33 all the sub-parts of the plant are represented:

- Feed station, to filter and regulate the feed to the column;
- Compressor station, to bottle the distillate at the bottom;
- Vacuum system, to keep a good vacuum in the cold-box, in order to minimize the heat losses;
- $\text{LN}_2$  storage;

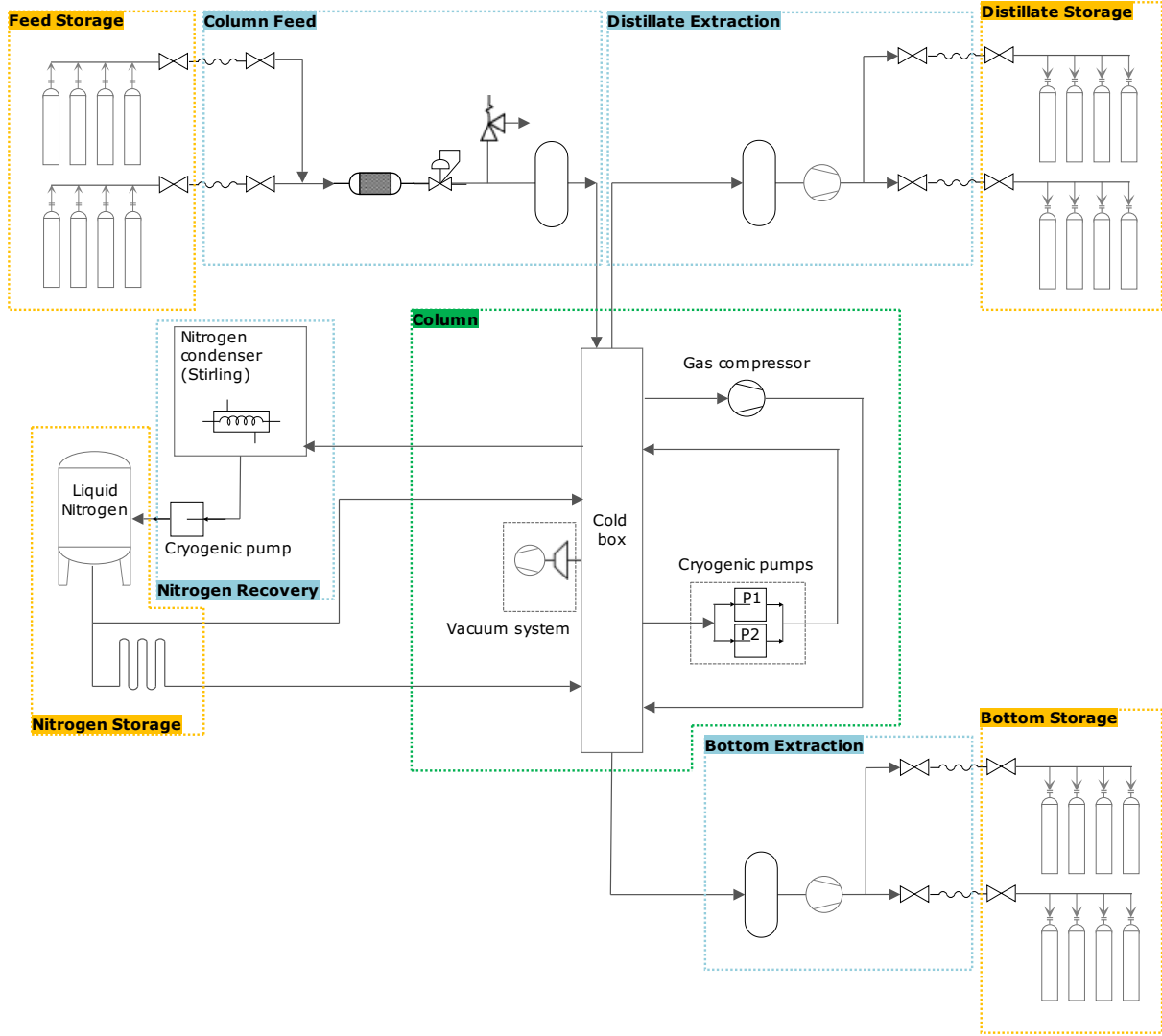


FIG. 33. Block diagram of the cryogenic system of the Aria plant.

- Nitrogen condenser system, consisting of 4 Stirling cryo-refrigerators needed to re-condense the nitrogen, used in a closed loop.

Seruci-I will consist of 28 modules of 12 m height, plus a top module (condenser) and a bottom module (reboiler).

Calculations indicate that Seruci-I will be able to process UAr at a rate of  $O(1 \text{ t/d})$  removing all chemical impurities (including traces of  $\text{N}_2$ ,  $\text{O}_2$ , and  $\text{Kr}$ ) with a separation power better than  $10^3$  per pass. Additionally, Seruci-I can be used in a different mode of operations to test the isotopic separation of the argon, in order to further reduce the  $^{39}\text{Ar}$  content in the UAr. The same models which have been used to calculate the chemical purification rate, have also been used to show that Seruci-I would be able to isotopically separate the UAr at a rate of  $10 \text{ kg/d}$ , while obtaining an  $^{39}\text{Ar}$  depletion factor of 10 per pass.

All modules for Seruci-I have already been built and passed a series of quality assurance checks. During the first check, the process column and all the service pipes were individually checked for leaks at room temperature. Then, the pipes were wrapped with super-insulation and everything was assembled into the cold box. The second check was a full module check, with an additional check done on the bottom reboiler module at  $77\text{K}$ . To date, all modules have passed both checks

at room temperature and the bottom module has passed the final cold temperature check.

Seruci-0 is a test column that is made with the Seruci-I top and bottom modules and a single central module. The goal of Seruci-0 is to confirm the proper operation of the three main components of the Seruci-I column, as well as to gain experience in operating the column on a smaller scale and to put in place the standard operating procedures. The three modules have been completely installed in a outdoor assembly hall at Nuraxi Figus, Italy, seen in Figure 34. During the last months, all the leak-check tests have been performed in order to guarantee the design tightness. Moreover, most of the plants have been installed and assembled in the area surrounding the column itself. Moreover, two concrete platforms were built: they currently host the liquid nitrogen dewar and the accessory plants, the cooling machine (chiller) and a control room to host people on shift and to organize the slow control. Test operations of Seruci-0 will start in summer of 2019.

Concerning the installation of Seruci-I, all the documents needed for the authorization request for installation were submitted in May 2018 to the competent authorities. During the first half of 2019, several meetings have been held, both with the fire brigade and with other local and county offices, entities and authorities. The authorization were eventually obtained. During 2018 a complete cleaning and preparation of the well at the Seruci site has been performed. A well-defined coring procedure was concluded in 2018. After the examination of the rocks samples, the design for the Seruci-I supporting structure was detailed. The tender was completed in Autumn 2018, and at the beginning of 2019 a carbon steel sample platform was delivered to the mine and installed in the Seruci well. The test was successful and was very useful in order to define all installation steps. The goal is to receive all of the platforms by the end of May 2019 and to install them inside the well by the end of 2019.

### 12.3. DArT

The DArT experiment will re-use the ArDM infrastructure with minimal modifications made and will consists of a radio-pure single-phase LAr detector with about one liter contained inside of its active volume. The DArT detector itself will be placed inside the middle of the ArDM vessel. DArT will be filled with argon to be tested in order to measure the content of  $^{39}\text{Ar}$ . The detector will be readout by two cryogenic SiPMs each with a surface area of  $1\text{ cm}^2$ . The SiPMs and the readout electronics will come from the DS-20k production chain.

The ArDM detector will act as an active veto against internal and external radiation. For this purpose, we are building a dedicated single phase setup with a new set of low-radioactive photo-multipliers (PMT). However, we will also retain the entire present double phase setup for later use, e.g. for measurements of large quantities of depleted argon.

Extensive GEANT4-based simulations were performed using the Monte Carlo simulation package inherited from the DarkSide-50. These simulations show that DArT will achieve a sub-% measurement when operated inside the ArDM detector, for  $^{39}\text{Ar}$  concentrations a factor of ten smaller than those of AAr, and in about a week of running. A 2% measurement could be made for  $^{39}\text{Ar}$  concentrations as low as two orders of magnitude (statistical uncertainty only) smaller than those in AAr. This setup will also be useful to characterize the performance of Aria, which is expected to suppress the  $^{39}\text{Ar}$  content by a factor of 10 per pass.

A very important addition to the setup described above will consist of adding a 6 t lead belt about 140 cm tall around the ArDM vessel, at the mid-height position. This will suppress the impact of external photons that dominate the background budget and allow for the measurement of even larger  $^{39}\text{Ar}$  depletion factors, corresponding to that of the UAr. If the depletion levels are those already measured in the past (i.e. of 1400), it will be possible, according to our simulations, to measure them with a 7% uncertainty in about a week of running. Upper limits can be set on depletion factors of order 25 200 (statistical uncertainty only), i.e. UAr with one distillation pass in Aria.

The argon from Urania is expected to be available only after mid-2021. However, it is planned that after the run of DS-50 at LNGS, presumably at the end of 2019, its argon will be measured with

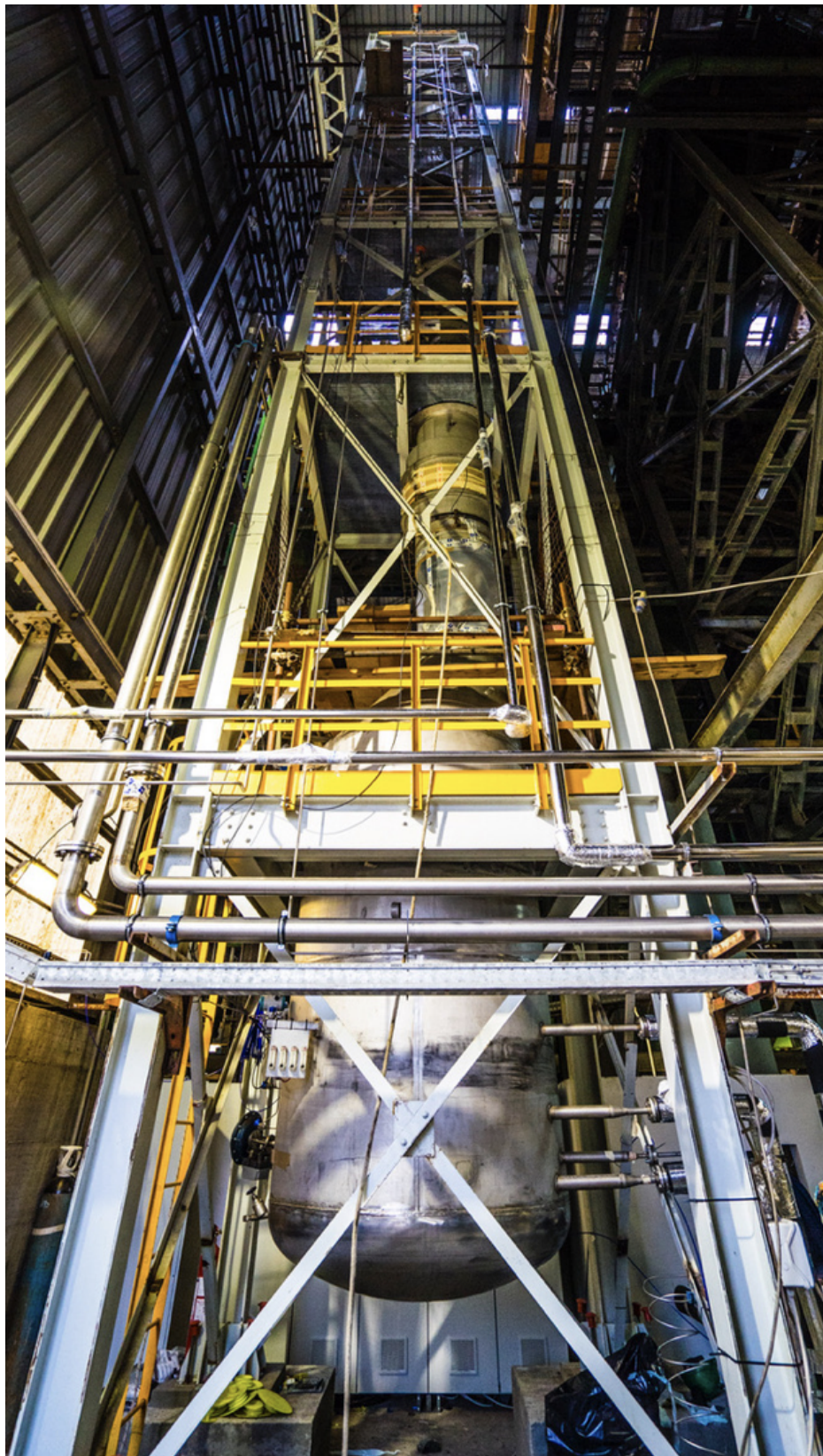


FIG. 34. The Seruci-0 cryogenic distillation column, installed in the *Laveria* building of Carbosulcis in Nuraxi Figus, Sardinia, Italy.

DArT to cross-check the original measurement taken with DS-50 and to test the new setup. This DArT experiment is expected to become a useful facility within LSC for the years to come, since it will be needed to measure samples of the extracted argon from Urania over time. An Expression of Interest and a TDR were recently submitted to the LSC Directorate. Detector construction in all collaborating institutions has already started.

---

- [1] P. Agnes et al. (The DarkSide Collaboration), *Phys. Lett. B* **743**, 456 (2015).
- [2] P. Agnes et al. (The DarkSide Collaboration), *JINST* **11**, P12007 (2016).
- [3] P. Agnes et al. (The DarkSide collaboration), *JINST* **11**, P03016 (2016).
- [4] P. Agnes et al. (The DarkSide Collaboration), *Phys. Rev. D* **93**, 081101 (2016).
- [5] P. Agnes (Université Paris Diderot), Ph.D. thesis, Université Paris Diderot (2016), URL <https://tel.archives-ouvertes.fr/tel-01497505v1>.
- [6] P. Agnes et al. (The DarkSide Collaboration), *JINST* **12**, P12011 (2017).
- [7] P. Agnes et al. (The DarkSide Collaboration), *JINST* **12**, P01021 (2017).
- [8] P. Agnes et al. (The DarkSide Collaboration), *JINST* **12**, P10015 (2017).
- [9] P. Agnes et al. (The DarkSide Collaboration), *JINST* **12**, T12004 (2017).
- [10] P. Agnes et al. (The ARIS Collaboration), *Phys. Rev. D* **97**, 10 (2018).
- [11] P. Agnes et al. (The DarkSide Collaboration), *Nucl. Inst. Meth. A* **904**, 23 (2018).
- [12] P. Agnes et al. (The DarkSide Collaboration), *Phys. Rev. D* **98**, 102006 (2018).
- [13] P. Agnes et al. (The DarkSide Collaboration), *Phys. Rev. Lett.* **121**, 081307 (2018).
- [14] P. Agnes et al. (The DarkSide Collaboration), *Phys. Rev. Lett.* **121**, 111303 (2018).
- [15] B. Abi et al. (The DUNE Collaboration), arXiv:1706.07081v2 (2017).
- [16] R. Acciarri et al. (The DUNE Collaboration), arXiv:1601.05471v1 (2016).
- [17] H. Cao et al. (The SCENE Collaboration), *Phys. Rev. D* **91**, 092007 (2015).
- [18] T. Alexander et al. (The SCENE Collaboration), *Phys. Rev. D* **88**, 092006 (2013).
- [19] I. Ostrovskiy et al., *IEEE Trans. Nucl. Sci.* **62**, 1825 (2015).
- [20] W. J. Willis and V. Radeka, *Nucl. Inst. Meth.* **120**, 221 (1974).
- [21] V. Radeka, *IEEE Trans. Nucl. Sci.* **21**, 51 (1974).
- [22] V. Radeka and S. Rescia, *Nucl. Inst. Meth. A* **265**, 228 (1988).
- [23] R. L. Chase, C. de La Taille, S. Rescia, and N. Seguin, *Nucl. Inst. Meth. A* **330**, 228 (1993).
- [24] R. L. Chase and S. Rescia, *IEEE Trans. Nucl. Sci.* **44**, 1028 (1997).
- [25] M. D'Incecco et al., *IEEE Trans. Nucl. Sci.* **65**, 1005 (2018).
- [26] W. Ootani, *Nucl. Inst. Meth. A* **732**, 146 (2013).
- [27] P. W. Cattaneo et al., *Nucl. Inst. Meth. A* **828**, 191 (2016).
- [28] M. D'Incecco et al., *IEEE Trans. Nucl. Sci.* **65**, 591 (2018).
- [29] I. Ostrovskiy (The University of Alabama), (2012).
- [30] C. E. Aalseth et al. (The DarkSide Collaboration), *Eur. Phys. J. Plus* **133**, 131 (2018).
- [31] C. M. Nantais, B. T. Cleveland, and M. G. Boulay, *AIP Conf. Proc.* pp. 185–188 (2013).
- [32] A. S. Barabash et al., *Nucl. Inst. Meth. A* **868**, 98 (2017).
- [33] L. Mapelli et al., *CERN EDMS* **1837551** (2017).
- [34] F. A. Lindemann, *Phil. Mag.* **38**, 173 (1919).
- [35] H. C. Urey, F. G. Brickwedde, and G. M. Murphy, *Phys. Rev.* **40**, 1 (1932).
- [36] J. de Boer and R. J. Lunbeck, *Physica* **14**, 520 (1948).
- [37] J. de Boer, *Physica* **14**, 139 (1948).
- [38] J. de Boer and A. Michels, *Physica* **6**, 97 (1939).
- [39] J. Bigeleisen, *J. Chem. Phys.* **34**, 1485 (1961).
- [40] G. Boato, G. Scoles, and M. E. Vallauri, *Nuovo Cim.* **23**, 1041 (1962).
- [41] G. Boato, G. Casanova, G. Scoles, and M. E. Vallauri, *Nuovo Cim.* **20**, 87 (1961).
- [42] G. Boato, G. Scoles, and M. E. Vallauri, *Nuovo Cim.* **14**, 735 (1959).
- [43] G. Casanova, A. Levi, and N. Terzi, *Physica* **30**, 937 (1964).
- [44] C. Casanova, R. Fieschi, and N. Terzi, *Nuovo Cim.* **18**, 837 (1960).
- [45] R. Fieschi and N. Terzi, *Physica* **27**, 453 (1961).
- [46] J. N. Canongia Lopes, A. A. H. Pádua, L. P. N. Rebelo, and J. Bigeleisen, *J. Chem. Phys.* **118**, 5028 (2003).
- [47] J. C. G. Calado, F. A. Dias, J. N. C. Lopes, and L. P. N. Rebelo, *J. Phys. Chem. B* **104**, 8735 (2000).
- [48] W. L. McCabe and E. W. Thiele, *Ind. Eng. Chem.* **17**, 605 (1925).

- [49] A. J. V. Underwood, *Ind. Eng. Chem.* **41**, 2844 (1949).
- [50] E. R. Gilliland, *Ind. Eng. Chem.* **32**, 1220 (1940).
- [51] M. R. Fenske, *Ind. Eng. Chem.* **24**, 482 (1932).
- [52] Aspen Technology, Inc., *Aspen Plus®* (2015).